Synthesis and characterisation of sputtered thin films for renewable energy purposes

Phuong Dan Nguyen

Thesis submitted in partial fulfilment of the requirements for the degree of Philosophiae Doctor

Department of Physics

Faculty of Mathematics and Natural Sciences

University of Oslo

November 2012

Series of dissertations submitted to the
Faculty of Mathematics and Natural Sciences, University of Oslo
No. 1292

ISSN 1501-7710

Cover: Inger Sandved Anfinsen.
Printed in Norway: AIT Oslo AS.

Produced in co-operation with Akademika publishing.
The thesis is produced by Akademika publishing merely in connection with the thesis defence. Kindly direct all inquiries regarding the thesis to the copyright holder or the unit which grants the doctorate.

Abstract

In the past years, a large body of work has been dedicated to semiconductor quantum dots embedded in thin films of oxide and nitride, as the tailorable electronic and optical properties of these nanostructures make them desirable for various optoelectronic applications. The properties of these low-dimensional semiconductor systems are directly related to the atomic arrangement, distribution and size of the quantum dots, the structure of the surrounding matrices and the distance between the quantum dots. The quantum confinement of carriers in the quantum dots, their interaction, and local states in the matrices are the dominating factors determining the material properties.

The present work focuses on studying the atomic structures of these materials, and how their optical and electronic properties vary as a function of size and structure. Two material systems were especially synthesized as part of this work; Si and Ge quantum dots embedded in Si_3N_4 and SiO_2 matrices, respectively. Direct evidence of quantum confinement effects on plasmon energies, interband and conduction band structures as a function of the size and morphologies of the aforementioned Si and Ge quantum dots are provided by exploiting the high spatial and energy resolution of state of the art Scanning Transmission Electron Microscopy (STEM). The discrepancies between earlier theoretical and experimental works on the behavior of confined plasmons and interband transitions are discussed in terms of crystal imperfections, interface states and the chemistry of the surrounding matrix of each system. A comparison between the confinement strength in the system of Si and Ge quantum dots was also brought into discussion. To date, the existing experimental works found in literatures cannot unambiguously identify the correlation between chemical bonding and optical properties of the embedded quantum dots, due to the complexity of these systems. Moreover, the theoretical approaches to this matter are more than often contradictory. The combination of complementary techniques in the present work has drawn a consistent picture of bonding structures and resulting optical properties of Si quantum dots embedded in silicon nitride, and simultaneously highlighted the important impact of oxygen incorporated into the films. A model of gap states and electronic transitions for the silicon nitride films is proposed, which explains adequately the role of QC excitons vs defects in the visible luminescence of silicon nitride films with and without Si quantum dots. These results provide important information for understanding the quantum dots' physical properties and the possibility for improvements of optoelectronic applications, like solar cells.

Acknowledgments

I would like to extend my sincere thanks and gratitude to my supervisors, Prof. Arne Olsen, Prof. Terje Finstad and Ass. Prof. Anette Eleonora Gunnæs for their academic guidance, support and for being a very patient and understanding committee.

I have to mention a very special “thank you” to Dr. Demie Kepaptsoglou for her invaluable contribution in all of my works, for daily scientific discussions, for her personal support, great patience and sympathy at all times. I would also like to thank Dr. Quentin Ramasse for his generous scientific guidance and input, for sharing his expertise and knowledge, and for his precious feedback and intensive review in the writing process.

I would like to express my gratitude to Ole Bjørn Karlsen for his irreplaceable role in my experimental works and for enjoyable discussions in science and life. I would like to thank my fellow lab members, Kjetil Valset, Fredrik Sydow Hage, Øystein Prytz, Espen Flage-Larsen, Annett Thøgersen, Martin F. Sunding and Lars Olav Vestland for their assistance, for the stimulating discussions, and for all the fun we have had in the last four years.

My acknowledge also goes to the financial, academic and technical support of the University of Oslo and the SuperSTEM Laboratory that provided the necessary means for this research.

Last but not the least, I am deeply grateful to my dearest parents for making me believe in myself and encourage me to pursue my PhD degree.

Preface

The project “Synthesis and characterisation of thin films for renewable energy purposes” funded by the University of Oslo was started in December 2008. The main part of the project was carried out in the Structure Physics group, in collaboration with the SuperSTEM Laboratory funded by the U. K. Engineering and Physical Sciences Research Council and the Physical Electronic group at the Department of Physics, University of Oslo. My supervisors at the University of Oslo were Professors Arne Olsen, Terje Finstad and Anette Eleonora Gunnæs. Experimental work at the SuperSTEM Laboratory was carried out in collaboration with Dr. Despoina Maria Kepaptsoglou and Dr. Quentin Ramasse.

This PhD project was motivated by the potential of the third generation solar cells, which seek to increase the device efficiency above the Shockley-Queisser limit, and the recent advances in aberration-corrected scanning transmission electron microscopy and electron energy loss spectroscopy that allow the investigation of the electronic structure and chemistry of materials with sub-angstrom spatial resolution. The work focused on studies of the structure and electronic properties of semiconductor quantum dots using mainly transmission electron microscopy and electron energy-loss spectroscopy. The synthesis and structural characterization of the semiconductor quantum dots were carried out at the Structure Physics group, University of Oslo. Due to the extremely small dimensions of the quantum dots and the need of high spatial and energy resolution instrument for very detail experiments, the investigation of the quantum dots’ chemical bonding and electronic properties was carried out by advanced analytical scanning transmission electron microscopy at the SuperSTEM Laboratory. There is a direct continuation of, and an improvement on, the important and novel results reported in the first to the third paper, which provided one of the first direct experimental evidence for the presence of quantum confinement effects in individual Si and Ge quantum dots in a dielectric matrix. The contribution from this work very much provides an improved understanding of the condensed matter physics responsible for the quantum behaviors of the quantum dots, while from a practical point of view it would also arguably provides important result for the photovoltaic community concerned with device/materials performance.

List of abbreviations

CMOS	Complementary Metal Oxide Semiconductor
ED	Electron Diffraction
EELS	Electron Energy-Loss Spectroscopy
EFTEM	Energy-Filtered Transmission Electron Microscope
ELNES	Electron Energy-Loss Near Edge Structure
EMA	Effective Mass Approximation
EPIA	The European Photovoltaic Industry Association
FWHM	Full-width at half-maximum
HAADF	High-Angle Annular Dark-Field
HRTEM	High-resolution Transmission Electron Microscope
MEG	Multiple Exciton Generation
NCs	Nanocrystals
PECVD	Plasma-enhanced Chemical Vapour Deposition
PL	Photoluminescence
PV	Photovoltaic
QC	Quantum confinement
QDs	Quantum dots
RCA	Radio Corporation of America
RF	Radio frequency
SRN	Si-rich silicon nitride
STEM	Scanning Transmission Electron Microscope
TEM	Transmission Electron Microscope
XPS	X-ray Photo Electron Spectroscopy

Contents

Chapter 1

Introduction

While the world's current electricity supply is mainly generated from fossil fuels, these traditional energy sources face a number of problems including rising prices, dependence on imports from a limited number of countries which have significant fossil fuel supplies, and environmental concerns over the climate change associated with power generation using fossil fuels. As a result of these, there is increasing support to the development of alternative energy sources and new technologies for electricity generation. Renewable energy sources, which are generally unlimited in availability, such as solar, biomass, hydroelectric and wind-power generation, have emerged as potential alternatives which address some of these concerns. Solar power generation has arisen as one of the most rapidly growing renewable sources of electricity. In this chapter, a brief introduction about the trend of solar power development, third generation photovoltaic solar cells and the use of semiconductor nanostructures in this field will be presented. Furthermore, and to the theme of this dissertation, the properties of Si and Ge nanostructure and theoretical models applied for these systems will be addressed, with respect to their application in photovoltaic cells.

1.1. The boom of photovoltaics

Through the photovoltaic (PV) effect, electrical power can be obtained from sunlight. PV energy is likely to become one of the largest – if not the largest, source of electricity production: sunlight, after all, is abundant, clean and free, while environmental concerns (and depleting stocks) are making the exploitation of more traditional sources such as fossil fuels unsustainable. PV energy production is extremely modular, being able to produce watts or megawatts under essentially the same configuration. It is versatile, both a potential world-scale energy source and a suitable solution for numerous small powering problems. It can be integrated in city buildings or in remote dwellings with no access to conventional electricity and is both inexhaustible and clean. Moreover, stand-alone PV systems produce power independently of the utility grid. In some off-the-grid locations even one half kilometer from power lines, stand-alone PV systems can be more cost-effective than extending power lines.

The year 2011 was a record year for the solar PV industry, with more than 29 GW of new capacity installed worldwide, corresponding to a 70% increase compared to 2010. Global PV capacity exceeded 69 GW in 2011, with 70% installed in European countries. The United States accounted for only 6% of capacity additions (nearly 1.9 GW) and 6% of total installed capacity (4.5 GW). Nevertheless, utilities and non-residential PV installations are growing steadily and in 2011 they accounted for more than half of the new PV capacity installed. The United States aims to raise new capacity installed every year to 2.8 GW in 2012, to more than 5 GW in 2014 and to 8 GW in 2016, reaching 15% of the global PV new installations. By contrast, in Japan, over 1.4 GW were installed in 2011, which corresponds to a 45% growth [1].

The 2011 boom is continuing the strong development which occurred over the last ten years. This expansion has two main drivers: falling PV module prices and strong support policies. PV continues to prove its ability to compete in the energy sector as mainstream power generation source.

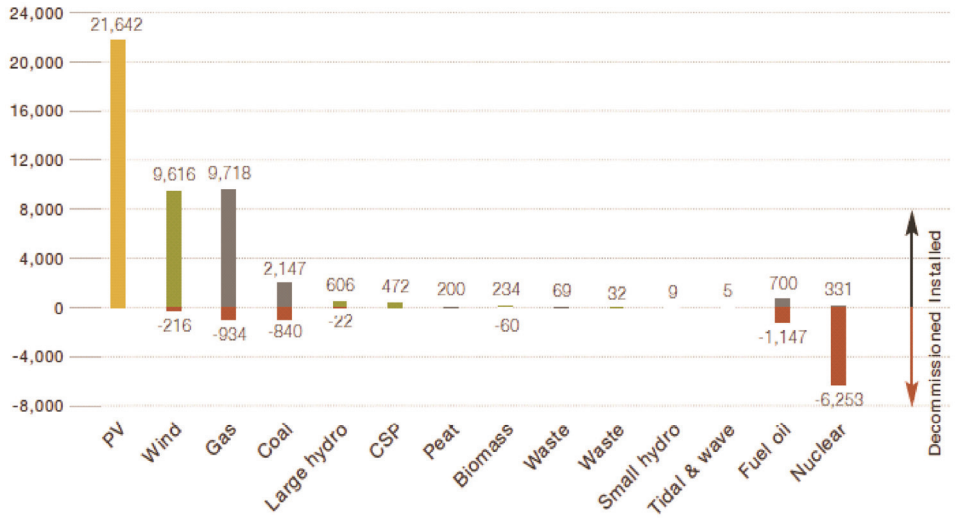

Figure 1.1 Power generation capacities added in Europe in 2011 (MW) (source: EPIA, EWEA)

What is the trend for 2012 and beyond?

Preliminary data for 2012 promise a strong development of capacity in new markets with sustained incentive policies. The US announced an increase of solar PV installations by 85% for the first quarter of 2012 compared to the first quarter of 2011 and plans for PV installations to exceed 3,200 MW in 2012: i.e. 75% greater than last year's total. China for its part expects capacity additions of about 4-5 GW in 2012. The market will be slower in Europe due to additional cuts in solar subsidies. Italy is expecting a further 1500 MW-2500 MW in 2012 alone compared to 9 GW in 2009.

Looking at a longer-term perspective, the European Photovoltaic Industry Association (EPIA) expects the globally installed PV capacity to reach 150 GW by 2015 (up to 200 GW in the policy-driven scenario). According to EPIA, the growth in world installed capacity will still be triggered by the European market (50 to 85 GW by 2015) but its share in the global capacity will decrease from around 75% to less than 60%; the share of North America is expected to rise from 7% to 17% between 2011 and 2015 and that of China from 4% to 8-10%. The effective capacity could be further developed if the 2010-2011 trends continue [1].

With the energy demand continually increasing, along with the need for new and clean energy sources, solar energy will definitely be an important part of the future energy mix. The challenge may seem daunting and solar energy remains rather controversial in the public debate about energy policy. Nevertheless, the fact that the global market for PV has continued to grow even in times of economic crisis shows there is a demand that can withstand a difficult period. With proper policy support, balanced market development, and continued industry innovation, the world's most promising source of electricity can continue its remarkable growth rate over the short-, medium- and long-term, and even beyond .

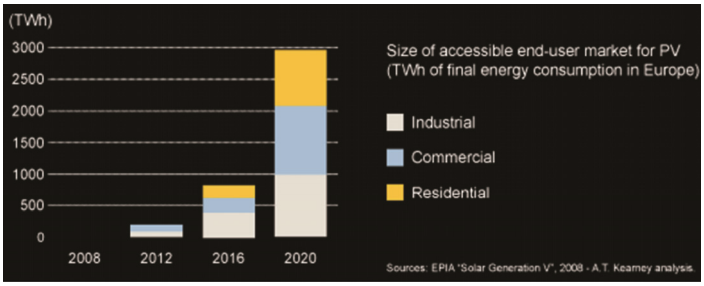

Figure 1.2 PV growth scenario until 2020 (source: EPIA)

1.2 Third generation photovoltaic solar cells

The single junction Si devices known as first generation PV cells have dominated the solar cell market with the limit of energy conversion efficiency between 31 and 41%, depending on the concentration of incoming sunlight. The second generation, which occupies a much smaller segment of the PV market, shares the same efficiency limit as the first generation solar cells, but promises a lower cost, thanks to reduced raw material usage and high throughput of manufacturing. Second generation PVs are based on amorphous Si, CdTe, CuIn (Ga)Se (CIGS) or polycrystalline Si thin films [2].

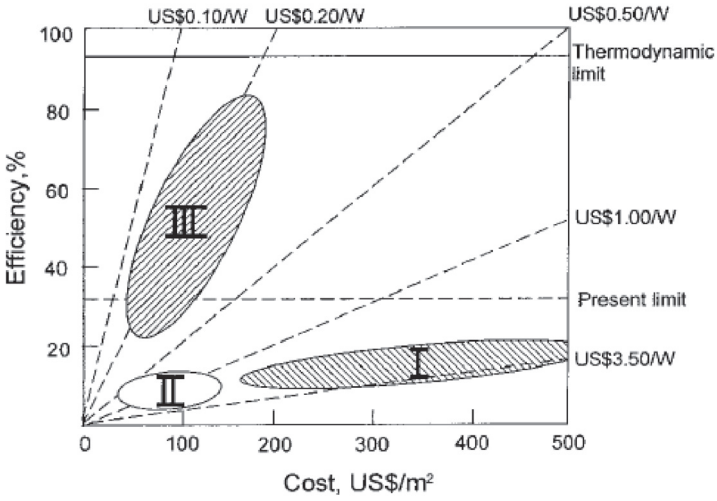

Figure 1.3 Efficiency and cost projections for first, second and third generation PV technology (wafers, thin-films, and advanced thin-films, respectively) [3].

The third generation PV cells are attempts to combine the advantages of both the first and the second devices. The idea behind the devices, is to circumvent the Shockley-Queisser limit for single-band gap devices, by multiple energy threshold approaches using thin-film processes and readily available nontoxic materials [2,3,4]. Such an approach can be realized by several designs: tandem cells, hot-carrier cells, multiple quantum well solar cells and, more recently, PV cells based on excitations between semiconductor energy bands - apart from the conventionally used valence and conduction bands. Among many strategies to design the cell structures, semiconductor quantum dots (QDs), also known as nanocrystals (NCs), have been applied to several of these approaches because of the extra degrees of freedom they give in the design of materials systems. Si QDs are particularly interesting because of the Si

availability and the wealth of experience in the processing of the material, as well as the relatively cheap and low-energy consumption of many of the thin-film manufacturing processes. The use of Si QDs can facilitate engineering of the material band gap and allow cheaper tandem cells to be made using thin-film processes.

1.3 Applications of semiconductor QDs in photovoltaic solar cells

The semiconductor QDs typically have diameters from about 2 to 10 nm and contain only hundreds to thousands of atoms. In this confined regime, there are several effects playing an important role such as quantum confinement, band folding and surface effects [5]. Semiconductor QDs used in the third generation PV cells have the potential to increase dramatically the efficiency of converting sunlight to electricity. The conversion process works via a Multiple Exciton Generation (MEG) process, in which when a single photon of light, of sufficient energy is absorbed by the QD, it produces more than one bound electron-hole pair, or exciton (Fig. 1.4). In contrast, conventional PV cells have bulk material properties, where a single photon produces a single electron-hole pair. MEG represents a promising route to increasing solar conversion efficiencies in PV cells. While MEG has been previously reported in direct-gap semiconductor NCs of PbSe, PbS, PbTe, CdSe, and InAs, Beard et al. have recently found that the threshold photon energy for MEG in 9.5 nm diameter Si NCs (effective band gap E_g = 1.2 eV) is $2.4E_g$ [6], compared to $3.5E_g$ in bulk Si. Because there are very few solar photons above 3.5 E_g, this lower threshold energy in Si NCs is a useful approach for enhancing PV efficiencies. This finding is of particular importance because Si dominates the PV solar cell industry, presents no problems regarding abundance and accessibility within the Earth's crust, and poses no significant environmental problems regarding toxicity. More importantly, highly efficient MEG in Si NCs at lower photon energies in the visible region (compared to bulk Si) has the potential to increase power conversion efficiency in Si-based PV cells toward a thermodynamic limit of ~ 44% at standard air mass coefficient AM1.5 solar intensity [6].

QDs exhibit other interesting trends in addition to MEG, e.g. varying the size of QDs can tune them to different wavelengths of light to optimize their performance. In essence, QDs can be tailored to absorb or emit specific wavelengths of light simply by changing the size of the dot [5]. Compared with bulk materials, which have larger crystals and more atoms than nanomaterials, the light spectra emitted or absorbed by QDs will shift to the blue, which

represents greater energy or shorter wavelength. Thus the smaller the dot, the greater the energy shift.

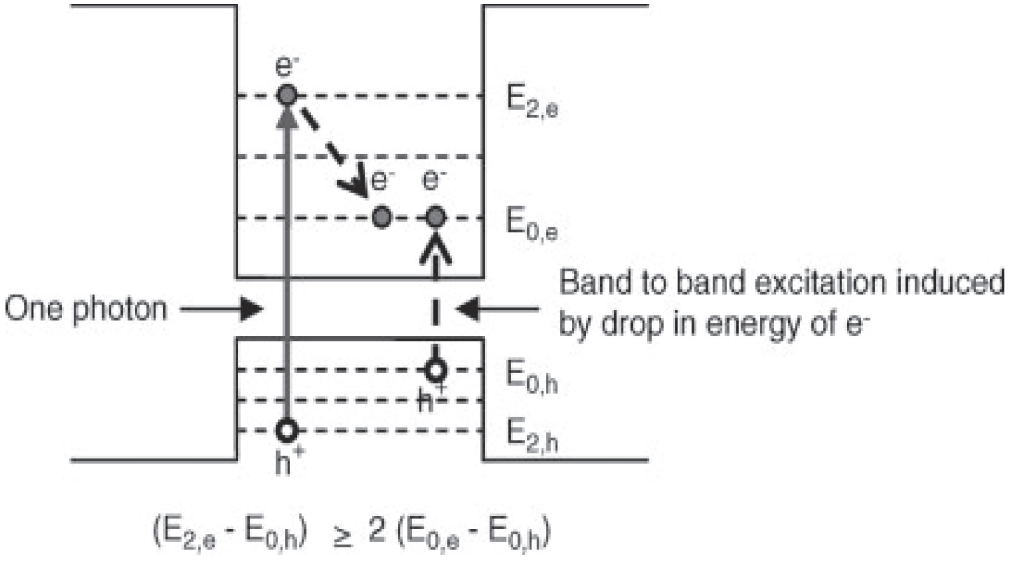

Figure 1.4 Multiple exciton generation in QDs: a high-energy photon is absorbed at a high confined energy level in the QD that then decays into two or more electron–hole pairs at the first confined energy level. Energy is conserved but momentum conservation in QDs is relaxed [7].

Taking advantage of both these effects – MEG and energy tuning due to size of the NCs – QDs can be incorporated into third generation solar cells. As pioneered by Green, a tandem cell design using only Si as a basic material, so-called all Si tandem solar cells, has been demonstrated to be a very attractive option [3]. A typical structure of such tandem cells involves a superlattice of thin film cells with different effective band gaps stacked together (Fig. 1.5). These effective band gaps can be controlled by changing the size of the Si QDs embedded in a higher band gap material, such as silicon oxide or nitride. By design, the upper cells should have a higher gap energy, which attenuates gradually from the top to the bottom cell in order to maximize the sun light absorption. Si has a band gap which is close to optimal not only for a standard, single p-n junction cell but also for the bottom cell in a 2-cell or even a 3-cell tandem stack. The radiative efficiency limit for a single junction silicon cell is 29%, which increases to 42.5% and 47.5% for 2-cell and 3-cell tandem stacks respectively. The optimal band gap of the top cell is 1.7 eV ~1.8 eV, for a 2-cell tandem with a Si bottom cell

and 1.5 eV and 2.0 eV for the middle and upper cells for a 3-cell tandem as shown in Fig. 1.5. This means that Si QDs can potentially be used in QD solar cells to produce much higher efficiencies and lower cost PV using a readily available and environmentally friendly material. Theoretical and experimental work will open the door to the potential application of QDs to greatly enhance the conversion efficiency of solar cells based on Si and other semiconductor materials. This is a key step toward making solar electricity and fuels more efficient and cost competitive with conventional power sources.

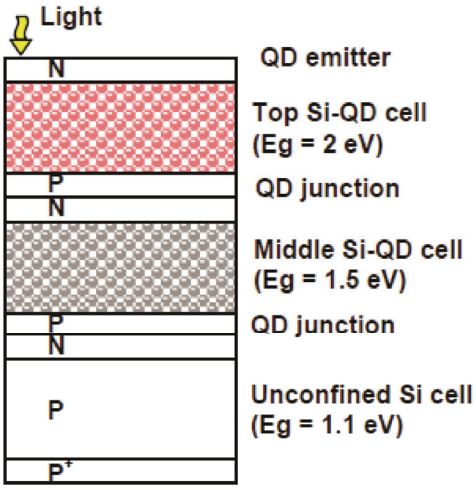

Figure 1.5 Schematic of "all-silicon" tandem solar cell [8].

1.4 Theoretical model of quantum confinement in nanocrystals

In nanocrystalline structures, confinement occurs in all three dimensions, resulting in the blue shift of the characteristic transition energies such as interband, intraband, excitonic, plasmonic and phonon optical transitions. As the radius *R* of the NC becomes very small, the energy levels of carriers change from continuous bands to a ladder of discrete levels (Fig. 1.6). There is an enhanced volume-normalized oscillator strength of exciton features as *R* is reduced. This enhancement arises because the oscillator strength becomes concentrated over sharp electron – hole transitions, rather than being distributed over a continuum of states, as for the case of bulk semiconductors. Most theoretical treatments assume spherical shapes for the crystallite, a rather reasonable approximation in most cases.

There have been many theoretical approaches to calculate the energy levels of semiconductor NCs, among which the first and simplest method used the effective mass approximation (EMA) model [9, 10], which assumes parabolic bands and infinite potential wells at the surface of a spherical NC and considers three cases involving the average crystallite radius R and the exciton Bohr radius $\boldsymbol{a_B}$ of the bulk semiconductor. The main energy terms are the electron-hole interaction energy (Coulomb term) and the confinement energy of the electron and hole (kinetic energy term). This method is only of partial used in determining the absolute confined energy levels for small NCs. It does, however, correctly model the trend and relative increase in confined energy level as QD size decreases [9]. The three EMA regimes are:

(a) ***Weak confinement*** ($R \geq a_B$ when $R \geq a_e$, a_h , where a_e and a_h are the electron and hole Bohr radius, respectively): the character of the exciton as a quasi-particle is preserved, and it is the translational degrees of freedom of the exciton that are modified because of the size quantization of the excitons. The dominant energy is the Coulomb term and the result of this is a small increase in the exciton energy, and the features in the optical spectra move slightly to the blue. The lowest-energy state is then the exciton state whose energy is shifted to higher energies by confinement, the shift in energy being proportional to $1/R^2$. The shift ΔE in energy of the ground-state exciton is given by [9, 10]:

$$\Delta E = \frac{\hbar^2 \pi^2}{2MR^2} \qquad (1)$$

where M, the mass of the exciton, is given by $M = m_e^* + m_h^*$, where m_e^* and m_h^* is the effective masses of the electron and hole respectively.

(b) ***Medium confinement*** ($a_h \leq R \leq a_e$): this is the usual situation for very small nanocrystallites, because of the large difference between the effective mass between the electron and the much '*heavier*' hole. In this case, confinement is assumed to be important for the motion of the electrons, but Coulomb forces between electrons and holes will influence the motion of the holes. The holes essentially move in a cloud of strongly confined electrons, which produce a mean Coulomb potential. The blue shift in the position of the maximum of the optical absorption coefficient will as a consequence vary roughly as [9, 10]:

$$\Delta E = \frac{\hbar^2 \pi^2}{2m_e^* R^2} \qquad (2)$$

(c) ***Strong confinement*** ($R \leq a_e,\ a_h$): the Coulomb term is small and can be ignored, or treated as a perturbation. The electrons and holes can be thought of as confined independent particles; excitons are not formed, and separate size quantization of the electron and hole is the dominant factor. The optical spectra should then consist of a series of lines due to transitions between sub-bands. Again, it has been shown that there is qualitative agreement with experiment, and the simple model gives the shift in energy as a function of crystallite size as [9, 10]:

$$\Delta E = \frac{\hbar^2 \pi^2}{2\mu R^2} \tag{3}$$

where μ is the reduced exciton mass given by

$$\frac{1}{m_e^*} + \frac{1}{m_h^*} = \frac{1}{\mu} \tag{4}$$

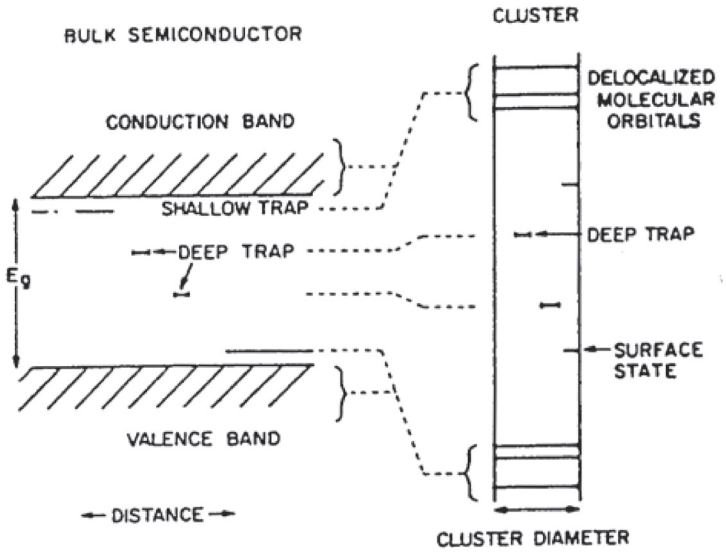

Figure 1.6 Schematic energy level diagram for the bulk semiconductor and for quantum dots [9].

Comparing with experimental results, it is found that the EMA overestimates the energy shift for small QDs [9]. This breakdown is not surprising as the Bloch assumption in the EMA of a carrier wave function varying only very gradually across the periodic potential of the lattice is no longer valid when the wave function is associated with a small spatial volume approaching

the size of the lattice spacing, as in a small QD [7]. It should be possible to calibrate a modified effective mass using Gaussian modeling, in order to modify the EMA. This parameter will vary with the QD size and with the species at the interface, as for small QDs the lowest energy states dominate the confined energy levels.

One of the problems met on the experimental side due to preparation techniques is the distribution of NC sizes in the samples [11]. Therefore, experimental approaches have to address this factor. In order to apply the theoretical model to experimental results, there are a few things that need to be taken into account. First, for the systems of the semiconductor NCs embedded in dielectric matrix, the NC size should be compared to the calculated bulk exciton Bohr radius corresponding to that material [9]. Second, semiconductors which have open-type structure such as tetrahedral in the case of Si and Ge, appear to divide into two categories. For the NCs containing less than 50 atoms, their structure can transform from tetrahedral to fcc structure [12, 13]. For the larger NCs a change to the open covalent diamond type structure may take place [13]. Third, for the very small NCs the proportion of surface atoms relative to the bulk will be high, and that might be a surface reconstruction, which cause deviation from the theoretical predictions [14, 15].

1.5 Si and Ge nanostructures

Initial attempts of forming NCs in dielectric matrices have largely focused on direct band gap semiconductor materials, such as group II-VI. In contrast to direct band gap materials, group IV of Si and Ge have an indirect gap, hence they are not an efficient emitter of light under optical or electrical excitation. They normally emit only weak near-infrared light and no visible luminescence. However, since the early of 1990s, Si and Ge NCs have attracted much interest due to strong visible photoluminescence at room temperature [16, 17]. Additional electrical studies of these systems have revealed several interesting properties. For instance, Si NCs can be used in Si photonics with on-chip incorporation of optical functions within existing microelectronics CMOS technology [18]. These systems have also shown nonlinear optical effects, potentially paving the way for nonlinear photonics with a wide range of applications such as sensing, high rate signal processing and broad band optical modulation [19]. In addition, Si oxide and nitride films are an integral part of existing solar cell technology and embedded Ge and Si NCs offer a route to creating stacked variable band gap structures [20].

1.5.1 Band structure modification in Si and Ge nanocrystals

At room temperature bulk Si has an indirect energy gap E_g = 1.14 eV ($\Gamma'_{25} - \Delta$) and a direct gap E_o = 2 eV ($\Gamma'_{25} - \Gamma'_{15}$) [21]. In comparison with Si, Ge has a larger dielectric constant and smaller effective masses for electrons and holes. The energy difference between the indirect gap ($\Gamma'_{25} - L_1 = E_g$ = 0.66 eV at 300 K) and the direct gap ($\Gamma'_{25} - \Gamma'_2 = E_o$ = 0.8 eV) is ΔE =0.12 eV, which is smaller than that of Si [21, 22] (Fig. 1.7). In addition, the effective Bohr radius of Ge is about 24 nm, which is much larger than that of Si (~ 5 nm). These electronic conditions lead to the expectation that it is much easier to change the electronic structure around the band gap of Ge and the possibility to engineer the band structure of Ge into a direct band gap is thus greater. One of the most effective means to convert an indirect optical transition into a direct optical transition is to form a nanostructure, such as an isolated quantum dot, by which the size of the Brillouin zone is reduced and the conduction-band bottom is folded onto the Γ point, resulting in a direct-gap material. If the envelope functions of carriers confined in a nanostructure have a sizable Fourier component at the wave vector corresponding to the indirect-gap transition, that Fourier component plays the same role as phonons in the bulk material and the direct optical transition becomes allowed [23]. However, one should keep in mind that very small NCs can have different geometries from the bulk structure because of surface reconstruction and structural changes, and this could result in more compact geometries and the breakdown of all theoretical model predictions.

Although the band gap of bulk Ge ~0.66 eV is smaller than that of bulk Si ~1.17 eV, it is predicted that small Ge QDs would have a larger band gap than Si dots of the same size. This predicted crossing of the optical gap, existing at a size of ~3.1 nm [24], raises the promise of easier access to blue light emission using Ge instead of Si dots (Fig. 1.8). However, there is still an ongoing and vibrant discussion about quantum confinement (QC) in Ge NCs [25]. The empirical tight binding calculation predicts stronger QC effects in Ge compared to Si [26]. In contrast to these calculations, another theoretical approach utilizing the empirical pseudopotential method predicts that the band gaps of Ge and Si should be similar upon size reduction [27]. The predicted similarities in the electronic structure of Si and Ge are explained with size-dependent structural changes in the conduction band of Ge: the conduction band minimum is found to move from the *L* point to the *X* point for reduced particle sizes and thus the Ge conduction band minimum becomes Si-like for small sizes. Therefore, from the experimental point of view, it is of interest to study and compare the

electronic structures and quantum behaviors of Ge and Si NCs in the same experimental conditions in order to confirm or rule out these points. This is discussed in detail in Paper III.

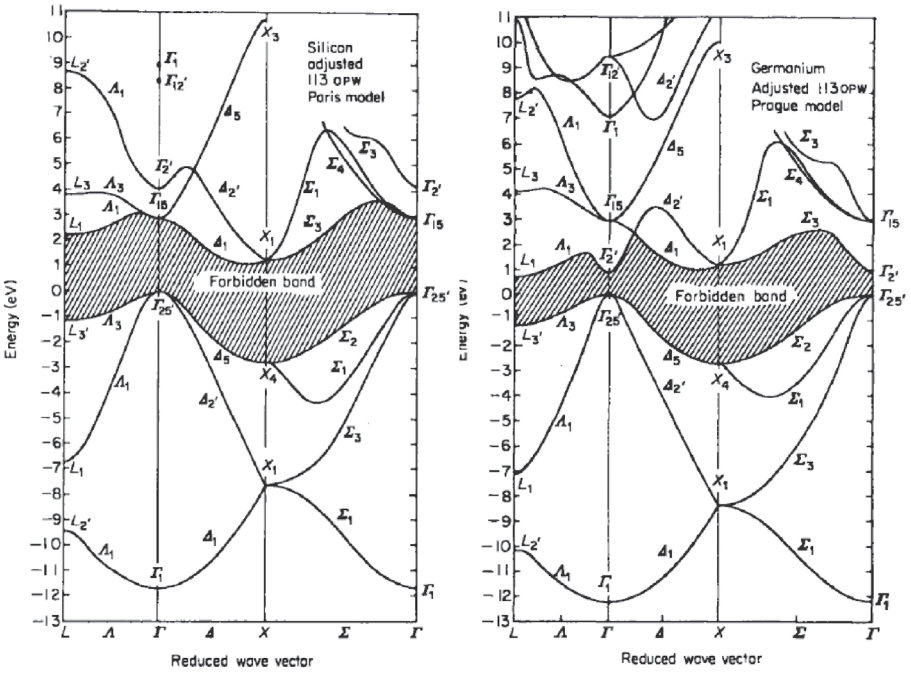

Figure 1.7 Energy band structure of Si and Ge (spin-orbit splitting neglected) calculated by the first-principles method [21].

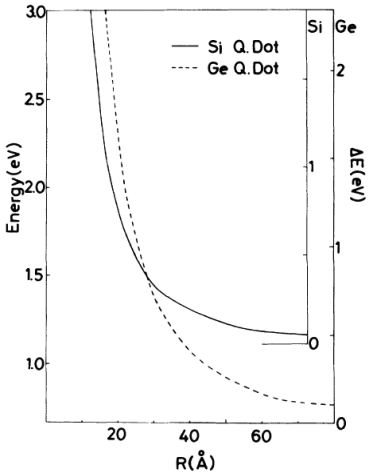

Figure 1.8 The calculated exciton energy in quantum dots (using the EMA method) is plotted as a function of the dot radius for Si (solid line) and Ge (dashed line). The right ordinate indicates the confinement energy ΔE measured from the indirect band-gap energy of the bulk material [23].

1.5.2 Impact of the dielectric matrix

In order to tailor the band gap of semiconductor QDs, it requires an ensemble of QDs isolated from each other by a close enough distance to allow for the overlap of their electron wave functions. The wave function of an electron confined to a spherical dot penetrates into the surrounding material, decreasing exponentially into the barrier. The slope of this exponential decay and hence the barrier to tunneling between QDs is reduced for a lower barrier height material [7]. With appreciable overlap of electron wave functions of adjacent potential wells, energy minibands may form, thus creating a superlattice. For Si and Ge QDs, this can be achieved by embedding the QDs in a higher band gap material such as Si oxide or nitride. The schematic of the bulk band alignments for Si with Si_3N_4 and SiO_2 matrix is shown in Fig. 1.9. The choice of barrier material should be a compromise between degree of confinement and ability for carrier transport. This is because a higher potential barrier results in enhanced confinement but it also reduces the penetration of the electron wave function into the barrier, thus lowering the transmission or tunneling probability [7]. A higher potential barrier would reduce the overlap of wave functions from adjacent potential wells and inhibit the formation of minibands. Since Si_3N_4 offers a lower barrier than SiO_2 it allows larger dot spacing for a given tunneling current. Hence, transport between dots can be significantly increased by

using alternative matrices with a lower barrier height, and hence increasing spacing between QDs to give the same effective transport [7].

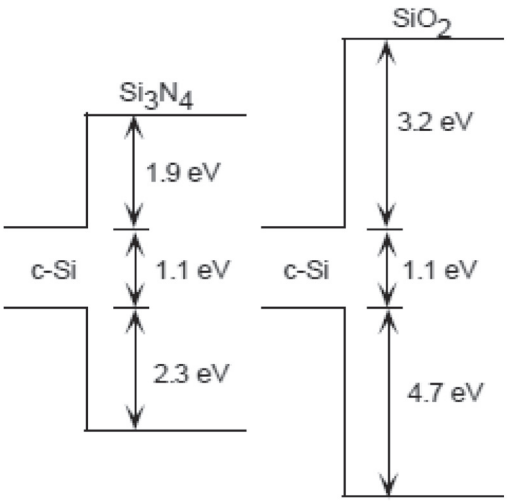

Figure 1.9 Bulk band alignments between crystalline Si and its nitride and oxide [7].

In addition, it has been reported by Conibeer [7] that compared to high polar Si-O bonds in SiO_2 matrix, the nonpolar Si-N bonds in Si_3N_4 matrix will not dramatically affect the QC energies. Therefore, the observed QC trend in the case of silicon nitride is well described by the EMA. Figure 1.10 show the photoluminescence (PL) results for Si QDs from different works [28,29-34] and the present work. For the same matrix systems the results are in good agreement, but are quite different for different matrix systems. The EMA predicts well the PL energy for Si QDs in SiN_x, but in turn overestimates the PL energy for Si QDs in Si dioxide, particularly for the smaller QDs. As shown by the calculations of König et al. [35], with increasing polarity of the Si interface bonds, the highest occupied molecular orbital (HOMO)-lowest unoccupied molecular orbital (LUMO)-gaps depend less on QC but more on the chemical nature of the interface itself. They estimated that for Si cores consisting of $\geq$10 Si atoms, the interface governs the electronic structure with QC competing for covalent and weak polar interface terminations, but being only a secondary effect for strong polar interface terminations. This explains why interface effects are more dominant for the QDs embedded in SiO_2 compared to the Si_3N_4 based systems.

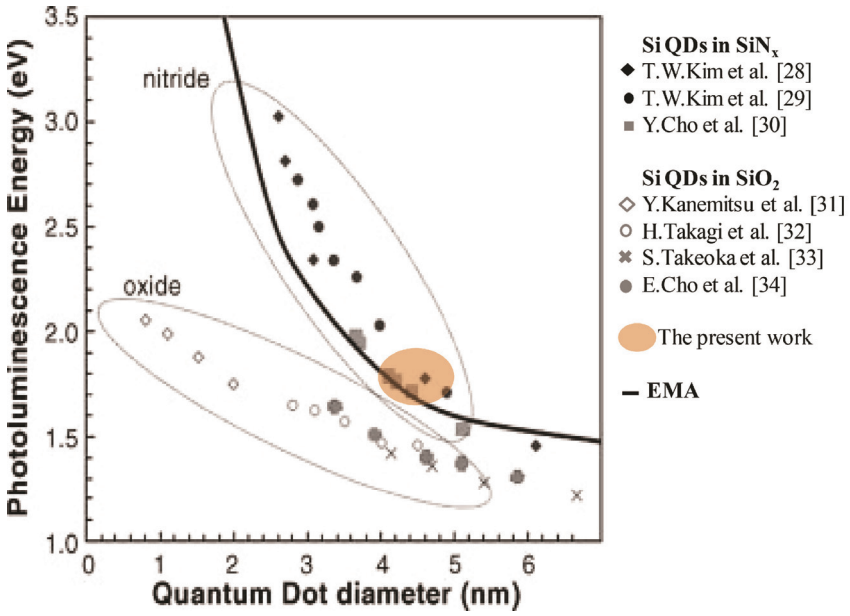

Figure 1.10 Measured photoluminescence energies for various authors data [28,29-34] and the present work for Si QDs in SiO_2 and SiN_x (300 K) as a function of QD size. Also shown is the EMA calculation for spherical dots [7].

1.5.3 Luminescence properties of Si and Ge nanocrystals

Much attention has been paid to the visible photoluminescence (PL) from Si and Ge QDs. QC theory leads to an expectation that this visible PL is made possible by band gap widening due to quantized levels and significant modulation of the usual electronic band structure in the band gaps, such as the change from an indirect gap to a direct gap, so that radiative efficiency may be enhanced at room temperature [5]. However, there is still an ongoing debate regarding the interpretations of optical spectra of the QDs embedded in a dielectric matrix, since the interpretations were often naïve and oversimplified. In fact, it has been difficult to identify the exact mechanism responsible for the PL response of these systems. Three mechanisms are thought to yield luminescence in this system under optical excitation: i) radiative electron–hole recombination in the NCs arising from QC effects [36], ii) radiative recombination at defect centers in the matrix network [37] and iii) radiative recombination at localized bonding states at the NCs/matrix interfaces, which may vary upon different preparation techniques [38]. Not only can all three of these distinct mechanisms be involved

at the same time in the PL process, non-radiative recombination processes and excitation energy transfer between different centers may also play a part.

1.5.3.1 Intrinsic emissions

Regarding the intrinsic luminescence properties of the NCs, Kim et al. [29] reported for a series of Si NCs embedded in Si nitride matrix films that when the Si crystal size was decreased from 6.1 to 2.6 nm, the PL peak energy blue shifted from 1.46 eV to 3.02 eV due to QC effects. The energy gap (*E*) of Si NCs can in the EMA be expressed as $E = E_{bulk}+C/d^2$ where d is the diameter of the Si NCs [16, 28, 29]. According to Kim et al. [29] $E\ (eV) = 1.16 + 11.8/d^2$. Maeda et al. [39] have fabricated Ge NCs embedded in SiO_2 glassy matrices by the radio frequency (RF) magnetron co-sputtering technique. They reported a strong room temperature luminescence with a peak at 2.18 eV for the Ge NCs of about 3 nm and concluded that it is consistent with QC of electrons and holes. In another later work of Maeda [22], Ge NCs in the size range of 2-6 nm were made. A blue shift of PL energy from 2-2.3 eV with decreasing NC size was observed, which was attributed to QC effects in Ge NCs. Hayashi et al. [40] reported a very clear blueshift of the optical absorption edge for Ge NCs embedded in SiO_2 matrix as the average crystallite size decreased, which seems to be due to a quantum size effect. However, such a clear size dependence of the PL peak energy has not been observed yet. Its absence has been considered to be due to a very broad spectrum coming from size inhomogeneity or the inherent electronic band structure in Ge or due to a large difference between the absorption and radiation procedures [40]. In the present work, it was found that Si NCs with a mean size of 4–5 nm give rise to the PL peak energy at ~ 1.76–1.79 eV (Paper II), which is in agreement with the result reported by Kim et al. [29].

1.5.3.2 Defect emissions

Radiative emission can also come from localized defect states lying inside the band gap [41]. Depending on the type of defect or impurity, the state can act as a donor (has excess electrons) or an acceptor (has a deficit of electrons). Electrons or holes are attracted to these sites of deficient or excess local charge due to Coulombic attraction. These defect states can be categorized into either shallow or deep levels, where shallow level defect states have energies near the conduction band or valence band-edge. Defect states are expected at the surface of a QD despite the use of various passivation methods, because of the large surface-to-volume ratio [26, 41, 42]. The concentration of surface states on the QDs is a function of the synthesis and passivation processes. These surface states act as traps for charge carriers and excitons, which generally degrade the optical and electrical properties by increasing the

rate of nonradiative recombination [43]. In addition to surface states, recent experiments and calculations indicate that amorphous silicon nitride and oxide matrix is photoluminescent on its own, i.e., even when the NCs are not present in the sample [38, 44]. The PL energy varies according to the concentration of the matrix compounds, i.e. the Si:O or Si:N ratios [38, 45]. This effect increases the complexity of determining the origins of emission of QDs in luminescent matrix composite materials.

1.5.3.3 Extrinsic emissions

Luminescence might also arise from unintentionally incorporated impurities, which is called extrinsic luminescence. The predominant radiative mechanism in extrinsic luminescence is electron-hole recombination, which can occur via transitions from conduction band to acceptor state, donor state to valance band or donor state to acceptor state. Especially in the case of amorphous silicon nitride thin films, where the inherent porous structure of the film is very likely to incorporate O into its network, a noticeable amount of Si-O bonds were reported by Liao et al. [46]. These Si-O bonds will create a gap state of Si–O above the valence band maximum of Si_3N_4 and will lead to the $\equiv Si^0 \rightarrow \equiv Si–O–Si$ transition. Huang et al. [47] reported that the blue emission peak at around 2.5 eV in amorphous Si nitride films that have been partially oxidized, originates from localized states related to Si–O bonds. Its intensity was shown to be strongly dependent on the Si–O bonds concentration. Furthermore, Liu *et al.* [48] reported that due to the presence of O in silicon-rich silicon nitride (SRN) films, Si–O bonds give rise to the 2.55 eV emission. In the present work, the contribution from the emission band related to the gap state of Si–O bonds was found at ~2.54-2.69 eV and it increased with the O content in the SRN films. This is discussed in detail in Paper II.

In short, the radiative emissions of QDs embedded in dielectric matrices originate from rather complicated and overlapping processes. In order to understand completely the role of various radiative centers contributing to the luminescence, the knowledge of sample preparation, chemical composition and theoretical models is demanded. In addition, complimentary techniques must be applied simultaneously in order to experimentally verify a clear correlation between structural and optical properties.

Chapter 2

The synthesis and formation of Si and Ge nanocrystals embedded in dielectric matrices

The properties of Si and Ge NCs can be controlled by their size, shape, density, surface termination, and so on. In the present work, the size, density and structure of Si and Ge NCs embedded in SiO_2 and Si_3N_4 thin films have been controlled during sputtering and thermal annealing processes. In addition to inherent properties of the materials, unintentional incorporation of contamination such as O and metallic elements has introduced undesirable properties and structural modification into the films. These changes can lead to dramatic differences in their physical, optical and electrical properties. Great efforts have been spent to investigate the intrinsic and extrinsic structures and properties of the films by using a combination of different techniques. The present study is not only focused on the quantum size effects in the NCs, but also on the atomic, electronic structures and optical properties of the matrix surrounding the NCs. In this chapter, the fabrication of Si and Ge NCs embedded in nitride and oxide matrices will be described in detail. The experimental challenges and results will also be discussed.

2.1 Si NCs in silicon nitride thin films

Si NCs can be formed by precipitation from a Si excess solid solution of dielectric materials (oxide, nitride, carbide), which is commonly deposited in thin film process such as sputtering, plasma-enhanced chemical vapour deposition (PECVD) and reactive evaporation [8, 36, 49-52]. A substrate heating and/or a post-annealing process are needed for the formation of the NCs [53]. Once the NCs are formed, in addition to QC effects therein, the matrix also plays an important role on the resultant energy states. With increasing polarity of the bonds between the NCs and the matrix, there is an increasing dominance of the interface strain over QC. SiO_2 matrix has a stronger polarity in this respect compared to SiN_x [7, 35]. Therefore, SiN_x matrix can be a better option because the relatively non-polar Si-N bonds do not dramatically affect the QC. Moreover, transport properties between the NCs are expected to depend on the matrix in which the NCs are embedded. Different matrices produce different transport barriers between the Si NCs and the matrix, with tunneling probability heavily

dependent on the height of this barrier. Si_3N_4 gives lower barrier than SiO_2 allowing larger NC spacing for a given tunneling current, which is another important effect for the practical application of PV solar cells.

2.1.1 Si NCs grown by radio frequency (RF) magnetron sputtering

The Si-rich silicon nitride (SRN) thin films in the present work have been grown by the RF magnetron co-sputtering technique in a Minilab Deposition System type ST60A. A stoichiometric compound Si_3N_4 target and a pure Si target were placed in two different magnetron sources (cathode), which are both connected to rf voltage. Prior to sputtering, the chamber was evacuated to 5×10^{-7} mbar. *In situ* Ar pre-sputtering of the targets was performed in order to remove any silicon oxide on the target surfaces. The flow rate of Ar was maintained at a constant rate of 40 standard cubic centimeters per minute and the pressure in the chamber was kept at 6×10^{-3} mbar during the film deposition. The glow discharge was maintained under the application of rf voltage between the cathode and the anode (substrate). The Ar^+ ions generated in the glow discharge were accelerated at the cathode fall (target sheath) and bombarded the targets with high energy. The atoms on the target surfaces were sputtered and deposited on the substrate. In this magnetron sputtering system, a magnetic field is superposed on the cathode and glow discharge, which is parallel to the cathode surface. It acts as an electron trap to increase the plasma density, which leads to increase in the current density at the cathode target and effectively increases the sputtering rate. This enabled us to maintain the sputtering process at low pressure and doing so the sputtered particles traverse the discharge space without collisions, which resulted in a high deposition rate. By co-sputtering and deposition from Si and Si_3N_4 targets, the excess Si content in the SRN films was achieved without any intentional substrate heating. Various Si excess compositions were obtained by simply changing the rf power supplies to each targets, ranging from 50 to 100 W for both targets.

Si NCs can precipitate and crystallize in a single layer of Si rich silicon nitride (SRN) only if either the annealing temperature is high enough ($\geq 900^o$ C) or the Si excess is high enough. Ideally, in such conditions a complete phase separation can occur: SRN$\rightarrow$ Si + Si_3N_4. This assumption appears to be oversimplified, since practically the excess Si can precipitate partially, resulting in a matrix of non-stochiometric silicon nitride and/or coexistence of sub-nitride. The uncontrollable matrix composition can potentially affect the carrier transport

properties since different matrices produce different transport barriers between the NCs and the matrix.

For Si NCs growth thermally in a sputtered SRN film layer, the size, density, morphology and crystal quality of Si NCs can be controlled by varying the composition of the nitride layer during the depositions and the post-thermal-annealing conditions (atmosphere, temperature, time, heating rates). Within the framework of this thesis, the properties of Si NCs and their counterpart nitride matrices have been modified by altering the sputtered SRN film compositions as well as annealing temperatures and times. Thin films composed of a nominally stoichiometric Si nitride (Si_3N_4) buffer layer (~20 nm) followed by an SRN layer (~40 nm) were deposited on (100)-oriented single-crystal Si substrates by RF magnetron sputtering in an Ar atmosphere (Fig. 2.1). The Si substrates were cleaned using a standard RCA (Radio Corporation of America) cleaning process followed by a dip in a 10% HF solution to remove the native oxide, then put into the deposition chamber. With the purpose of forming Si NCs and induce phase separation in the nitride matrix, the samples were subsequently annealed in a sealed SiO_2 glass tube evacuated to a vacuum of better than 1×10^{-2} mbar. For a fixed composition of the SRN layers, the annealing temperatures and times were varied depending on the specific desired NC structures, ranging from 900 to 1100°C for 30 min to 2 h. For a fix annealing condition of 1100°C for 2 h, different Si excess in the SRN layers were achieved by adjusting the sputtering rates for the Si and Si_3N_4 targets individually. Transmission electron microscope (TEM) analysis shows that the mean size and size distribution of Si NCs increase with increasing the annealing temperature for the same annealing time, and with increasing the annealing time for a fixed annealing temperature. High temperature annealing for a short time favors the formation of NCs with small size and defect-free. Long annealing time leads to larger NCs size and annealing at low temperature results in NCs with small size but with defects.

Low- and core-loss Electron Energy Loss Spectroscopy (EELS) in the electron microscope (for more details see Chapter 3, 3.2.3 and 3.2.4) were used to probe the local chemistry of the silicon nitride matrix as well as electronic structure of the formed NCs. The energy position of the plasmon excitation peak found in the low-loss part of the EELS spectrum is directly related to the valence electron density (see 3.2.3). Any change in this quantity, for example due to chemical or structural changes in the material, can in principle be detected as a shift in the plasmon peak positions [54]. In this work, the plasmon peaks of the matrix surrounding the Si NCs, in the different samples mostly have energies in the range of 20 - 24 eV. This

indicates that the matrix is nonstoichiometric silicon nitride SiN_x ($x < 4/3$). It has been observed earlier by Gritsenko et al. [55] that for SRN, the plasmon energy decreases from 24 to 17 eV depending on the Si excess in SiN_x. The decrease of plasmon energy in SiN_x is attributed to the increase of Si-Si bond concentration. This result implies that Si agglomeration in the SiN_x films is not complete even after annealing at 1000 ^oC or above for a rather long time (30 minutes or more).

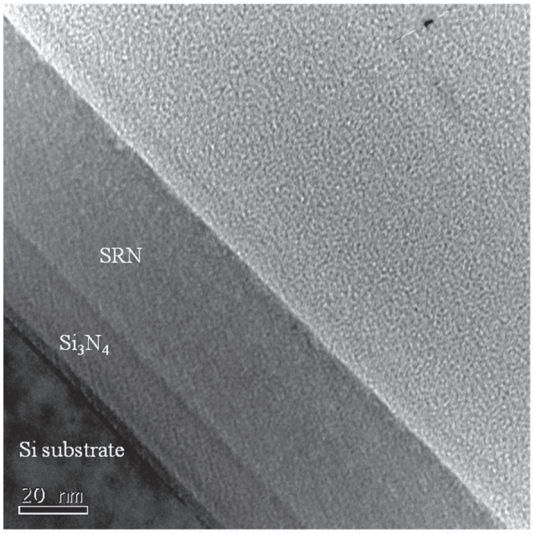

Figure 2.1 TEM image of the film structure including Si nitride (Si_3N_4) buffer layer (~20 nm) followed by an SRN layer (~40 nm) were deposited on (100)-oriented single-crystal Si substrates

Common defects formed in Si NCs such as twinning, stacking faults and dislocations are crucial to the electrical and optical properties of the materials. Batson has reported Si $2p_{3/2}$ EELS spectra from stacking faults at the substrate interface of a strained Si quantum well, which show splitting of the L_1 conduction band minimum caused by third-neighbor interactions at the fault and the spectra from the 30° partial dislocation show a similar splitting as well as in-gap defect electronic states [56]. In the present work, it is shown that the presence of lattice distortion, stacking faults, and dislocations inside the Si NCs can cause a weakening of quantum size effects and a reduction in the light emission efficiency of the films. The results are discussed in detail in Paper I of this dissertation.

It has been found by Liao et al. that Si nitride films produced by PECVD are easily oxidized by exposure to air after deposition [46]. This high reactivity was attributed to the porous structure of the observed films, which were typically fabricated at low substrate temperatures, as it likely that moisture from the air penetrates into them. A similar porous structure of as-sputtered nitride films has been observed by TEM in the present work; the nominal Si_3N_4 buffer layers show a higher density of pores than the SRN layers. Upon annealing these porous layers become denser, more so in the SRN. This leads to the conclusion that the degree of oxidation is proportional to the nitride content: the higher the nitride content, the more significant the amount of O found. As a result, different SRN compositions are expected to have dissimilar O incorporations in the films, resulting in dramatic change in stoichiometry and the film structures and properties. This was observed experimentally by XPS, PL and EELS as shown in Paper II and discussed therein.

2.1.2 Contamination issues during silicon nitride thin film fabrication

In the initial stages of this work, RF magnetron sputtering in the Minilab Deposition System was used to make multilayer thin films of alternating Si and Si_3N_4 on single crystal Si (001) substrates. The substrate was held at 400^{o}C during deposition and annealing was done at 1000^{o}C for 2 hours in vacuum. Under deposition of the films, sputtering also occurred from the target clamping rings of stainless steel. In this case, HRTEM/EFTEM imaging and XPS are very useful tools to detect and locate the contamination elements during the fabrication process. It was found that during annealing, chromium rich and iron rich phases crystallized. Cr quickly moved to the interface between the substrate and the film, where it crystallized as $CrSi_2$, as identified by electron diffraction and energy dispersive x-ray spectroscopy. Iron showed no preference of diffusing towards the substrate. The structure of $CrSi_2$ NCs and their orientation relation with the Si substrate were analyzed and discussed in detail in Paper IV. The formation and evolution of contamination nanoparticles, which are easily misinterpreted as Si NCs in the nitride films, were investigated thoroughly and should be taken into account when studying the structures of silicon-nitride thin films fabricated by RF magnetron sputtering. In order to prevent the contamination in this system, the target clamping ring of stainless steel was replaced by Al, since this material tends to form a surface of Al_2O_3, which has the lowest sputtering yield. This modification has been proven to be very efficient in this work, as no contamination was found in the films afterwards.

2.2 Ge NCs in silicon dioxide thin films

Intensive studies of Ge NCs embedded in a single layer SiO_2 film have been reported by many authors, including many methods, such as magnetron sputtering of Ge and SiO_2 [57-62], oxidation of Si_xGe_{1-x} alloys [63], molecular beam epitaxy [64, 65], Ge ion implantation [66], PECVD [67], electron beam irradiation [68], and electron beam evaporation [69]. Although the preparation methods are different, all the films fabricated have almost the same structure, i.e., Ge NCs randomly dispersed in a single layer SiO_2 film. In the co-sputtering technique, a target of SiO_2 with several pieces of Ge attached was usually applied [57, 59, 70]. The Ge content in the samples was then controlled by changing the amount of attached Ge pieces. In the present work, a slightly different experimental set up was employed: two different targets of SiO_2 and Ge were used for the co-sputtering process. This method has also been applied previously by other authors [62, 71].

Compared to the growth temperature of Si (1414^oC), a lower growth temperature of Ge NCs is predicted. Recently, it has been reported by Pinto et al. [72] that Ge NCs can be grown in SiO_2 at temperatures around 250^oC by in situ substrate heating during magnetron sputtering, while the typical temperature to form Si NCs is around 1100^oC. Despite these advantages, in practice, the fabrication and observation of Ge NCs was a more difficult task than of Si, due to the tendency to form defects, interfacial mixing, suboxide states, diffusion out of the film surface and moreover the NC structure was changed and/or damaged quickly by the electron beam irradiation in TEM/STEM experiments [68, 70, 71, 73]. Cosentino et al. [71] studied the influence of surfaces states on the photon absorption in films formed of Ge nanoclusters embedded in SiO_2 by magnetron co-sputtering of SiO_2 and Ge, in Ar atmosphere, followed by annealing at 600 – 800 °C in N_2. The authors found an optical band gap of 1.6 eV, independent of the quantum dot size for size in 2 − 10 nm range and the structural phase, amorphous or crystalline (diamond) of Ge nanoclusters. They showed how the absorption is influenced by surface states. The authors also observed the Ge out-diffusion through the surface. Shen et al. [70] obtained Ge NCs (2.1 – 27.2 nm) with diamond structure by co-sputtering of SiO_2 and Ge, followed by an annealing in N_2 at different temperatures (300 – 1100^oC). They remarked the out-diffusion of Ge atoms in the samples annealed at 1100^oC.

In the present work, the size, density and structure of Ge NCs were controlled via changing Ge concentration using RF magnetron sputtering in the Minilab Deposition System with an Ar atmosphere. The films were fabricated by co-sputtering and deposition from SiO_2 and Ge

targets without any intentional substrate heating. A four-layer structure thin film composed of an SiO_2 buffer layer followed by two SiGeO middle layers with different Ge contents and a capping SiO_2 layer was deposited on (100)-oriented single-crystal Si substrate. These layers are named as layers 1, 2, 3 and 4 as shown in Fig. 2.2. The different Ge content between layers 2 and 3 was achieved by adjusting the sputtering rate for the Ge target, while the sputtering rate for the SiO_2 target was kept constant. With the purpose of forming Ge NCs in the oxide matrix, the sample was subsequently annealed at 600 – 1000°C for 1 h in a sealed SiO_2 glass tube evacuated to a vacuum of better than 1×10^{-2} mbar. Figure 2.2 shows the structure of the film layers after annealing at 800°C for 1 h. It was found in the present work that the critical temperature for Ge NCs to be formed in SiO_2 matrix is around 800°C, below which uniform amorphous films were observed. A too high temperature leads to the oxidation and evaporation of Ge, as well as the formation of voids in the films.

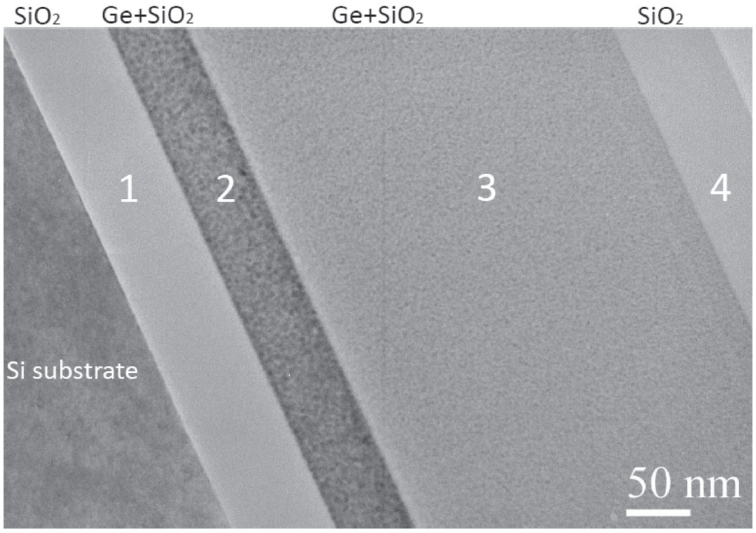

Figure 2.2 TEM image of the film structure including 4 layers, after annealing at 800°C for 1h.

The SiO_2 matrix is a supersaturated solid solution containing a large amount of excess Ge. When the samples were annealed at temperatures from 600 to 800° C, both an increase of Ge corresponding to precipitation of Ge NCs in the matrix and a decrease in the amount of GeO_2 occurred simultaneously. The thermodynamically possible reaction describing formation of elemental Ge in SiO_2 is: $GeO_2 + Si = Ge + SiO_2$. Previously, it has been reported that Si

atoms in the substrate is the large source for this reaction, as they diffuse from the substrate to the alloy film of $Si_{1-x}Ge_xO_2$ and the reaction took place close to the substrate/film interfaces [39, 62, 74]. Kolobov et al. [62] prepared films of Ge NCs (5 – 20 nm) embedded in SiO_2 also by co-sputtering of Ge and SiO_2, with a subsequent annealing at 800^oC in Ar. The films contain 25, 40 or 60 mol% of Ge in the SiO_2 matrix. The authors found that the size of NCs strongly depends on the type of the substrate used, quartz-glass or Si (100). Ge NCs with two shapes were observed, one spherical with multiple twinning defects and the other faceted single crystals. They have also evidenced a gradient of Ge NCs concentration with the depth of the film. At the film surface, there are no Ge NCs, and at the bottom part, i.e. at the interface with the Si substrate, a higher density of Ge NCs was evidenced. The authors observed the presence of single faceted NCs in the layer, whereas at the interface with the Si substrate, spherical NCs with multiple twinning defects are present. The films deposited on quartz substrates have Ge NCs with smaller sizes that form a continuous network.

Therefore, in the present work, the purpose of using the buffer layers of SiO_2 was to prevent the formation of Ge NCs close to the substrate, and the NCs grew spontaneously and uniformly within the bulk of layer 2 and 3. As expected, the NCs are nearly spherical in shape and uniformly distributed throughout the bulk of these layers, as shown in the high resolution transmission electron microscopy (HRTEM) imaging (Fig. 2.3). Layer 2 has a higher density and bigger grain size of Ge NCs (5 ~ 10 nm) than layer 3 (2 ~ 5nm). In addition, the SiO_2 capping layer is used to protect Ge from diffusing out of the film surfaces during the annealing. It was found in the present work that in the samples without capping layers, Ge evaporated completely after annealing at 1000^o C for 1 h.

The annealing atmosphere is crucial to the film structure evolution. Marstein et al. [75] have reported the mechanisms of void formation in Ge implanted SiO_2 films: Ge first segregates into NCs which then increase in size by diffusion and Oswald ripening. Ge is quite mobile in SiO_2, and O or moisture from the annealing atmosphere diffuse in from the surface, Ge will be bonded in an oxide closer to the surface than the precipitate. There is thus a net flux of Ge out of the nanoprecipitate into an oxide closer to the surface. The volume occupied by the Ge precipitate becomes a void. This is in agreement with the observations in the present work. When the samples were annealed at a poorer vacuum condition, voids were formed throughout the film structures and a dramatic reduction in Ge concentration was found.

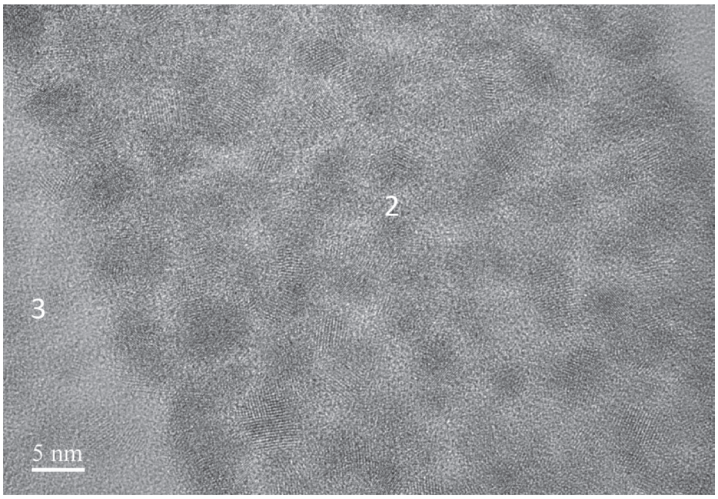

Figure 2.3 HRTEM image of Ge NCs embedded in SiO_2 matrix in layer 2.

While the growing mechanism of Ge NCs and its dependence on the Ge content are interesting topics that have been studied intensively, the research on quantum behaviors of individual NCs by using EELS is still lacking. This might be due to the fact that obtaining localized EELS from individual Ge NCs with very small sizes is a difficult task because of the radiation damage. It was found in the present work that if irradiated with a large enough dose, the NCs in layer 3 (< 5 nm) damage very rapidly and in some cases they appear to have 'dissolved' after the acquisition of EELS data. To rule out any over-interpretation due to sample damage, particular care was taken to exclude all the data points for which there was a suspicion of possible damage after beam irradiation. In the present work, experimental low-loss and core-loss STEM-EELS were used to study a number of phenomena related to QC in individual Ge NCs embedded in SiO_2 matrix. The observed phenomena include an apparent blue-shift in plasmon energies and an enhancement of Ge interband transitions with decreasing NC size. In order to facilitate the interpretation of the experimental results, theoretical simulations have also been carried out for similar confined nanostructures to predict possible behaviors of the excitations in the low-loss EELS and thus provide a clearer physical understanding. In addition to the quantum size effects, chemical states and electronic properties of the SiO_2 matrix as well as effects due to changes in the Ge crystal structure are also investigated and discussed. The results are discussed in detail in Paper III.

Chapter 3

Characterization methods

The purpose of this chapter is not to describe the detailed principles of the characterization methods, since this information can be found easily in textbooks. Instead, the experimental conditions and techniques that have been used for each instrument in the present work will be presented.

3.1 Imaging of nanostructures

3.1.1 High Resolution Transmission Electron Microscopy (HRTEM)

While X-ray diffraction and selected-area electron diffraction can provide accurate structural information averaged over the excited sample volume, they are incapable of providing information on the structure of individual NCs. On the other hand, HRTEM gives important information about crystal structure, size distribution and morphology of the individual NCs. HRTEM is also a powerful tool for studying the lattice distortion, stress and defects inside the NCs as shown in Paper I and other works [76-79]. The high-resolution detail in the micrograph arises from coherent interference between the central beam (unscattered plane wave) and all diffracted beams (scattered plane waves) by the specimen. The NCs, oriented along one of the low-index zone axes, show contrast variations that are perceived as periodic lattice fringe images and under certain conditions, they correspond to atom columns and can thus yield atomic-resolution images of the NCs. An important parameter to determine the NC structure is the inter-planar spacing d of the crystal planes. For a cubic crystal system, d spacing corresponding to each hkl Miller indices can be described by the following equation:

$$\frac{1}{d^2} = \frac{1}{a^2}\left(h^2 + k^2 + l^2\right) \tag{5}$$

where a is the lattice constant of the material.

In the present work, HRTEM is the main tool to investigate the structure of as-deposited thin films as well as the formation, structure and morphology of Si and Ge NCs in the films after thermal annealing. The HRTEM and energy-filtered transmission electron microscopy

(EFTEM) observations were performed at 200 keV primary beam energy with a JEOL 2010F microscope equipped with a Gatan Imaging Filter. HRTEM imaging of Si NCs in SiN_x matrix is a challenge due to very low contrast between the Si NCs and the nitride matrix, and the random orientation of the NCs. The contrast of HRTEM images depends severely on the sample's thickness and orientation relative to the beam direction. More importantly, the contrast transfer function (CTF) (Fig. 3.1) contains zeros and inversions meaning that some spatial frequencies present in the sample are not observed in the images and other spatial frequencies are imaged with reversed contrast. Therefore, there is a problem with unambiguous interpretation of individual high-resolution images and only under well-defined conditions may high-resolution images be naively interpreted in terms of the projected potential of the atomic columns aligned along the beam direction. As seen in Fig. 3.1, the most likely resolvable lattice fringes in Si and Ge correspond to (111) d spacing, because these spacing fall into the first passband of the CTF, where the effect of the envelope function is very small. In order to resolve smaller d spacing (e.g. (220) or (311)) the defocus setting needs to be changed to maximize the passband for a given frequency.

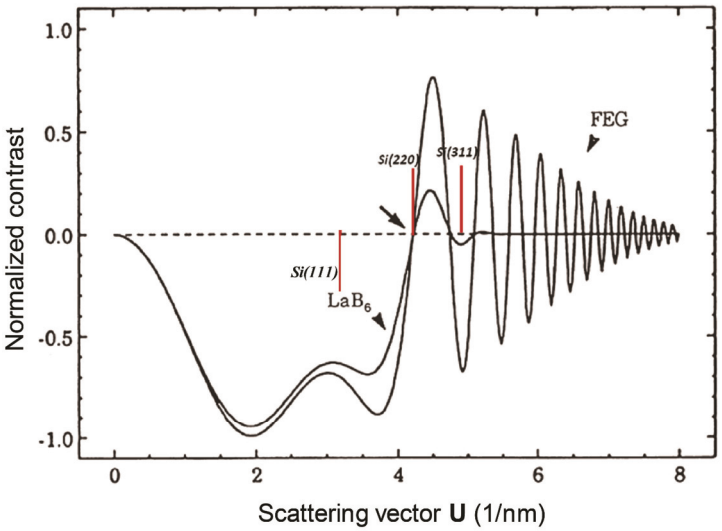

Figure 3.1 Contrast transfer function at the Scherzer defocus (maximum passband) for 200 kV HREM, comparing effect of the temporal coherence (energy spread) envelope on information transfer beyond the interpretable resolution limit. The Si(111) is in the first passband; Si(220) is at a point of zero contrast; Si(311) is in a passband with a positive contrast. [80]

3.1.2 Energy-filtered Transmission Electron Microscopy (EFTEM)

A potentially more efficient way to image the randomly oriented NCs simultaneously is using the energy-filtered imaging in the transmission electron microscope (EFTEM). The purpose of the energy filtering is to form images from electrons that have suffered a specific energy loss. An energy filter consists of an electron spectrometer with a mechanical slit in the energy-dispersive plane that is used for the selection of the energy loss of interest. Behind the slit either an energy-filtered image (or diffraction pattern) or an image of the energy-dispersive plane is formed by additional electron lenses. These lenses can be considered as a second projector lens system of the microscope. The images formed by this procedure provide information in a convenient form; e.g. a core-loss image can indicate the spatial distribution of a particular element.

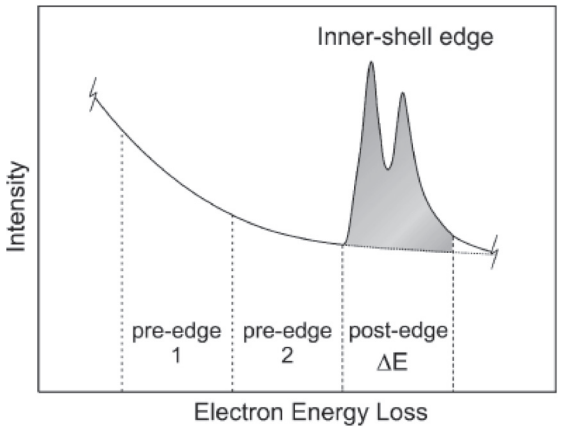

Figure 3.2 Three-window method used in EFTEM in order to obtain elemental distribution maps. Images using energy losses from the hatched areas are used for background subtraction. The signal is obtained from the third window above the edge onset.

EFTEM imaging for Si NCs in this work is typically acquired using plamon energy (low loss imaging) for bulk Si at 17 eV with an energy slit width of 2 eV or using the core-loss energy of Si-L edge at 99 eV, N-K edge at 401 eV and O-K edge at 532 eV (elemental mapping). When using the core-loss energy, a method called three-window method is employed, in which three images are sufficient to obtain a distribution map of a certain element: two from the pre-edge energy-loss range and one image from the post-edge area (Fig. 3.2). The pre-edge images are used for extrapolated background subtraction, which is then subtracted from the post-edge image to produce an elemental map. The EFTEM elemental mapping is a really

useful tool to map the distribution of elements in silicon nitride, oxide or oxy-nitride thin films. An example of that is shown in Fig. 3.3.

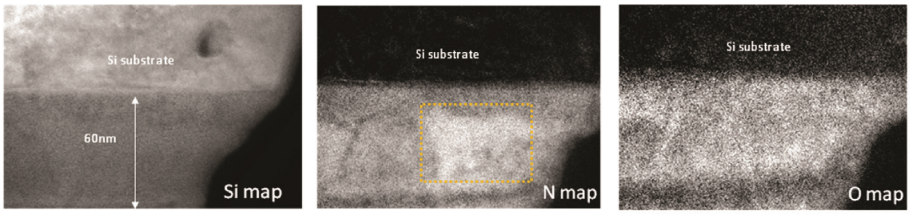

Figure 3.3 Elemental mapping of silicon nitride thin film (taken at Si-L, N-K and O-K edge), showing a uniform distribution of Si, and enrichment of N (dotted frame) as well as depletion of O at some area.

3.1.3 High-angle Annular Dark-field Scanning Transmission Electron Microscopy (HAADF-STEM)

Scanning transmission electron microscopy (STEM) is a technique where a focused electron beam is scanned over a sample and images are generated by collecting the forward scattered electrons in a series of detectors. STEM is a very powerful technique capable of atomic-resolution imaging and analysis thanks to the combination of the electronics and mechanical stability of TEMs with the high-brightness electron sources. In particular, the Z-contrast high-angle annular dark-field (HAADF) technique is often used for atomic-scale imaging. Unlike HRTEM images, HAADF images are formed by electrons that are elastically scattered at high angles (50–150 mrad) which in turn are dependent on the atomic number of the atomic columns. It can be shown that there is no coherence relationship between high angle scattered electrons because they are mutually independent. Therefore, for incoherent scattering, the intensities from individual scatterers (atoms) are added, rather than the wave function amplitudes. The phase relationship of scattered beams and their interference, which are important considerations for HRTEM imaging, are not relevant for HAADF-STEM imaging. Each atom can be considered an independent scatterer because there is no constructive or destructive interference between the phases of wave functions emanating from the different atoms. The incoherent nature of Z-contrast STEM imaging enables a direct interpretation of these images in terms of atom types and positions.

The Z-contrast STEM images are formed by collecting high-angle elastically scattered electrons with an annular dark-field detector. The fact that the probability of such scattering

events rises for heavier atoms offers the possibility for obtaining chemical contrast. This means that areas or particles containing high Z elements scatter stronger and thus appear bright in images. This is in particular a valuable method for determining the size distribution of NCs embedded in nitride or oxide matrices. For example in the present work, Ge NCs of a few nm can be easily recognized by their bright contrast in SiO_2 matrix as shown in Paper III.

3.2 Electronic structure of semiconductor nanocrystals

3.2.1 Electron Energy Loss Spectrometer

When an electron beam is incident into a specimen, some of the electrons are inelastically scattered and lose a part of their energy. Elemental composition and atomic bonding states can be determined by analyzing the energy loss with the spectrometer attached in the electron microscope. This technique is called electron energy loss spectroscopy (EELS). The basic electron spectrometer type is the prism spectrometer. Electrons are deflected by about 90^o in a perpendicular static magnetic field. According to the Lorentz force, the deflection angle depends on the electron velocity. Using quadruple lenses the spectrometer can disperse electrons according to their energy loss and project them on a detector (CCD) which can record the spectrum obtained as shown in Fig. 3.4.

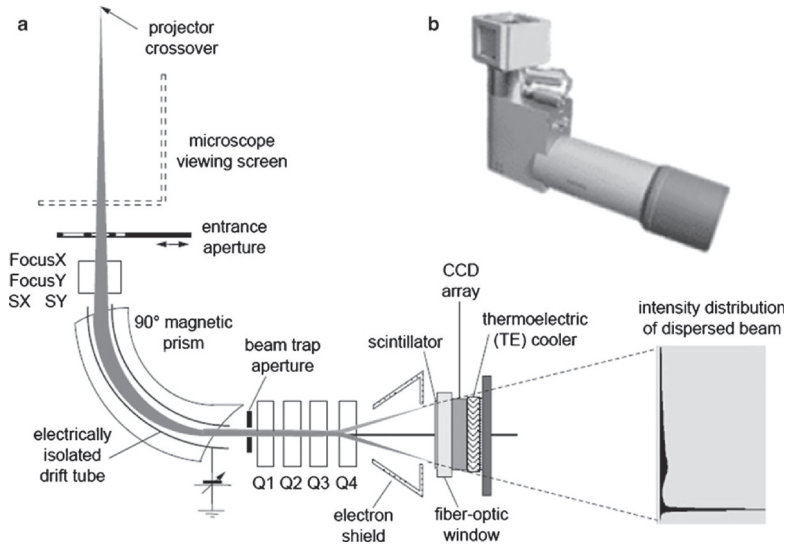

Figure 3.4 Gatan Enfina EELS spectrometer. The diagram in (a) shows schematically how the electrons are dispersed in the magnetic prism and then projected onto the CCD via the quadrupoles lenses of the spectrometer. (b) shows a picture of the Gatan Enfina. [81]

3.2.2 STEM-EELS experimental setup

Studying QC effects in semiconductor NCs has been done by using many different optical techniques. One of the important factors for the experimentalists to consider when studying QC effects is the spread in NC sizes in the experimental samples, which can lead to uncertainties in exciton line positions and widths. Due to the limit of spatial resolution, the optical techniques do not have enough sensitivity to probe the properties of individual particles. The observed results are therefore collectively quantitative informations, which are difficult to interpret. On the other hand, progress in electron microscopy has combined advantages of both high brightness electron sources, aberration corrected microscopes and EELS spectrometers to provide extremely high spatial and energy resolutions. This makes the aberration corrected STEM-EELS particularly suited to probing the local electronic structure and elemental distribution inside the individual NCs and their surrounding matrices. Therefore, in the present work STEM-EELS has been used as a main tool to study a number of phenomena related to QC in individual NCs embedded in dielectric matrices. The chemical states and electronic properties of the matrix, size and crystal structures of the NCs are also investigated and discussed. The STEM-EELS experiments were performed at 60 to 100 keV in a C_s-corrected Nion UltraSTEM equipped with a Gatan Enfina spectrometer (Fig. 3.5). Dropping the acceleration voltage down to 60 kV has the advantage of minimizing the retardation effects that would otherwise mask the fine details in the zero-loss peak (ZLP) tail and reducing the radiation damage [82]. The cold field electron emitter of this instrument has a native energy spread of 0.3 eV, as determined from the full width at half maximum (FWHM) of the ZLP in typical operating conditions. The EELS acquisitions were operated with a probe size of ~0.7 – 1.1 Å, depend on the applied voltage. The collection semi-angle was 4 mrad for the low-loss data sets and 32 mrad for the core-loss datasets. The probe convergence semi-angle was 30 mrad. Both 2D-EELS spectrum imaging and low-dose 'SMART EELS' line-scan techniques [83] were employed. The latter was used in order to mitigate the effects of radiation damage and contamination. Postmortem images were systematically acquired in order to check for possible specimen drift during the data collection and assess specimen beam damage. Under such experimental conditions, plasmon-loss and core-loss EELS spectra were acquired in order to probe the valence band and conduction band information respectively.

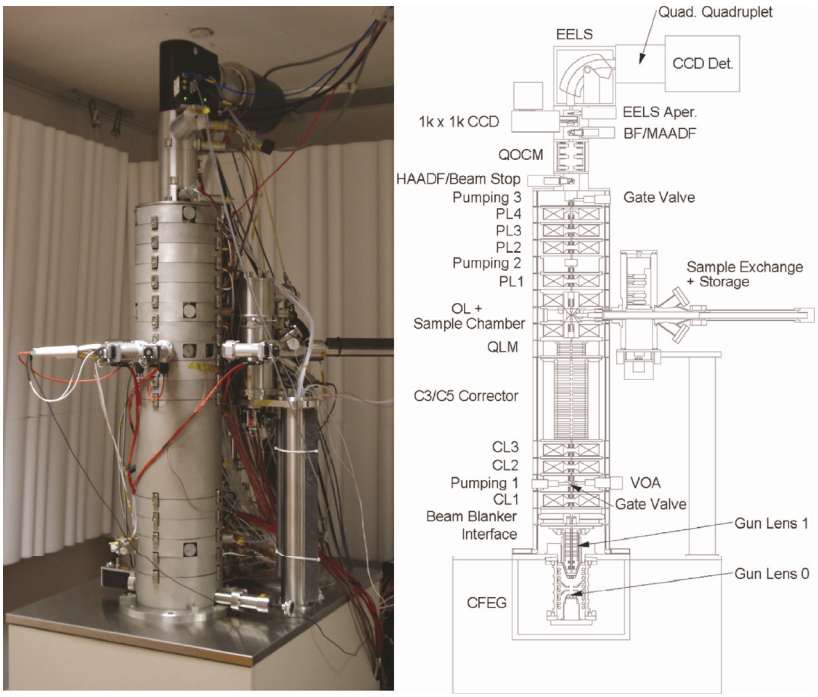

Figure 3.5 Photo and schematic diagram of the basic components of C_s-corrected SuperSTEM Nion Ultrastem™ 100.

3.2.3 Low-loss EELS

The low-loss region in the EELS spectra, extending from 0 to ~50 eV (Fig. 3.6), is dominated by the bulk plasmon excitation, which is a resonant oscillation of the valence electron gas of the solid in response to the fast incident electron. The plasmon energy is sensitive to the valence electron density; hence, any changes in this quantity, such as chemical modification or structural rearrangement, can be detected as a shift in the plasmon energy. This can be a very useful method to investigate the stoichiometry of a chemical compound, e.g. SiO_2 or Si_3N_4. Particularly, in a microstructure any change in material properties (such as structural and electronic changes) as a function of the local valence electron densities can be determined using plasmon energy as an indicator. It has been reported that changes in the band gap structure of the NCs arising from QC can be observed by shifts to higher energies (blue shift) of the volume plasmon energy with decreasing NC size [84, 85]. Furthermore, when the size of the NCs decreases, the effects of QC and interfaces are also reflected in the changes of plasmon loss energy and features: the volume plasmon energy is predicted to be proportional to the inverse square of the NC diameter; the plasmon peaks broaden with

decrease in the NC size due to the faster relaxation of the plasmon in the NCs than in the bulk materials [84-86].

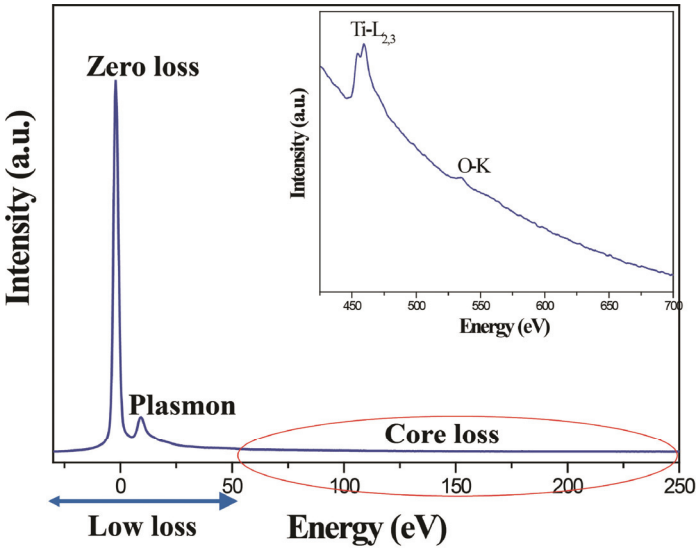

Fig. 3.6 An example of electron energy-loss spectrum (figure adapted from D.M. Kepaptsoglou, Electron Microscopy Course, 2011)

From a theoretical point of view, Mitome has introduced an analytical approximation for the increase of volume plasmon energy as a function of the NCs size through the oscillator strength [85]. The plasmon energy is proportional to the square root of the oscillator strength, which in turn is proportional to the energy gap of the NCs. This leads to the following expression:

$$E_P = \frac{\hbar^2 \pi^2 E_b}{\mu d^2 E_g} + E_b \qquad (6)$$

where $\hbar$ is the Planck constant, μ is the effective mass of an electron/hole pair in the material in the strong confinement regime ($1/\mu = 1/m_e + 1/m_h$, where m_e and m_h are the electron and the hole effective masses, respectively). In the medium confinement regime, μ can be replaced by m_e as mentioned in section 1.4. d is the particle diameter, E_p is the plasmon energy of the nanoparticle, E_b and E_g are the plasmon energy and the band gap for the bulk, respectively. This effective mass model predicts the relationship between the particle size and its plasmon energy $E_P \approx 1/d^2$. For the present work, this simple three-dimentional

confinement approximation adequately predicts the increase of plasmon energy when the NC size reaches a critical value in both the Si and Ge NCs cases. Small deviations from the theoretical prediction were found and suggested due to lattice distortion, change in crystal structure and dangling bonds at defect centers, or due to the interface effects between the NCs and the matrix. This is discussed in detail in Papers I and III.

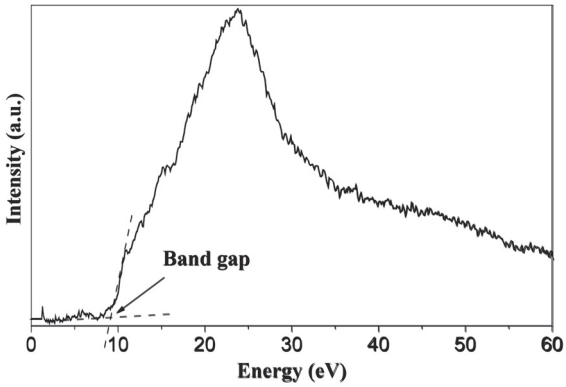

Fig. 3.7 Visible band gap signal of the stoichiometric SiO_2 estimated to be at 9.5 eV from the intersection of a straight line originating from the background level with a linear fit to the onset of the plasmon spectrum.

In addition to plasmon oscillations, the low loss region may also exhibit interband transitions, which are single electron transitions from the valence band to unoccupied states in the conduction band. In an insulator with a wide band gap there should be no interband transitions below the band gap energy and thus the band gap is associated with an initial rise in intensity in the low loss region. Figure 3.7 shows an example of the visible band gap signal of the stoichiometric SiO_2 in the present work estimated to be at 9.5 eV (from the intersection of a straight line originating from the background level with a linear fit to the onset of the low-loss signal spectrum). In the case of semiconductor nanostructures, one would expect the interband transitions to move to higher energies due to QC effects. The blue shift of these transition energies in Si and Ge NCs has been studied mostly by optical spectroscopies [87-90], but ambiguous results were obtained because the information they yield is difficult to interpret due to several factors contributing to the experimental results: size dispersion of NCs, different shapes, density and interface structures of NCs as well as electron, photon and phonon transfer between NCs. The local information obtained directly in individual NCs by STEM-EELS is somewhat simpler to understand and interpret. In the present work, the blue-

shift of the E_2 transition in Ge NCs, which occurs near the X point of the Brillouin zone, was clearly resolvable in the low loss region of EELS spectra. This is discussed in detail in Paper III.

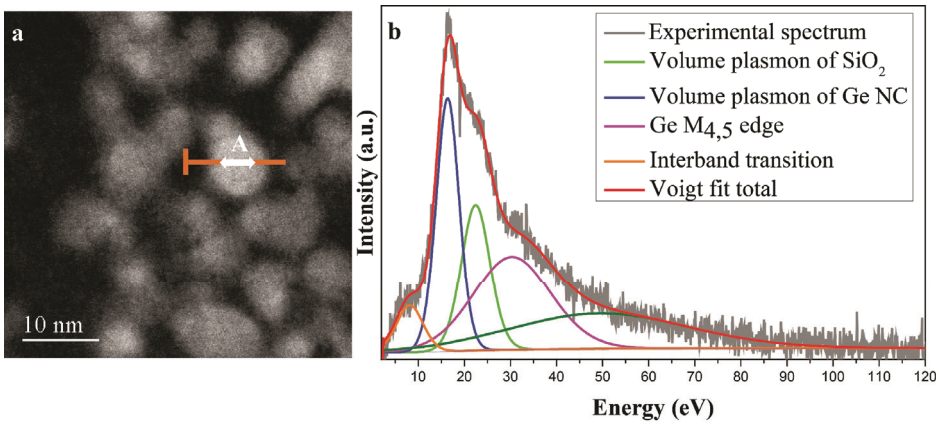

Fig. 3.8 (a) HAADF image is marked with the trace of the line scan taken across the Ge NC. (b) Deconvolution of the low-loss EELS spectrum acquired from the Ge NC core at the position A.

In order to obtain reliable results from the low loss EELS spectra of the semiconductor NCs embedded in an amorphous dielectric matrix, several steps should be carried out. Firstly, the absolute energy scale for the whole spectrum should be calibrated by means of zero loss peaks. Secondly, an accurate removal of the zero loss peak from the rest of the spectra using the power-law function need to be done to reveal the onset of the band gap signal and/or interband transition features. Thirdly, the very low-loss region of the EELS spectra where the interband transitions locate is complicated to analyze due to the convolution of many factors: retardation effects such as Cerenkov losses or losses due to the excitation of guided light modes, radiation loss effects, surface/interface plasmons. Therefore, calculations of low-loss EELS spectra for similar confined nanostructures have also been carried out to give a better physical understanding and interpretation. Last, owing to the delocalized character of the plasmon excitation, the sample volume contributing to the low-loss signal is significant. Therefore, the broadening of plasmon peaks of the NCs with small sizes is expected to contain some contribution from the vicinity of the surrounding matrix. The broad plasmon peaks in the low-loss EELS spectra need to be deconvoluted in different components using the Voigt functional form fitting method. Based on the observed features in the spectra and

the expected characteristic excitations, several component peaks can be used to fit the spectra: interband transitions, surface/interface plasmons, volume plasmon from both the NCs and the host matrix (Fig. 3.8). By combining the literature data and the experimental results in the present work, the NC size dependence of volume plasmon energy and interband transition were derived and compared to the theoretical models. Once the low loss data has been treated correctly, the results can be directly compared to other optical characterization techniques.

3.2.4 Core-loss EELS

The core-loss region in the EELS spectra, extending from ~50 to several thousand eV (Fig. 3.6), corresponds to the excitation of electrons from well-localized orbitals on a single atomic site to unoccupied electron energy levels just above the Fermi level of the material. This region exhibits ionization edges, of which threshold energy is determined by the binding energy of the particular electron subshell within an atom. Therefore, the atomic species can be identified from that. More importantly, if the conduction band minimum of the NCs shifts to higher energies by ΔE_{CB} due to QC effects in the NCs, the ionization edges in the core-loss EELS spectra are also expected to shift by ΔE_{CB} to higher energies, and are slightly broadened with respect to the bulk. Batson and Heath have reported the quantum behaviors of Si 2p → conduction band in EELS spectra acquired from single H-terminated Si NCs [91]. They found that the Si $L_{2,3}$ edge shape changes abruptly from multiple sets of parabolic bands (corresponding to final states at Δ_1, L_1 and L_3) to a single parabolic band and a blue shift of 2 eV for H-terminated Si NCs smaller than 5 nm. In agreement with this, a shift of 1.5 eV at the Si $L_{2,3}$ edge onset relative to the bulk when the Si NC size drops to 3 nm was found in the present work (Paper I), even though the change of edge features was not clearly resolved.

In the near edge region, the electron energy-loss near-edge structure (ELNES) reflects the electronic states in the empty conduction band of the material. These structures are highly dependent on the local atomic environment, which may be used to determine the density of unoccupied electron states projected onto the particular atom in question. In many cases, for a particular elemental ionization edge, the observed ELNES exhibits a structure that is specific to the atomic arrangement, i.e. the number of atoms and their geometry, as well as the type of atoms within solely the first coordination shell. Hence, they provide a means of qualitatively determining nearest neighbor coordination. For example, in the present work it is possible to

distinguish different solid structures of Si_3N_4, SiO_2 or Si_2ON_2 based on their distinct ELNES and transition peak energies. This is discussed in detail in Paper II.

The core loss edges lie on a background composed of the tails of the plasmon excitation plus those from ionization edges with lower threshold energies. This large background contribution is one of the major concerns since the weak edges become difficult to see and analyze, with the signal to noise ratio reducing with increasing specimen thickness. Therefore, the subtraction of the continuously decreasing background component from the edge signal of each element of interest needs to be done, by using the power law function method.

3.2.5 Thickness considerations

Thickness of the investigated specimen in TEM is important for several reasons. First, if the changes in the band structure are localized around the NCs, then in theory a sample that is thinner than those NCs is required. Having tens of nm of film above and below would indeed completely mask any signal intrinsic to the cluster itself. Second, the thicker the sample, the more likely it is to encounter retardation effects in the low loss region (guided light modes, Cerenkov etc...) and those essentially prohibit any quantitative band structure analysis from the low loss EELS data. Dropping the microscope voltage mitigates that effect to an extent (the lower the voltage, the less prominent the retardation effects are [82]) but the electrons penetrate the sample even less, which means a thin specimen is even more crucial.

According to Erni and Browning [82], in order to perform low-loss EELS experiments with minimal retardation losses, the ideal specimen thickness t needs to be in the range of $0.2\text{-}0.5t/\lambda$, where λ is the inelastic mean free path at the given acceleration voltage. For example in the case of the Ge-SiO_2 system that was observed at 60 kV, the electron mean free path for SiO_2 is approximately 58 nm. The specimen thicknesses in the most useful areas for this experiment were determined to be in the range of ~0.15 to $0.3t/\lambda$ by the log-ratio method from low-loss EELS spectra [92], which yields roughly 8 to 18 nm.

At such small thicknesses it is possible to determine accurately the contribution of the very small NCs (Si or Ge) to the observed plasmons in the low-loss EELS spectra, the signal of which would otherwise be swamped by the matrix signal (for more details see Paper I and III). For example in the case of the 8 nm Ge NC shown in Fig. 3.8, the total specimen thickness was determined to be 18 nm, which means that the NC represents 45 % of the total

thickness in the beam path. This is in good agreement with the relative area of the plasmon component attributed to the Ge NC in the low-loss EELS spectrum in Fig. 3.8 that was determined to be ~50%.

Similar to the low-loss EELS, small specimen thicknesses allows for the detection of the core-loss signal originating from the small NCs, while effects like multiple scattering that could complicate the EELS data processing and interpretation can be ignored. This is especially important in the case of the Si/Si_3N_4 system, where the features of the Si $L_{2,3}$ edge for the NCs and the silicon nitride matrix overlap. In this case the core-loss signal can be simply considered to be a linear combination of the signals originating from the matrix and the NC weighed by their respective thicknesses (or mass) in the electron beam path. Figure 3.9 shows an MLLS fitting of the Si $L_{2,3}$ core loss signal from the core of a Si NC of 3 nm in diameter, using the signals from the Si single crystal substrate (bulk Si reference) and the matrix adjacent to the NC (silicon nitride reference) as references, and the fitting coefficients of the two components. The onset of the Si $L_{2,3}$ of the bulk Si reference spectrum has been shifted in order to match that of the Si NC, as the latter shows a blue shift attributed to QC effects (for more details see Paper I).

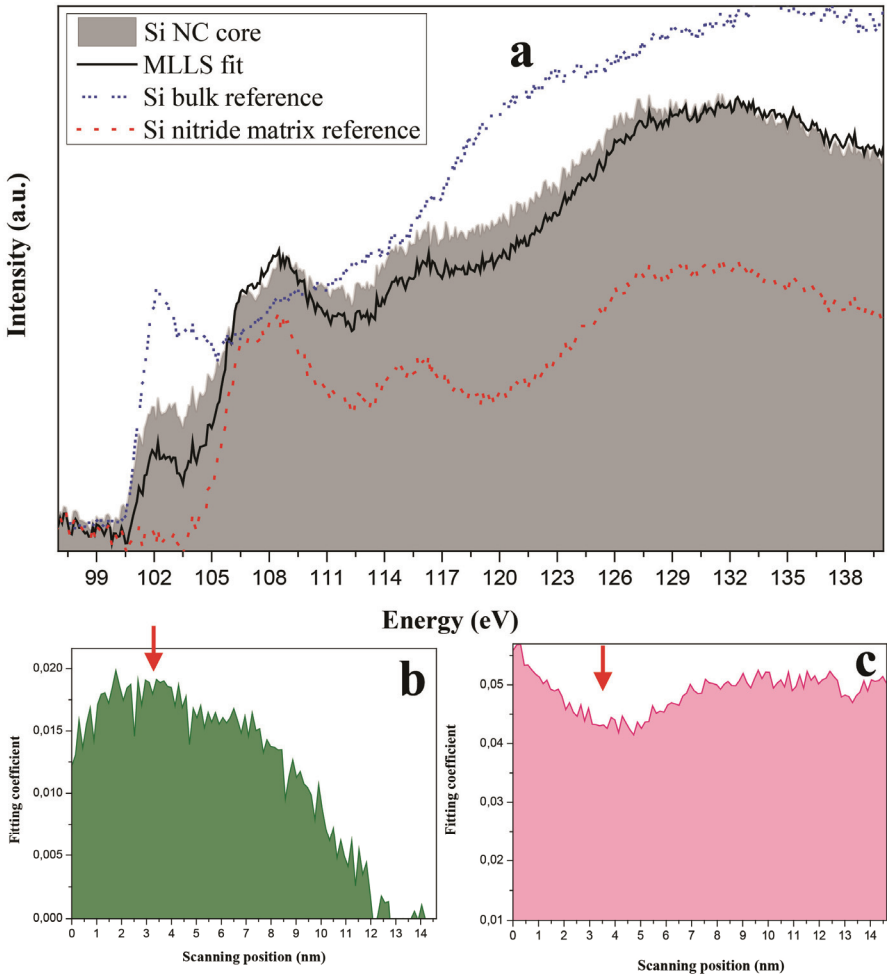

Fig. 3.9 (a) MLLS fitting (solid line) of the Si $L_{2,3}$ (background subtracted) edge acquired at a Si NC core (shaded curve). The MLLS fit is a linear combination of bulk Si (short dot line) and silicon nitride matrix (dot line). Fitting coefficient of (b) bulk Si and (c) silicon nitride matrix component were applied to the MLLS fitting. The arrows point out the position of the NC core, where the signal of Si increases and the matrix decreases.

3.3 TEM specimen preparation

As mentioned in the previous paragraph, specimen thickness is a crucial parameter in order to observe and quantify the QC effects arising from the embedded NCs. In order to achieve such

small and uniform thicknesses, a combination of several different thinning methods was applied:

- Cutting sample to make cross-section stacks: slices of 2 mm width and 4 mm length are cut out of the sample using a diamond scriber. Two slices of the sample are glued together by using the Gatan two-component epoxy glue so that the film layers face each other. Two other slices of a Si wafer with the same size are glued on top of each slice of the sample (with Si on top of the layers). The film layers of interest should be situated in the middle of the stack, so that they are in the center of the final cross-section TEM specimen. The glued stack is then heated to 120 ^{o}C, the hardening time is about 2 minutes.

- Mechanical grinding: The cross-section stack is then coarsely thinned by mechanical grinding using SiC abrasive papers, followed by mechanical fine grinding and polishing to flatten the surface of the stack to be shiny and scratch-free using the MultiPrep™ System. In order to reduce artifacts from ion beam damage, the specimen thickness is preferred to be mechanically thinned down to ~10 μm, followed by quick ion beam polishing for 15 – 30 minutes. At the final stage, the specimen is mounted on the support grid.

- Ion beam polishing: In the Gatan PIPS 691 Precision Ion Polishing System, the polished surfaces of a thin sample are bombarded with argon ions of energies of between 2 and 5 kV at various glancing angles. The ideal ion-milled TEM sample would contain large, thin areas in selected regions, minimal top and bottom surface amorphization, and minimal preferential etching of adjacent materials. Minimizing the incident angle of the ion beam to the surface of the sample has been found to be one of the most effective techniques for fulfilling these requirements. The best result is obtained with a low ion-incident angle such as 5-7 degree. Operation at low angles increased the thinning time and contamination from the Cu support grid. Therefore, the Ti grid has been used instead. Since Si is not a good heat conductor, long ion beam milling operation and Ar implantation might over heat and/or create defects in the sample, which could change the original nanostructures. Therefore, it is important to work with very thin samples and low ion-incident angles to obtain successful and artifact-free specimens.

3.4 Elemental composition and chemical states

X-ray Photoelectron Spectroscopy (XPS) is an analysis technique that uses X-rays in an ultra-high vacuum environment to investigate the elemental composition and chemical states of a solid material. Although this technique is commonly used for surface characterization, the use of sputtering and collecting data through the whole thin film depth in the present make it, to some extent, a bulk characterization method. XPS is based on the photoelectric effect of interactions between x-rays and electrons in the solid, resulting in electron emission from the solid surface. Depending on the energy of the applied X-rays, the electrons can be generated not only from the outer shells but also from the core levels of all elements. When an incident X-ray collides with a core electron, this causes the electron to be ejected from the electronic shell. The electron is released with a certain kinetic energy that is directly related to the binding energy of the electron to the atom. The ejection of the inner core electron leads to the secondary processes; the missing inner core electron represents an unstable hole in the electronic shell. An electron from the valance shell then fills the newly formed hole, causing an Auger electron to be emitted from the valance shell to conserve energy. Again, the kinetic energy of the emitted electron is directly related to the binding energy of the electron to the atom. These two processes are used to identify the elements in the sample since the binding energies of the electrons are unique for every element. To determine the binding energies, we first need to collect the kinetic energies of the electrons. Once the detector collects the data, we can calculate the binding energies of the electrons if we know the wavelength of the incident x-rays. In theory, this should be all that is needed to find the binding energy of the emitted electrons. However, depending on whether the sample is an insulator or a conductor, the binding energy will be changed slightly. This is due to the fact that the Fermi level of both the sample surface and the spectrometer are equivalent. Since all samples are grounded in the system the conducting sample will not have charge build up. An insulating sample is slightly different. For insulating samples, in general, the Fermi levels are not equivalent between the sample and the spectrometer. Charge build up occurs just above the sample's surface which causes the Fermi level of the spectrometer to shift to a higher energy. The shift in the Fermi level of the spectrometer results in the kinetic energy of the measured electrons to be slightly different from the actual value. To account for this during analysis, we calibrated the data using the Carbon 1s peak at a binding energy of 285 eV.

The XPS measurements in the present work were carried out using a Kratos AxisUltra^{DLD} instrument with a monochromatic Al Kα radiation. The employed settings allowed for a

resolution of 0.57 eV as determined by the FWHM of the Ag $3d_{5/2}$ peak. Depth profiling was performed using Ar ion sputtering (at 4 keV) combined with sample rotation. To analyze the XPS data, the CASA data processing program was used. The collected data is a measurement of binding energies, which can be found once the energy of the incident x-ray is known for the system. Since the binding energy is unique for every element, the elemental composition of the materials can be determined qualitatively. An important aspect of XPS is to determine the quantitative chemical composition of the sample, which can be derived from the photoelectron peak areas. The area under the photoelectron curve is proportional to the number of atoms that emit the electrons at that binding energy. Therefore, if we take the ratio of the area under the binding energy curve for each element, we can determine the composition of the samples quantitatively. Prior to the quantitative evaluation of the photoelectron peak areas, a suitable inelastic background subtraction needs to be done using Shirley background subtraction method. More importantly, the chemical states of the materials can also be found through a reasonable fitting of the experimental peaks. In order to obtain an optimized fit with sufficient number of Gaussian-Lorentzian curves without constraints, knowledge of the sample chemistry is important as it suggests the number of chemical states and therefore number of peaks. Introducing parameter constraints to restrict the peak widths and relative intensities of the peaks force the peak model to obey the chemistry. Without these inputs any model designed purely on the spectral envelope would be a cause for concern. In the case of SRN thin films in the present work, a depth profile study through the whole film depth has revealed important information including chemical composition and bonding structures of the nitride networks. The atomic percentage of each tetrahedral unit incorporated in the film network was calculated from the deconvolution of the XPS spectra in the Si $2p_{3/2}$ region and corroborated by the results obtained from survey scans. The chemical modification due to the substitution of N atoms by O in the Si_3N_4 network can lead to the shift of the binding energy in the Si $2p_{3/2}$ and the N 1*s* region of the XPS spectra. Combined with the theoretical models of different chemical bond distribution, an unambiguous picture of the atomic structure and bonding characteristics of SRN thin films was made. These results and conclusions are discussed in detail in Paper II.

3.5 Optical properties

If a photon has an energy greater than the band gap energy, it can be absorbed and thereby raise an electron from the valence band up to the conduction band; this will create an electron-hole pair in the material. In this photoexcitation process, the electron generally has

excess energy, which it loses before coming to rest at the lowest energy in the conduction band. At this point the electron eventually falls back down to the valence band to recombine with the hole there through the radiative recombination process. As it falls down, the energy it loses is converted back into a luminescent photon, which is emitted from the material. Thus, the energy of the emitted photon is a direct measure of the band gap energy, E_g. In addition, the radiative recombination can also take place at the interfaces or defect centers, which introduce the energy levels in the middle gap or band tails. These processes can alter the radiative transitions and convolute or dominate the observed spectra. The process of photon excitation followed by photon emission is called photoluminescence (PL). This experiment also introduces the widely used tool – PL spectroscopy, which is a contactless, nondestructive method to probe the electronic structure of materials through using a monochromatic source to excite electrons and measuring the intensity of light as a function of wavelength. The intensity and spectral content of the emitted PL is a direct measure of various important material properties, including:

- Band gap determination: the spectral distribution of PL from a semiconductor can be analyzed nondestructively to determine the electronic band gap. This provides a means to quantify the elemental composition of compound semiconductor.

- Impurity levels and defect detection: the PL spectrum at low sample temperatures often reveals spectral peaks associated with impurities contained within the host material. The high sensitivity of this technique provides the potential to identify extremely low concentrations of intentional and unintentional impurities that can strongly affect material quality and device performance.

- Recombination mechanisms: the quantity of PL emitted from a material is directly related to the relative amount of radiative and nonradiative recombination rates. Nonradiative rates are typically associated with impurities and thus, this technique can qualitatively monitor changes in material quality as a function of growth and processing conditions.

In the present work, the PL measurements were performed by excitation with a 325 nm line of a He-Cd laser at room temperature. Due to the convolution of many factors (radiative electron–hole recombination in Si NCs, radiative recombination at defect centers in the nitride network and at localized bonding states at Si NCs/nitride interfaces), the PL spectra need to be deconvoluted by a standard nonlinear least-squares fitting procedure using Voigt

functions in order to identify individual constituents. The deconvoluted PL spectra measured in the SRN thin films have revealed emission bands at different energies, corresponding to different radiative recombination centers in both Si NCs, defects and impurity levels. In association with other analytical techniques, PL measurements in the present work provide very useful information about electronic structures and the role of defects and impurities existing in the nitride films, which is vitally important parameters influencing solar cell device efficiency.

Chapter 4

Overview of publications

4.1 Paper I

The paper presents a study of QC in Si NCs. Based on the characterization of individual Si NCs using STEM-EELS, the volume plasmon energy and the Si $L_{2,3}$ edge position as a function of the Si NC size obtained with TEM observation is investigated. In both cases, the measured shifts in energy are consistent with the previous works and reflect QC effects. While similar results have been obtained for Si NCs, the novelty resides in the host matrix: the Si NCs are embedded in a silicon nitride film and such type of film has recently gained much interest to be integrated in Si solar cells. In addition, the role of defects to account for small variations in the shift of the volume plasmon energy is highlighted. The direct evidence of QC in this system confirms the viability of silicon nitride as a matrix for nano-structured thin films in tandem solar cell stacks and opens up promising avenues for the exploitation of the higherband gap energy of silicon nitride in PV applications.

The films were grown and the TEM work was carried out by P. D. Nguyen at the University of Oslo. The STEM-EELS experiments were performed in SuperSTEM Laboratory in UK by Dr. Q. M. Ramasse, P. D. Nguyen and Dr. D. M. Kepaptsoglou. Data analysis was carried out by P. D. Nguyen.

4.2 Paper II

The atomic structure and optical properties of SRN thin films have been for decades the subject of intense research. However, there is still an ongoing and vibrant discussion about the deviation between theoretical and experimental results. This is mainly because the results have been reported only partially and a broader, more complete picture is still lacking, which should take into account any effect of chemical modification, intrinsic and extrinsic defects on the physical properties of SRN films. The problem is that no single characterization technique can provide a clear and definitive structural picture of the SRN films. Hence,

complimentary techniques must be applied simultaneously in order to experimentally verify a clear correlation between structural and optical properties unambiguously. In this paper, different techniques including XPS, HRTEM, STEM-EELS and PL spectroscopy have been combined to study the structure, chemical bonding and optical properties of sputtered silicon nitride thin films of variable compositions. The theoretical models of chemical bond distribution were justified experimentally by the XPS and EELS results. A model of gap states and electronic transitions for the SiO_xN_y films is proposed, which explains adequately the role of QC excitons vs defects in the visible luminescence of SRN films with and without Si NCs.

The films were grown and the TEM work was carried out by P. D. Nguyen at the University of Oslo. The STEM-EELS experiments were performed in SuperSTEM Laboratory in UK by Dr. D. M. Kepaptsoglou and P. D. Nguyen. XPS measurements were done by M. F. Sunding and PL data have been obtained by L. O. Vestland. Data analysis was carried out by P. D. Nguyen.

4.3 Paper III

The paper reports on the QC of Ge NCs embedded in SiO_2 matrix through a blue-shift in plasmon energies and an enhancement of Ge interband transitions with decreasing NC size investigated by STEM-EELS. This technique allows direct correlation between the NC geometry and its electronic properties. While this is a natural extension of Paper I, the interesting results point out the important effects of the dielectric matrix surrounding the NCs. Because of that, a substantial deviation of the observed QC from the classical model was found. A comparison between the confinement strength in the system of Si NCs and Ge NCs was also brought into discussion.

The films were grown and the TEM work was carried out by P. D. Nguyen at the University of Oslo. The STEM-EELS experiments were performed in SuperSTEM Laboratory in UK by Dr. D. M. Kepaptsoglou. The low-loss EELS calculations were done by Dr. R. Erni. Data analysis was carried out by P. D. Nguyen.

4.4 Paper IV

Contamination in thin film samples during a sputtering process is a major concern since this will result in undesirable structures and properties. The purpose of the work was to identify the contaminations, which were present in the sputtered Si/Si_3N_4 multilayer thin films and find a solution for eliminating the contaminations. As the contamination resulted in crystallization of $CrSi_2$, which is considered as a promising material for thermoelectric application and for optoelectronic devices, the structures and mechanisms of $CrSi_2$ heterogen nucleation and growth during the sputtering and thermal annealing processes has been investigated further.

The films were grown and the TEM work was carried out by P. D. Nguyen at the University of Oslo. XPS measurements were done by M. F. Sunding. Data analysis was carried out by Prof. A. Olsen, P. D. Nguyen and Prof. A. E. Gunnæs.

Bibliography

[1] E. P. I. Association, *Global Market Outlook for Photovoltaics until 2016*, (May 2012).

[2] M. A. Green, *Third Generation Photovoltaics: Advanced Solar Energy Conversion* (Springer-Verlag, 2003).

[3] M. A. Green, Progress in Photovoltaics: Research and Applications 9, 123 (2001).

[4] W. Shockley and H. J. Queisser, J. Appl. Phys. 32, 510 (1961).

[5] C. Bulutay and S. Ossicini, in *Silicon Nanocrystals* (Wiley-VCH Verlag GmbH & Co. KGaA, 2010), p. 5.

[6] M. C. Beard, K. P. Knutsen, P. Yu, J. M. Luther, Q. Song, W. K. Metzger, R. J. Ellingson, and A. J. Nozik, Nano Lett. 7, 2506 (2007).

[7] G. Conibeer, in *Silicon Nanocrystals* (Wiley-VCH Verlag GmbH & Co. KGaA, 2010), p. 555.

[8] G. Conibeer, et al., Thin Solid Films 516, 6748 (2008).

[9] A. D. Yoffe, Advances in Physics 42, 173 (1993).

[10] T. T. Y.Masumoto, *Semiconductor Quantum Dots: Physics, Spectroscopy and Applications* (Springer, 2002).

[11] M. Zacharias, in *Silicon Nanocrystals* (Wiley-VCH Verlag GmbH & Co. KGaA, 2010), p. 195.

[12] K. Raghavachari and V. Logovinsky, Phys. Rev. Lett. 55, 2853 (1985).

[13] J. R. Chelikowsky, Phys. Rev. Lett. 60, 2669 (1988).

[14] Z. Zhou, L. Brus, and R. Friesner, Nano Lett. 3, 163 (2003).

[15] M. V. Wolkin, J. Jorne, P. M. Fauchet, G. Allan, and C. Delerue, Phys. Rev. Lett. 82, 197 (1999).

[16] L. Pavesi and R. Turan, in *Silicon Nanocrystals* (Wiley-VCH Berlin, 2010), p. 1.

[17] L. T. Canham, Appl. Phys. Lett. 57, 1046 (1990).

[18] N. Luca Dal, H. Sebastien, Z. Natalia, Y. Jae Hyung, W. Andrew, S. Michael, M. Jurgen, G. Giulia, and C. K. Lionel, Selected Topics in Quantum Electronics, IEEE Journal of 12, 1151 (2006).

[19] S. Minissale, S. Yerci, and L. D. Negro, Appl. Phys. Lett. 100, 021109 (2012).

[20] G. Conibeer, I. Perez-Wurfl, X. Hao, D. Di, and D. Lin, Nanoscale Research Letters 7, 193 (2012).

[21] F. Herman, R. L. Kortum, and C. D. Kuglin, Int. J. Quantum Chem 1, 533 (1967).

[22] Y. Maeda, Phys. Rev. B 51, 1658 (1995).

[23] T. Takagahara and K. Takeda, Phys. Rev. B 46, 15578 (1992).

[24] T. Takagahara and K. Takeda, Phys. Rev. B 53, R4205 (1996).

[25] C. Bostedt, T. v. Buuren, T. M. Willey, N. Franco, L. J. Terminello, C. Heske, and T. Moller, Appl. Phys. Lett. 84, 4056 (2004).

[26] Y. M. Niquet, G. Allan, C. Delerue, and M. Lannoo, Appl. Phys. Lett. 77, 1182 (2000).

[27] F. A. Reboredo and A. Zunger, Phys. Rev. B 62, R2275 (2000).

[28] T.-W. Kim, C.-H. Cho, B.-H. Kim, and S.-J. Park, Appl. Phys. Lett. 88, 123102 (2006).

[29] T.-Y. Kim, N.-M. Park, K.-H. Kim, G. Y. Sung, Y.-W. Ok, T.-Y. Seong, and C.-J. Choi, Appl. Phys. Lett. 85, 5355 (2004).

[30] Y.-H. Cho, Cho, E.-C., Huang, Y., Jiang, C.-W., Conibeer, G., and Green, M.A., in *20th European Photovoltaic Solar Energy Conference*, Barcelona, Spain, 2005), p. 47.

[31] Y. Kanemitsu, J. Lumin. 70, 333 (1996).

[32] H. Takagi, H. Ogawa, Y. Yamazaki, A. Ishizaki, and T. Nakagiri, Appl. Phys. Lett. 56, 2379 (1990).

[33] S. Takeoka, M. Fujii, and S. Hayashi, Phys. Rev. B 62, 16820 (2000).

[34] E.-C. Cho, University of New South Wales, Sydney, 2003.

[35] D. König, J. Rudd, M. A. Green, and G. Conibeer, Phys. Rev. B 78, 035339 (2008).

[36] B.-H. Kim, C.-H. Cho, T.-W. Kim, N.-M. Park, G. Y. Sung, and S.-J. Park, Appl. Phys. Lett. 86, 091908 (2005).

[37] M. Wang, D. Li, Z. Yuan, D. Yang, and D. Que, Appl. Phys. Lett. 90, 131903 (2007).

[38] R. Guerra, M. Ippolito, S. Meloni, and S. Ossicini, Appl. Phys. Lett. 100, 181905 (2012).

[39] Y. Maeda, N. Tsukamoto, Y. Yazawa, Y. Kanemitsu, and Y. Masumoto, Appl. Phys. Lett. 59, 3168 (1991).

[40] M. Y. R. Hayashi, K.Tsunetomo, K. Kohno, Y. Osaka and H. Nasu, Jpn. J. Appl. Phys. 29, 756 (1990).

[41] C. Delerue, G. Allan, and M. Lannoo, Phys. Rev. B 48, 11024 (1993).

[42] G. Allan, C. Delerue, and M. Lannoo, Phys. Rev. Lett. 76, 2961 (1996).

[43] J. Nelson, *The Physics of Solar Cells* (Imperial College Press, London 2003).

[44] J. Kistner, X. Chen, Y. Weng, H. P. Strunk, M. B. Schubert, and J. H. Werner, J. Appl. Phys. 110, 023520 (2011).

[45] C. Ance, F. d. Chelle, J. P. Ferraton, G. Leveque, P. Ordejon, and F. Yndurain, Appl. Phys. Lett. 60, 1399 (1992).

[46] W.-S. Liao, C.-H. Lin, and S.-C. Lee, Appl. Phys. Lett. 65, 2229 (1994).

[47] R. Huang, K. Chen, B. Qian, S. Chen, W. Li, J. Xu, Z. Ma, and X. Huang, Appl. Phys. Lett. 89, 221120 (2006).

[48] Y. Liu, Y. Zhou, W. Shi, L. Zhao, B. Sun, and T. Ye, Mater. Lett. 58, 2397 (2004).

[49] L. D. Negro, J. H. Yi, L. C. Kimerling, S. Hamel, A. Williamson, and G. Galli, Appl. Phys. Lett. 88, 183103 (2006).

[50] M. Molinari, H. Rinnert, and M. Vergnat, Appl. Phys. Lett. 79, 2172 (2001).

[51] M. Molinari, H. Rinnert, and M. Vergnat, J. Appl. Phys. 101, 123532 (2007).

[52] X. J. Hao, A. P. Podhorodecki, Y. S. Shen, G. Zatryb, J. Misiewicz, and M. A. Green, Nanotechnology 20, 485703 (2009).

[53] A. K. PANCHAL, D. K. RAI, M. MATHEW, and C. S. SOLANKI, Nano 04, 265 (2009).

[54] R. Brydson, *Electron Energy Loss Spectroscopy*, Taylor & Francis, 2001).

[55] V. A. Gritsenko, H. Wong, J. B. Xu, R. M. Kwok, I. P. Petrenko, B. A. Zaitsev, Y. N. Morokov, and Y. N. Novikov, J. Appl. Phys. 86, 3234 (1999).

[56] P. E. Batson, Phys. Rev. Lett. 83, 4409 (1999).

[57] M. Fujii, O. Mamezaki, S. Hayashi, and K. Yamamoto, J. Appl. Phys. 83, 1507 (1998).

[58] S. K. Ray and K. Das, Opt. Mater. 27, 948 (2005).

[59] I. Stavarache, A.-M. Lepadatu, A. Maraloiu, V. Teodorescu, and M. Ciurea, J. Nanopart. Res. 14, 1 (2012).

[60] B. Zhang, S. Shrestha, M. A. Green, and G. Conibeer, Appl. Phys. Lett. 96, 261901 (2010).

[61] W. K. Choi, H. G. Chew, F. Zheng, W. K. Chim, Y. L. Foo, and E. A. Fitzgerald, Appl. Phys. Lett. 89, 113126 (2006).

[62] A. V. Kolobov, S. Q. Wei, W. S. Yan, H. Oyanagi, Y. Maeda, and K. Tanaka, Phys. Rev. B 67, 195314 (2003).

[63] V. Craciun, C. Boulmer-Leborgne, E. J. Nicholls, and I. W. Boyd, Appl. Phys. Lett. 69, 1506 (1996).

[64] K. Gacem, A. E. Hdiy, M. Troyon, I. Berbezier, P. D. Szkutnik, A. Karmous, and A. Ronda, J. Appl. Phys. 102, 093704 (2007).

[65] A. Kanjilal, et al., Appl. Phys. Lett. 82, 1212 (2003).

[66] S. N. M. Mestanza, E. Rodriguez, and N. C. Frateschi, Nanotechnology 17, 4548 (2006).

[67] R. Peibst, J. S. de Sousa, and K. R. Hofmann, Phys. Rev. B 82, 195415 (2010).

[68] N. Jiang, J. Qiu, A. L. Gaeta, and J. Silcox, Appl. Phys. Lett. 80, 2005 (2002).

[69] P. Basa, et al., Journal of Nanoscience and Nanotechnology 8, 818 (2008).

[70] J. K. Shen, X. L. Wu, C. Tan, R. K. Yuan, and X. M. Bao, Phys. Lett. A 300, 307 (2002).

[71] S. Cosentino, S. Mirabella, M. Miritello, G. Nicotra, R. Lo Savio, F. Simone, C. Spinella, and A. Terrasi, Nanoscale Research Letters 6, 135 (2011).

[72] A. G. R. Sara RC Pinto, Maja Buljan, Adil Chahboun Sigrid Bernstorff, Nuno P Barradas, Eduardo Alves, Reza J Kashtiban, Ursel Bangert and Maria JM Gomes, Nanoscale Research Letters 6, 341 (2011).

[73] N. Jiang, J. Qiu, and J. C. H. Spence, Appl. Phys. Lett. 86, 143112 (2005).

[74] W. K. Choi, V. Ho, V. Ng, Y. W. Ho, S. P. Ng, and W. K. Chim, Appl. Phys. Lett. 86, 143114 (2005).

[75] E. S. Marstein, A. E. Gunnæs, U. Serincan, S. Jørgensen, A. Olsen, R. Turan, and T. G. Finstad, Nuclear Instruments and Methods in Physics Research Section B: Beam Interactions with Materials and Atoms 207, 424 (2003).

[76] F. Delachat, M. Carrada, G. Ferblantier, J.-J. Grob, and A. Slaoui, Nanotechnology 20, 415608 (2009).

[77] Y. Q. Wang, R. Smirani, and G. G. Ross, Nano Lett. 4, 2041 (2004).

[78] Y. Q. Wang, R. Smirani, G. G. Ross, and F. Schiettekatte, Phys. Rev. B 71, 161310 (2005).

[79] Y. Q. Wang, R. Smirani, F. Schiettekatte, and G. G. Ross, Chem. Phys. Lett. 409, 129 (2005).

[80] D. J. Smith, in *Nanocharacterisation* (The Royal Society of Chemistry, 2007), p. 1.

[81] A. Maigné and R. D. Twesten, J. Electron Microsc. 58, 99 (2009).

[82] R. Erni and N. D. Browning, Ultramicroscopy 108, 84 (2008).

[83] K. Sader, B. Schaffer, G. Vaughan, R. Brydson, A. Brown, and A. Bleloch, Ultramicroscopy 110, 998 (2010).

[84] Y. W. Wang, J. S. Kim, G. H. Kim, and K. S. Kim, Appl. Phys. Lett. 88, 143106 (2006).

[85] M. Mitome, Y. Yamazaki, H. Takagi, and T. Nakagiri, J. Appl. Phys. 72, 812 (1992).

[86] P. N. H. Nakashima, T. Tsuzuki, and A. W. S. Johnson, J. Appl. Phys. 85, 1556 (1999).

[87] P. Tognini, L. C. Andreani, M. Geddo, A. Stella, P. Cheyssac, R. Kofman, and A. Migliori, Phys. Rev. B 53, 6992 (1996).

[88] J. R. Heath, J. J. Shiang, and A. P. Alivisatos, The Journal of Chemical Physics 101, 1607 (1994).

[89] B. S. Mendoza, J. Wei, and M. C. Downer, physica status solidi (b) 249, 1166 (2012).

[90] K. L. Teo, S. H. Kwok, P. Y. Yu, and S. Guha, Phys. Rev. B 62, 1584 (2000).

[91] P. E. Batson and J. R. Heath, Phys. Rev. Lett. 71, 911 (1993).

[92] R. F. Egerton, *Electron Energy-Loss Spectroscopy in the Electron Microscope* (Springer, New York, 2011).

Paper I

P. D. Nguyen, D. M. Kepaptsoglou, Q. M. Ramasse and A. Olsen

Direct observation of quantum confinement of Si nanocrystals in Si-rich nitrides

Physical Review B 85, 085315 (2012)

Direct observation of quantum confinement of Si nanocrystals in Si-rich nitrides

P. D. Nguyen,[1,*] D. M. Kepaptsoglou,[1,2] Q. M. Ramasse,[2] and A. Olsen[1]
[1]*Department of Physics, University of Oslo, P.O. Box 1048, Blindern, NO-0316 Oslo, Norway*
[2]*SuperSTEM Laboratory, STFC Daresbury Campus, WA4 4AD Warrington, Cheshire, United Kingdom*
(Received 6 December 2011; published 29 February 2012)

The band gap of the active layers in stacked Si-based tandem solar cells can be fine tuned by changing the size of embedded silicon nanocrystals (Si NCs). Although SiO_2 matrices have been predominantly used for such applications, nitride phases have recently emerged as a promising alternative. In this paper, we use high-resolution scanning transmission electron microscopy and energy-loss spectroscopy to report on the electronic structure of individual Si NCs embedded in silicon nitride films. Si NCs were produced by rf sputtering and exhibited controllable crystallite size and quality via different thermal annealing conditions. Quantum confinement effects were observed through a blue shift in both conduction band edges and volume plasmon energies as a function of particle size and structure. We show that, in good agreement with theoretical models, the volume plasmon energy E_p (eV) is related to the size d (nm) of Si NCs by $E_p = 16.89 + 23.90/d^2$. Lattice distortion in twinned Si NCs and dangling bonds at defect centers are shown to be the cause of a weakening in quantum size effects and a reduction in the light emission efficiency of the films. Both electron spectroscopy and optical results are consistent in explaining the correlation between structure and optoelectronic properties of Si NCs.

DOI: 10.1103/PhysRevB.85.085315 PACS number(s): 73.22.−f, 73.21.La, 73.63.Bd

I. INTRODUCTION

Over the last 10 years, the use of silicon-based tandem solar cells has emerged as a very promising technique to increase the efficiency of converting sunlight to electricity.[1] The structure of such devices involves stacks of Si-based materials with different band gap energies, which can absorb various solar spectrum bands. Carrier confinement in embedded nanoscale structures is the key to controlling the band gap of these layers. The integration of Si nanocrystals (Si NCs) with a size approaching the Bohr radius of a Si dielectric matrix allows for tuning of the band gap of the resulting material by utilizing the quantum effects related to the particle size and distribution across the solar cell.[2] The resulting quantum confined energy levels lead to an increase in the effective band gap of the nanostructure compared to bulk Si.

Extensive efforts have been made to produce the adequate structure of Si NCs embedded in a silicon oxide matrix for this type of application.[3–5] However, theoretical and experimental results recently suggested that, if silicon nitride is used as a matrix material around Si NCs, the photoluminescence peaks from the Si NCs are more blue shifted than those of similar NCs embedded in silicon oxide.[6] This enhanced energy of Si NCs in silicon nitride is attributed to the better passivation of the NCs by nitrogen atoms eliminating the strain at the Si-Si nitride interface.[6] In addition, Si_3N_4 has a lower band gap energy than SiO_2, leading to a lower barrier height and much increased carrier tunneling probability between Si NCs.[2] Therefore, Si NCs in a silicon nitride matrix are expected to be good candidates for silicon-based tandem solar cells. This nanostructure is typically formed by precipitation of Si from supersaturated silicon nitrogen solid solutions (Si-rich silicon nitride films, SRN), upon annealing at temperatures above 900 °C. Optical absorption spectroscopy and photoluminescence (PL) spectroscopy techniques have been extensively used to study the optoelectronic properties with respect to the size and structure of Si NCs embedded in silicon nitride matrix.[6–8] In spite of the fact that there have been plenty of reports on the quantum confinement-induced luminescence in this system, the origin of PL from SRN films is still an object of controversy.[9] Both the quantum confinement effects of Si NCs and defect centers, as well as the interface states in the SRN films, have been confirmed by PL measurements to give rise to the luminescence at different energy bands.[10] Although the optical techniques mentioned above have a very good energy resolution, the information they yield is averaged over a relatively large area of the specimen, which includes a large number and size distribution of NCs. Consequently, it is difficult to experimentally distinguish these mechanisms in the radiative emission. On the other hand, the very high spatial and energy resolution of dedicated aberration corrected scanning transmission electron microscopes equipped with an electron energy-loss spectrometer (STEM-EELS) provides information on the local electronic structure and elemental distribution inside the individual particles and their surrounding matrix.[11,12] To our knowledge, there has so far not been any high-spatial resolution STEM-EELS study of the quantum confinement and defect-related properties of Si NCs formed in a silicon nitride matrix.

In an attempt to explain the nanoscale origin of the PL from an electron spectroscopic point of view, we focus on using STEM-EELS to establish possible correlations between the quantum confinement of Si NCs in SRN and their size or localized defects. The size, density, and structure of Si NCs were controlled by varying the thermal annealing conditions. Changes in the band gap structure of the NCs arising from quantum confinement can be observed by shifts to higher energies (blue shift) of the volume plasmon energy or core loss edge onsets with decreasing NC size.[13,14] The relationship between structures/sizes of Si NCs and shifts in the plasmon energies and the Si $L_{2,3}$ edges will be discussed. In addition, PL suggests a strong influence of defects in Si NCs, which can act as nonradiative recombination centers and degrade the light emission efficiency. High-resolution transmission electron microscopy (HRTEM)/STEM observations, EELS,

and PL results are consistent in explaining the correlation between the structure and optoelectronic properties of Si NCs.

II. EXPERIMENT

Thin films composed of a nominally stoichiometric silicon nitride (Si_3N_4) buffer layer (∼15 nm) followed by an SRN layer (∼40 nm) were deposited on (100)-oriented single-crystal Si substrates by rf magnetron sputtering in an Ar atmosphere. The Si substrate was cleaned using a standard RCA (Radio Corporation of America) clean and given a dip in a 10% HF solution to remove the native oxide, and then dried by being blown with N_2 and put into the deposition chamber. Prior to sputtering, the chamber was evacuated to 5×10^{-7} mbar. *In-situ* Ar presputtering of the target was performed in order to remove any Si oxide on the target surface. The flow rate of Ar was maintained at a constant rate of 40 sccm during the film deposition. The excess silicon content in the SRN layer was achieved by cosputtering deposition from Si and Si_3N_4 targets at room temperature. The as-deposited layers were confirmed to be amorphous by transmission electron microscopy (TEM) imaging and electron diffraction. In order to form Si NCs in the nitride matrix, the samples were annealed in vacuum at temperatures of 900 to 1100 °C for 30 min to 2 h, depending on the specific desired nanostructure (i.e. the size and distribution of the particles within the matrix). In this paper, we report on three sets of samples that have been annealed at 1000 °C for 2 h, 1100 °C for 30 min, and 1100 °C for 2 h, hereafter denoted 1000-2 h, 1100-30 m, and 1100-2 h, respectively.

Transmission electron microscopy specimens were prepared for cross-sectional observation by mechanical polishing using the Allied MultiPrep System and finished with low-angle, Ar-ion milling at 5 keV in a Gatan PIPS 691 Precision Ion Polishing System. High-resolution transmission electron microscopy and energy-filtered transmission electron microscopy (EFTEM) observations were performed at 200 kV, with a JEOL 2010F microscope equipped with a Gatan Imaging Filter. The energy spread was determined to be ∼1.4 eV from the full width at half maximum (FWHM) of the zero-loss peak. Energy-filtered transmission electron microscopy images were acquired using the silicon bulk plasmon peak at 17 eV with an energy-slit width of 2 eV.

The STEM-EELS experiments were performed at 100 kV in a Cs-corrected Nion UltraSTEM[15] equipped with a Gatan Enfina Spectrometer. The cold field emission gun (FEG) has a native energy spread of 0.3 eV, as determined from the FWHM of the zero-loss peak in typical operating conditions. For the EELS acquisition, the collection semi-angle was 4 mrad for the low-loss datasets and 32 mrad for the core-loss datasets, and the probe convergence semi-angle was 30 mrad. In order to mitigate the effects of radiation damage and contamination on the beam-sensitive silicon nitride samples, the low-dose SMART[16] acquisition for EELS technique was employed. Postmortem images were systematically acquired in order to check for possible specimen drift during the data collection and assess specimen beam damage. Sample thicknesses in the most useful areas were determined to be 0.1 to 0.3 relative to the inelastic mean free path (t/λ) by the log-ratio method from low-loss EELS spectra. Occasionally, slightly thicker areas (up to $0.5t/\lambda$) were used when necessary in order to provide a better range of particle sizes. Due to the very low probability of plural scattering in such small thicknesses, the spectra were not treated for plural scattering removal.

III. RESULTS AND DISCUSSION

Figures 1(a) and 1(b) show, respectively, an HRTEM image and an Si plasmon EFTEM image acquired at 17 eV of the 1100-30 m sample. The observed lattice fringes in the SRN layer and electron diffraction pattern confirm the precipitation of NCs in the silicon nitride matrix. No crystallization was observed for samples annealed below 1000 °C. The EFTEM imaging at the bulk Si plasmon energy confirms that the observed NCs are indeed Si particles. The brighter areas correspond to the Si clusters and the Si substrate, while the

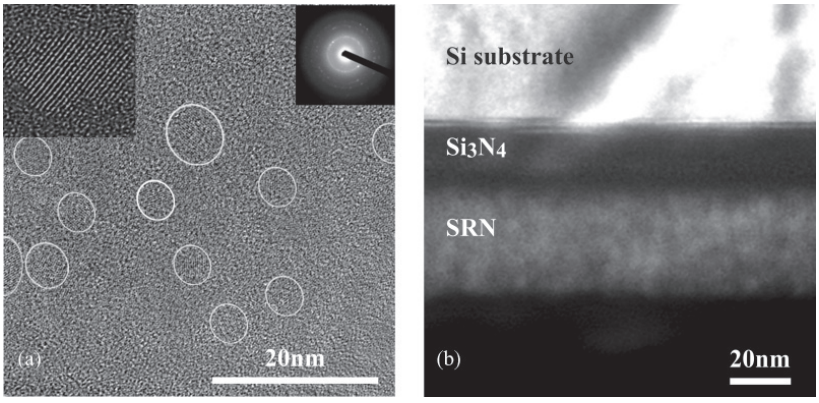

FIG. 1. (a) Cross-sectional HRTEM and (b) EFTEM at 17 eV images of Si NCs in nitride annealed at 1100 °C for 30 min. (a) shows distribution of NCs in which lattice planes can be seen clearly (left inset). Diffraction pattern (right inset) confirms crystal structure of Si particles observed by HRTEM. (b) shows layers of the film where bright areas correspond to elemental Si.

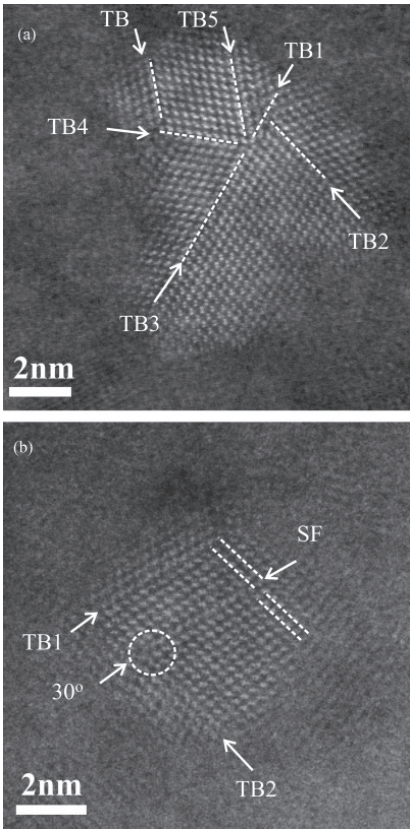

FIG. 2. (a) A HAADF STEM image of an Si NC with multiple twins and (b) a Si NC with twins, dislocation, and stacking fault in the film annealed at 1000 °C for 2 h. The arrows point out positions of twin boundaries (TB), stacking fault (SF), and a 30° partial dislocation with an extra plan marked by the dotted circle.

Si_3N_4 layer that has higher plasmon energy (∼24 eV) is dark. Delachat *et al*.[17,18] also used EFTEM imaging to identify Si NCs in a silicon nitride matrix confined between SiO_2 buffer layers and suggested that, because of the high density of NCs in their system, the phase separation mechanism probably consisted in nucleation and growth of Si NCs up to a critical size beyond which coalescence would take over. In the films grown for this study, both HRTEM and EFTEM micrographs also show that, in all samples, the amorphous SiN_x matrix contains a high density of Si NCs. However, the sizes and morphology of the Si NCs in our samples range from 1 to 30 nm and were controlled by varying the annealing temperature and/or time. The statistical analysis of the crystal size distribution obtained from the HRTEM micrographs indicates that the mean diameter and the width of the size distribution strongly depend on the annealing conditions. For instance, the mean size and the standard deviation (σ) increase with increasing the annealing temperature for the same annealing time and with increasing the annealing time for a fixed annealing temperature. Indeed, a mean size of ∼15 nm (with σ of approximately 4 nm) was observed in the 1100-2 h; the 1100-30 m and 1000-2 h exhibit finer grains, with a mean size of ∼3 nm ($\sigma \sim 0.8$ nm) and ∼4 nm ($\sigma \sim 1.7$ nm), respectively. While the mean sizes of Si NCs in 1100-30 m and 1000-2 h samples are comparable, in the latter, the largest particles (>5 nm) are characterized by heavy twinning (Fig. 2).

The high-angle annular dark field (HAADF) STEM image in Fig. 2(a) shows the typical morphology of twinned Si NCs observed in the 1000-2 h. We have found three- and fivefold twinned particles, with diameters as fine as about 5 nm, including twinned domains parallel to the [110] direction. Such a twinned structure has been observed before in Si NCs implanted in SiO_2 film by Wang *et al*.[19] and in silicon nitride by Delachat *et al*.,[17,18] although in the latter, the presence of these defects was not clearly linked to the NCs luminescence properties. For Si or diamond, fivefold twins with a mismatch angle of $360^\circ - (70.53^\circ \times 5) = 7.35^\circ$ can be accommodated by lattice distortions or other lattice defects.[19,20] In the present work, a similar misfit was observed in Si fivefold twins; dislocations and stacking faults were also found in some NCs [Fig. 2(b)]. This indicates the presence of lattice distortion and, therefore, of electronic structure changes through dangling bonds inside these Si NCs.[21] By contrast, there is no evidence of the presence of twin defects in the Si NCs with diameters <5 nm or >20 nm (not shown), which is typically the case of the 1100-30 m and 1100-2 h samples.

The chemical state of Si particles and their surrounding matrix was investigated by core-loss EELS line scans. Figure 3(a) shows the HAADF STEM survey image of a particle in the 1000-2 h sample, where the (004) Si dumbbells are clearly resolved (probe size 0.8 Å). The HAADF image is marked with the trace of the core-loss EELS line scan taken across the particle; on average, about 70–100 spectra were acquired during each core-loss line scan. Figure 3(c) shows background-subtracted, averaged Si $L_{2,3}$ EELS spectra (each spectrum in this figure is an average of 10 adjacent spectra) from the line spectrum image in Fig. 3(b). The spectra correspond to the areas marked A to E in Figs. 3(a) and 3(b), respectively. Spectrum C in Fig. 3(c) is taken from the particle core and corresponds to the crystalline Si $L_{2,3}$ edge with a sharp onset at 99 eV and a small peak in the fine structure at 101 eV, confirming that the composition of the precipitated NC is pure Si. In the spectra from areas A and E that correspond to the SRN matrix, the Si $L_{2,3}$ edge onset remains at 99 eV as a shoulder, while a pronounced peak corresponds to Si_3N_4 present in the fine structure at 105.5 eV [marked as a vertical dotted line in Fig. 3(c)]. A similar trend has been observed in the 1100-30 m and 1100-2 h. The presence of the shoulder at 99 eV corresponding to pure Si indicates that there is a contribution from the underlying or surrounding Si particles. Given the high density of Si NCs, as shown by the HRTEM/EFTEM observation, this is a likely scenario. Spectra B and D, taken at the matrix-NC interface, resemble those in areas A and E, with a more pronounced Si shoulder at 99 eV and a broader Si_3N_4 peak in the fine structure. This reveals that the relative contribution of the pure Si edge gradually increases toward the particle core as the Si content rises.

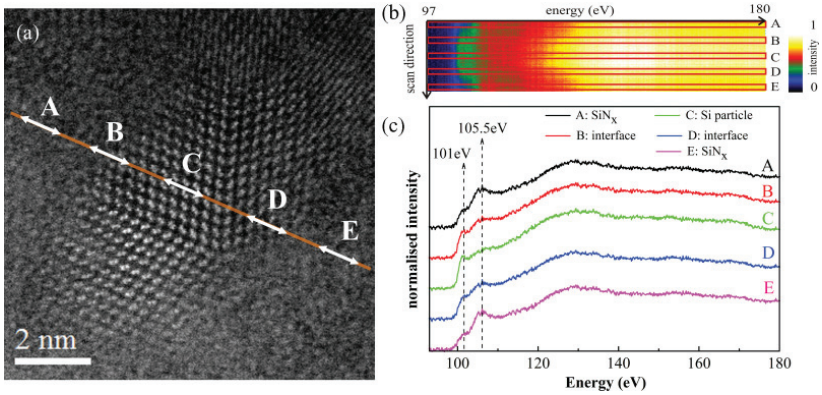

FIG. 3. (Color online) (a) A HAADF STEM image of a twinned Si NC in the film annealed at 1000 °C for 2 h, showing the trace of the Si $L_{2,3}$ edge EELS line scan. The parts of the line scan that are marked from A to E correspond to the parts of the raw spectrum image in (b) (the color scale corresponds to normalized intensity). (c) Averaged (and background subtracted) Si $L_{2,3}$ edge spectra from regions A to E, respectively.

Figure 4 shows Si $L_{2,3}$ edge EELS spectra (average of 10 adjacent spectra) taken at the cores of Si NCs of different sizes in the 1100-30 m sample. The horizontal axis corresponding to the energy loss was cross calibrated across datasets by means of the very characteristic silicon nitride peak at 105.5 eV from the matrix areas. As seen in Fig. 4, the edge shape changes dramatically as the particle size decreases from 10 to 3 nm. The edge onset gradually shifts to higher energy relative to the bulk and reaches a shift of 1.5 eV when the particle size drops to 3 nm. This behavior is similar to the observation of Batson and Heath,[13] who reported that the Si edge shape changes abruptly to a single parabolic band and a shift of 2 eV for H—terminated Si NCs smaller than 5 nm. The latter were prepared via a different method than the one used here (the gas-phase photolysis of a dilute Si_2H_6/He mixture in a gas flow cell and deposited on a holey carbon grid), albeit exhibiting a similar effect on the change of conduction band edge. Due to the lack of NCs smaller than 3 nm, the observation of quantum size effects at the Si $L_{2,3}$ edge has not been implemented in the 1000-2 h and 1100-2 h.

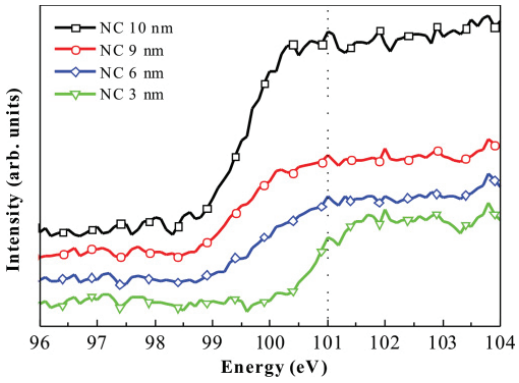

FIG. 4. (Color online) Si $L_{2,3}$ (background subtracted) EELS spectra taken at the Si NC cores with different sizes in the film annealed at 1100 °C for 30 min. The edge onset shifts and the edge shape changes with decreasing particle size. The Si peak energy at 101 eV is marked by the dot vertical line.

Figure 5 shows three distinct Si plasmon peaks acquired from Si NCs in three sets of samples. The low-loss EELS spectra presented are averaged adjacent spectra taken from a SMART acquisition linescan,[16] which was acquired in the center of the NCs. The 1100-2 h sample exhibits the narrowest plasmon peaks at 16.9 eV, of which the plasmon energy and shape correspond to that of bulk crystalline Si, confirmed in our experiment by comparison with the plasmon of the Si substrate (not shown). Plasmon peaks in the 1100-30 m are broad and have a large plateau on top, while plasmon peaks in the 1000-2 h are sharp at the lower energy side (around 17 eV) and have a shoulder at the higher-energy side (around 21 eV). It has been previously observed that, for NCs of Si, CdS, and Bi, the volume plasmon energy shifts toward higher energy, and the spectra are broadened with decreasing particle

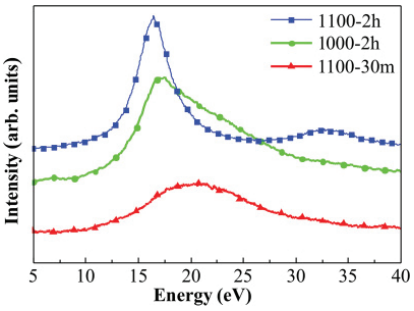

FIG. 5. (Color online) Selected low-loss EELS spectra acquired at the cores of Si NCs from samples under different annealing conditions. The shapes of the spectra are typical for each sample.

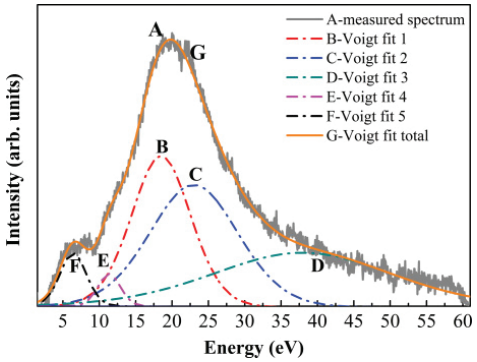

FIG. 6. (Color online) Zero-loss peak striped plasmon peak, acquired from the core of an Si NC in the film annealed at 1100 °C for 30 min. The different contributions are separated by fitting using the Voigt functional form. The first and the second Voigt peaks correspond to volume plasmon of Si NCs and their surrounding matrices, respectively.

size.[12,22,23] This is consistent with the observation in Fig. 5: the particles examined in the 1100-30 m and 1000-2 h are in the range size from 4 to 8 nm, while they are larger than 10 nm in the 1100-2 h.

Owing to the delocalized character of the plasmon excitation,[24] the sample volume contributing to the low-loss signal is significant. Therefore, the broadening of plasmon peaks of the Si NCs with small sizes is expected to contain some contribution from the vicinity of the surrounding silicon nitride matrix. The broad plasmon peaks in the low-loss EELS spectra were deconvoluted in five components using the Voigt functional form fitting method (Fig. 6). The first component corresponds to the volume plasmon of Si NCs, which were taken at the NC cores. The second component of the plasmon is the matrix contribution. Figure 7 shows the typical setting of EELS SMART acquisitions: the position of the matrix plasmon was verified independently by acquisition of low-loss EELS spectra from the matrix immediately surrounding each studied NC. The accuracy of the matrix plasmon energies depends on the density and the volume fraction of Si NCs in different samples. The determined values for the volume plasmon energies of the NCs and their adjacent matrix together with the particle size of three samples are summarized in Table I. The smaller peaks at around 5 and 10 eV correspond to the interband transition and surface plasmon energies of Si NCs, respectively.

Plasmon peaks of the matrix surrounding the Si NCs mostly have energies in the range of 20–24 eV, as seen in Table I. This indicates that the matrix is nonstoichiometric silicon nitride SiN_x ($x < 4/3$). It has been observed earlier that for silicon-rich nitride, the plasmon energy decreases from 24 to 17 eV depending on the Si excess in SiN_x.[25] The decrease of plasmon energy in SiN_x is attributed to the increase of Si-Si bond concentration. This result implies that Si agglomeration in the SiN_x films is not complete even after annealing at 1000 °C or above for a rather long time (30 min or more).

The NC size dependence of the Si volume plasmon energy was obtained, as shown in Fig. 8. The common trend in the 1100-30 m and 1000-2 h samples is that the volume plasmon energies shift toward higher energies with decrease in the particle sizes. For the former, the peak energy increases drastically when the diameter reaches ~5 nm. The blue shift of plasmon energy with decreasing the particle size attributed to the quantum size effect is described by Mitome *et al.*:[23]

$$E_P = \frac{\hbar^2 \pi^2 E_b}{\mu d^2 E_g} + E_b, \tag{1}$$

where $\hbar$ is the Planck constant, μ is the effective mass of an electron/hole pair in the material ($1/\mu = 1/m_e + 1/m_h$, where m_e and m_h are the electron and the hole effective masses, respectively), d is the particle diameter, E_p is the plasmon energy of the nanoparticle, E_b and E_g are the plasmon energy and the band gap for the bulk, respectively. This effective

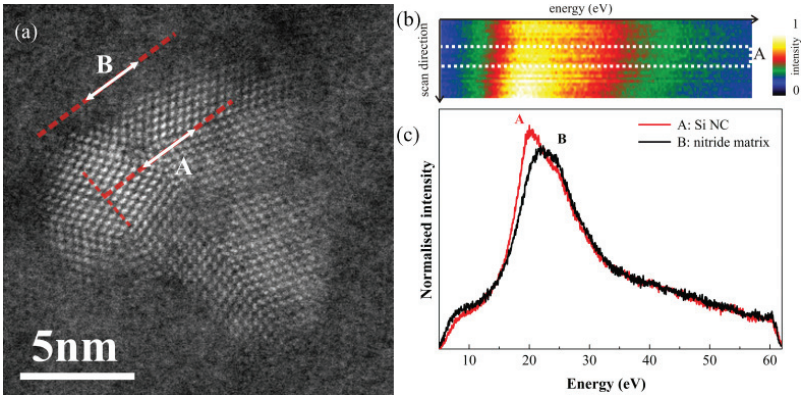

FIG. 7. (Color online) (a) The EELS SMART acquisitions for an Si nanotwin particle and its surrounding matrix in the film annealed at 1000 °C for 2 h. (b) The spectrum image of the SMART acquisition on the Si particle, where A corresponds to the line scan at the particle core (the color scale corresponds to normalized intensity). (c) Si NC and matrix plasmons from regions A and B in (a).

TABLE I. Plasmon energies of different size Si NCs and their surrounding matrices.

Sample	Particle diameter (nm)	Volume plasmon energy of Si NC (eV)	Plasmon energy of silicon nitride matrix (eV)	FWHM of Si volume plasmon peaks (eV)
1000-2 h	6.6 (twin)	17.33	20.36	3.22
	6.9 (twin)	17.38	20.10	3.64
	7.0 (twin)	17.36	20.10	4.11
	7.5 (twin)	17.20	19.90	4.36
	8.0	17.13	20.20	4.03
	8.9 (twin)	17.03	20.20	3.74
1100-30 m	3.8	18.56	23.85	9.82
	4.3	18.20	22.79	9.32
	5.2	17.80	23.03	8.73
	5.5	17.64	22.33	8.11
	5.6	17.60	20.10	5.90
	6.6	17.52	20.86	4.47
	7.0	17.34	21.31	3.22
	7.7 (twin)	17.33	20.10	3.82
1100-2 h	11.0	16.94	21.14	3.80
	20.4	16.90	20.10	3.51

mass model predicts the relationship between the particle size and its plasmon energy $E_P \approx 1/d^2$. The observed increasing volume plasmon energy of Si NCs in the 1100-30 m sample agrees well with predictions from this model as seen in the inset of Fig. 8. The rise of the volume plasmon energy in NCs of a semiconductor is known to be a result of the band gap expansion in the excitonic quantum confinement regime, which becomes significant at sizes smaller than the Bohr radius of bulk crystalline Si (around 5 nm). The experimental data of the 1100-30 m sample are best fitted by the equation:

$$E_p = 16.89 + 23.90/d^2, \tag{2}$$

plotted as the dotted line in Fig. 8. An energy shift $\delta E_p = 0.4$–1.6 eV with respect to the bulk plasmon energy of 16.9 eV is thus obtained for a NC size range of 3.8–7.7 nm in this sample. A similar shift measured by x-ray photoelectron spectroscopy was reported by Mannella *et al.* for porous Si with sizes of 2.4–3.4 nm.[26] From Eq. (2), an effective mass $\mu = 0.47m_0$ was estimated, where m_0 is the electron rest mass. This effective mass is much smaller than the reported value of $1.1m_0$ for freestanding Si nanoclusters obtained by Mitome *et al.*,[23] suggesting that the quantum confinement effect is stronger in our system. Nevertheless, this value is very close to that obtained in c-Si ($\mu = 0.48m_0$ at 300 K) by Barber[27] and a-Si/SiO_2 quantum wells by Lockwood *et al.*[28] These results imply the importance of the sample preparation method, which leads to different surface chemistry and shapes of Si NCs. For instance, Si clusters prepared by using SiH_4 as a precursor gas in Ref. 23 might be terminated by amorphous layers of polysilane around the clusters,[23] whereas our Si NCs are passivated by nitrogen. Additionally, the freestanding Si clusters reported in Ref. 23 were spherical in shape, while in our case, they are nonspherical and have

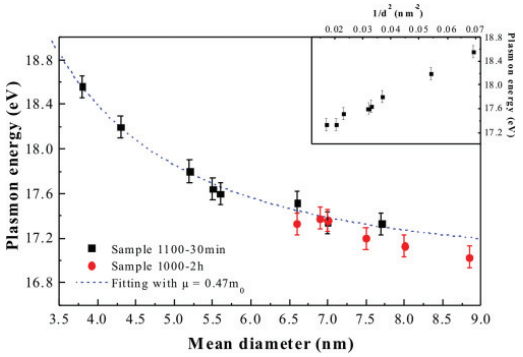

FIG. 8. (Color online) Size dependence of the plasmon energy in the 1100-30 m and 1000-2 h samples. The dot line is the least squares fit by effective mass theory to the data of the 1100-30 m. The inset shows the increase of plasmon energy proportional to the inverse square of particle diameter $E_P \approx 1/d^2$ in the 1100-30 m sample.

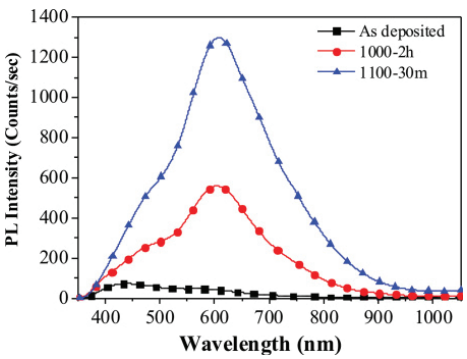

FIG. 9. (Color online) The PL spectra of the 1100-30 m, 1000-2 h, and as-deposited samples. Both the 1100-30 m and 1000-2 h exhibit a PL maximum centered at around $\lambda = 605$ nm (2.05 eV) with a small shoulder at $\lambda = 480$ nm (2.6 eV).

irregular morphologies, hence the confinement is expected to be stronger in some dimensions than others.

While the 1100-30 m sample provides data that fit nicely into the effective mass curve, the plasmon energy as a function of Si NC size in the 1000-2 h is systematically shifted down on the energy scale by approximately 0.2 eV. The fact that most of the particles examined in this latter sample include twins or other defects is a very likely reason for the weakening of the observed plasmon energy shift compared with similar-sized, defect-free particles in the 1100-30 m. A shift of ∼0.4 to 0.9 eV in plasmon energies due to lattice distortion in c-ZrO_2/α-Al_2O_3 has been reported by Yamada *et al*.[29] The decrease in plasmon energy of α-Al_2O_3 by 0.9 eV in that system was attributed to a 6% lattice expansion. The presence of lattice distortion, stacking faults, and dislocations inside the Si-twinned unit cells, as mentioned above, could thus alter the charge density and in turn change the plasmon energies. The observed downward shift in plasmon energies due to stacking faults and dislocations appears to be higher than the shift due to twinning effect, as evidenced by results obtained on a particle with a diameter of ∼6.6 nm. In this particle [Fig. 2(b)], the line scan was acquired close to a dislocation core and across a stacking fault. Although additional data would be required to confirm it, this observation is in good agreement with the report by Hanrath and Korgel that stacking faults strongly attenuate the plasmon signal of Ge nanowires.[30] Calculation of lattice distortions by using plasmon energy shift could further confirm this hypothesis. It is worth mentioning that the Si NCs in the 1100-2 h sample exhibit no remarkable blue shift at volume plasmon energies, which is expected since the sizes of these NCs are much larger than the quantum confined size range.

The combined observation of a blue shift of the plasmon energies and a shift of up to 1.5 eV in the core-loss Si $L_{2,3}$ edge onset of the particle as small as 3 nm (sample 1100-30 m) provide conclusive evidence of the presence of confinement effects in Si NCs within Si-rich nitrides. We attribute this blue shift to a specific quantum confinement effect, which raises the energy of the bottom of the conduction band relative to the Si $2p$ core level. This hypothesis agrees with the EELS data and conclusions from Batson and Heath[13] for H-terminated Si NCs with sizes <5 nm or from Sun *et al*.[31] for Si nanowires of 2.5 nm. Furthermore, the strong dependence of the observed blue shift on the size of the Si NCs fits very well within the general theoretical framework established by Delerue *et al*.[32] Using first-principles calculations, they estimated the recombination rate of electron-hole pairs in Si nanostructures and found that the balance between the size dependence of radiative and nonradiative events leads to the prediction of a blue shift of the luminescence for small crystallites. Indeed, our results are also in very good agreement with the PL energy shifts observed, for instance, for crystalline Si quantum dots embedded in silicon nitride reported by Kim *et al*.[7]

In addition to the electronic properties discussed above, the presence of defects in semiconductor crystals can strongly influence the electrical and optical properties of the material.[21,33] To relate luminescence properties with the nanostructure of Si NCs, the PL spectra of the 1100-30 m and 1000-2 h samples were measured and analyzed. Figure 9 compares the PL spectra from three samples: 1100-30 m, 1000-2 h, and as-deposited, excited at 325 nm by an ultraviolet PL spectroscopy at room temperature. The as-deposited film does not show any appreciable light emission, while the other two exhibit a strong PL maximum centered at around $\lambda = 605$ nm (2.05 eV), with a small shoulder at $\lambda = 480$ nm (2.6 eV), as shown in Fig. 9. These are in excellent agreement with the results and quantum confinement modeling obtained from Si NCs with a core diameter of 3 nm reported by Ledoux *et al*.[34]

A significantly lower PL intensity was obtained in the 1000-2 h sample compared to that in the 1100-30 m. The heavier defect density present in the 1000-2 h is evidently responsible for the large drop in PL intensity compared to that of the defect-free Si NCs in the 1100-30 m, which is in agreement with our STEM-EELS observations. Dangling bonds at dislocations can introduce extra electronic states in the band gap, which are referred to as intraband gap states and tend to trap carriers.[35] Furthermore, as the calculations of Delerue *et al*.[32] show, if these energy states are lying near the center of the band gap, they may be capable of trapping either electrons or holes and, hence, act as nonradiation recombination centers, which cause the decrease in light emission efficiency. Surface states in the Si NCs do not appear to play a major role, since the average particle sizes in both samples are comparable. These results clearly demonstrate the significant impact of crystal imperfections on the optical emission from Si NCs. Moreover, the PL results shown here provide strong support for our previous explanation of the weakening of quantum confinement effects in the 1000-2 h sample.

Finally, we briefly comment on the mechanisms of twin growth in Si NCs, for which temperature and time are crucial factors. If twinned NCs are formed by coalescence of small Si NCs, one would expect that the smaller crystals (<4 nm) are twin free because they have not grown to an impingement size.[36] Certainly, some rearrangements of the crystals are necessary before the crystal merging to get a twin relation. The twinned structure is unstable due to its higher free energy compared to twin-free structure. Twin boundaries do raise the energy of the system and should be considered as defects. The observation that big NCs (∼20 nm) are twin free indicates that, when given enough time, the system will lower its free energy by reconstructing and transforming into large twin-free particles. Annealing at 1100 °C for 30 min gives Si NCs with small grain size and size distribution, very few of which are twins. Annealing at 1100 °C for 2 h gives enough time for grain growth to reach a size where most of the crystals are without twins. Indeed, in the 1100-2 h sample, there is very little evidence of twins. Our argument until this point has been restricted to 1100 °C, where the atoms have sufficient diffusion rate to find their best positions in order to grow crystals without twinning at 1100 °C. At the lower temperature of 1000 °C for 2 h, however, the atoms have less mobility and are more likely to be trapped by one another, giving rise to an increase of twinned defects. This explains the higher density of twinning in the 1000-2 h compared to that in the 1100-30 m.

IV. CONCLUSION

We have demonstrated that the size, density, and structure of Si NCs embedded in a silicon nitride matrix can be controlled by varying the thermal annealing conditions. The

HRTEM/EFTEM analysis shows that the mean size and size distribution of Si NCs increase with increasing the annealing temperature for the same annealing time, and with increasing the annealing time for a fixed annealing temperature. The STEM-EELS and distributed dose (SMART) techniques were applied to this system to carry out a comprehensive study of quantum confinement effects as a function of the size and morphology of the Si NCs and are in qualitative agreement with carrier quantum confinement theory. The observation of twinning and defects in Si NCs and their impact on the blue shift of plasmon energy and PL intensities suggests a strong impact of crystal imperfections in the luminescence process of Si NCs. High-quality materials are needed in order to eliminate the nonradiative recombination and engineer the required band structure. Our direct evidence of quantum confinement in this system confirms the viability of Si-rich nitride as a matrix for nano-structured thin films in tandem solar cell stacks and opens up promising avenues for the exploitation of the higher band gap energy of SiN_x in photovoltaic applications.

ACKNOWLEDGMENTS

The authors would like to thank the University of Oslo for financial support. Phuong Dan Nguyen would like to thank Ole Bjørn Karlsen for useful discussions and for assistance with sample preparation. We also thank Augustinas Galeckas and Lars Olav Vestland for carrying out the PL measurements.

*Corresponding author: danpn@fys.uio.no

[1] M. A. Green, Prog. Photovolt: Res. Appl. **9**, 123 (2001).
[2] G. Conibeer, M. A. Green, D. König, I. Perez-Wurfl, S. Huang, X. Hao, D. Di, L. Shi, S. Shrestha, B. Puthen-Veetil, Y. So, B. Zhang, and Z. Wan, Prog. Photovolt: Res. Appl. **19**, 813 (2011).
[3] H. Tamura, M. Ruckschloss, T. Wirschem, and S. Veprek, Appl. Phys. Lett. **65**, 1537 (1994).
[4] N. Daldosso, M. Luppi, S. Ossicini, E. Degoli, R. Magri, G. Dalba, P. Fornasini, R. Grisenti, F. Rocca, L. Pavesi, S. Boninelli, F. Priolo, C. Spinella, and F. Iacona, Phys. Rev. B **68**, 085327 (2003).
[5] L. Pavesi, L. Dal Negro, C. Mazzoleni, G. Franzò, and F. Priolo, Nature **408**, 440 (2000).
[6] M. S. Yang, K. S. Cho, J. H. Jhe, S. Y. Seo, J. H. Shin, K. J. Kim, and D. W. Moon, Appl. Phys. Lett. **85**, 3408 (2004).
[7] T. W. Kim, C. H. Cho, B. H. Kim, and S. J. Park, Appl. Phys. Lett. **88**, 123102 (2006).
[8] P. RJ Wilson, T. Roschuk, K. Dunn, E. N Normand, E. Chelomentsev, O. HY Zalloum, J. Wojcik, and P. Mascher, Nanoscale Res. Lett. **6**, 168 (2011).
[9] J. Kistner, X. Chen, Y. Weng, H. P. Strunk, M. B. Schubert, and J. H. Werner, J. Appl. Phys. **110**, 023520 (2011).
[10] M. Wang, D. Li, Z. Yuan, D. Yang, and D. Que, Appl. Phys. Lett. **90**, 131903 (2007).
[11] P. R. Coxon, Y. Chao, B. R. Horrocks, M. Gass, U. Bangert, and L. Šiller, J. Appl. Phys. **104**, 084318 (2008).
[12] N. D. Browning, M. F. Chisholm, and S. J. Pennycook, Nature **366**, 143 (1993).
[13] P. E. Batson and J. R. Heath, Phys. Rev. Lett. **71**, 911 (1993).
[14] Y. W. Wang, J. S. Kim, G. H. Kim, and K. S. Kim, Appl. Phys. Lett. **88**, 143106 (2006).
[15] O. L. Krivanek, G. J. Corbin, N. Dellby, B. F. Elston, R. J. Keyse, M. F. Murfitt, C. S. Own, Z. S. Szilagyi, and J. W. Woodruff, Ultramicroscopy **108**, 179 (2008).
[16] K. Sader, B. Schaffer, G. Vaughan, R. Brydson, A. Brown, and A. Bleloch, Ultramicroscopy **110**, 998 (2010).
[17] F. Delachat, M. Carrada, G. Ferblantier, A. Slaoui, C. Bonafos, S. Schamm, and H. Rinnert, Physica E **41**, 994 (2009).
[18] F. Delachat, M. Carrada, G. Ferblantier, J. J. Grob, and A. Slaoui, Nanotechnology **20**, 415608 (2009).
[19] Y. Q. Wang, R. Smirani, and G. G. Ross, Nano Lett. **4**, 2041 (2004).
[20] X. Jiang and C. L. Jia, Appl. Phys. Lett. **80**, 2269 (2002).
[21] J. E. Northrup, M. L. Cohen, J. R. Chelikowsky, J. Spence, and A. Olsen, Phys. Rev. B **24**, 4623 (1981).
[22] P. N. H. Nakashima, T. Tsuzuki, and A. W. S. Johnson, J. Appl. Phys. **85**, 1556 (1999).
[23] M. Mitome, H. Yamazaki, H. Takagi, and T. Nakagiri, J. Appl. Phys. **72**, 812 (1992).
[24] R. F. Egerton, *Electron Energy—Loss Spectroscopy in the Electron Microscope* (Plenum Press, New York and London, 1986), p. 131 .
[25] V. A. Gritsenko, H. Wong, J. B. Xu, R. M. Kwok, I. P. Petrenko, B. A. Zaitsev, Yu. N. Morokov, and Yu. N. Novikov, J. Appl. Phys. **86**, 3234 (1999).
[26] N. Mannella, G. Gabetta, and F. Parmigiani, Appl. Phys. Lett. **79**, 4432 (2001).
[27] H. D. Barber, Solid State Electron. **10**, 1039 (1967).
[28] D. J. Lockwood, Z. H. Lu, and J. M. Baribeau, Phys. Rev. Lett. **76**, 539 (1996).
[29] S. Yamada, J. Ohta, and H. Kusanagi, J. Appl. Phys. **88**, 5206 (2000).
[30] T. Hanrath and B. A. Korgel, Nano Lett. **4**, 1455 (2004).
[31] X. H. Sun, Y. H. Tang, P. Zhang, S. J. Naftel, R. Sammynaiken, T. K. Sham, H. Y. Peng, Y.-F. Zhang, N. B. Wong, and S. T. Lee, J. Appl. Phys. **90**, 6379 (2001).
[32] C. Delerue, G. Allan, and M. Lannoo, Phys. Rev. B **48**, 11024 (1993).
[33] P. E. Batson, Phys. Rev. B **61**, 16633 (2000).
[34] G. Ledoux, J. Gong, F. Huisken, O. Guillois, and C. Reynaud, Appl. Phys. Lett. **80**, 4834 (2002).
[35] J. Nelson, *The Physics of Solar Cells* (Imperial College Press, London, 2003), p. 211.
[36] Y. Q. Wang, R. Smirani, G. G. Ross, and F. Schiettekatte, Phys. Rev. B **71**, 161310R (2005).

Paper II

P. D. Nguyen, D. M. Kepaptsoglou, Q. M. Ramasse, M. F. Sunding, L. O. Vestland, T. G. Finstad and A. Olsen

Impact of oxygen bonding on the atomic structure and photoluminescence properties of Si-rich silicon nitride thin films

Journal of Applied Physics 112, 073514 (2012)

Impact of oxygen bonding on the atomic structure and photoluminescence properties of Si-rich silicon nitride thin films

P. D. Nguyen,[1,a)] D. M. Kepaptsoglou,[2] Q. M. Ramasse,[2] M. F. Sunding,[1] L. O. Vestland,[1] T. G. Finstad,[1] and A. Olsen[1]
[1]*Department of Physics, University of Oslo, P.O. Box 1048, Blindern, NO-0316 Oslo, Norway*
[2]*SuperSTEM Laboratory, STFC Daresbury Campus, WA4 4AD Warrington, Cheshire, United Kingdom*

(Received 11 July 2012; accepted 30 August 2012; published online 5 October 2012)

The atomic structure and optical properties of Si-rich silicon nitride thin films have been for decades the subject of intense research, both theoretically and experimentally. It has been established in particular that modifying the chemical composition of this material (e.g., the Si excess concentration) can lead to dramatic differences in its physical, optical, and electrical properties. The present paper reports on how the incorporation of oxygen into silicon nitride networks influences their chemical bonding and photoluminescence properties. Here, by using a combination of analytical scanning transmission electron microscopy and x-ray photoelectron spectroscopy it is demonstrated that the structure of Si-rich silicon nitride with low O content can be described by the co-existence of Si nanocrystals in a Si_3N_4 matrix, with occasional localized nano-regions of a Si_2ON_2 phase, depending on the amount of excess Si. Furthermore, it is shown that the structure of silicon nitride with high O content can be adequately described by a so-called random bonding model, according to which the material consists in bonded networks of randomly distributed tetrahedral SiO_xN_{4-x} (where $x = 0$, 1, 2, 3, and 4). Photoluminescence measurements indicate that the effect of O is to introduce a gap state in the band gap of Si_3N_4 matrix. When a large amount of O is introduced, on the other hand, the photoluminescence measurements are in agreement with a shifted conduction band minimum in the dielectric. For both cases (high and low O content), Si dangling bonds were found to give rise to the deep level in the band gap of the nitride matrix, causing the dominant emission band in the photoluminescence of the films. © *2012 American Institute of Physics*. [http://dx.doi.org/10.1063/1.4756998]

I. INTRODUCTION

There has recently been a tremendous interest in thin films of silicon nitride with embedded Si nanocrystals (NCs), prompted by the large number of potential applications of this system.[1] Si NCs can for instance be used in Si photonics with on-chip incorporation of optical functions within existing microelectronics CMOS technology.[2] These systems have also shown nonlinear optical effects, potentially paving the way for nonlinear photonics with a wide range of applications such as sensing, high rate signal processing, and broad band optical modulation.[3] In addition, Si nitride films are an integral part of existing solar cell technology, and embedded Si NCs offer a route to creating stacked variable bandgap structures.[4] In most of these applications, while the importance of defects, their structure, and their influence on physical processes in potential devices are well recognized, they are often not satisfactorily understood. Although optical methods such as photoluminescence (PL) have been commonly used to characterize embedded Si NCs, it has been difficult to identify the exact mechanism responsible for the PL response of these systems. Three mechanisms are thought to yield luminescence in this system under optical excitation: (i) radiative electron–hole recombination in Si NCs arising from quantum confinement effects,[5] (ii) radiative recombination at defect centers in the nitride network,[6] and (iii) radiative recombination at localized bonding states at Si NCs/nitride interfaces, which may vary upon different preparation techniques.[7] Not only can all three of these distinct mechanisms be involved at the same time in the PL process, nonradiative recombination processes and excitation energy transfer between different centers may also play a part.[8] Furthermore, it has been found that Si nitride films produced by plasma-enhanced chemical vapor deposition are easily oxidized by exposure to air after deposition.[9,10] This high reactivity was attributed to the porous structure of the observed films, which were typically fabricated at low substrate temperatures, as it likely permitted moisture from the air to penetrate into them.[10] Consequently, luminescent centers related to the Si–O bonds may be expected.[11] Finally, it was shown that many kinds of defects can exist in oxynitrides with high densities and non-uniform distributions, which, in turn, can act as electron or hole traps and cause a deviation from theoretical predictions.[12,13]

Nguyen *et al.* have previously observed quantum confinement effects as a function of the size and morphology of Si NCs embedded in a Si nitride thin film.[14] However, a broader, more complete picture is still lacking, which would take into account any unintentional incorporation of O and would describe the correlation between the local chemical bonding, intrinsic and extrinsic defects, and the physical

[a)]Author to whom correspondence should be addressed. Electronic mail: danpn@fys.uio.no.

TABLE I. RF power supplies and respective atomic concentrations (at. %) of SRN layers of the three annealed samples.

Sample	RF power to Si target (W)	RF power to Si_3N_4 target (W)	Si (at. %)	N (at. %)	O (at. %)
SN1	150	100	62	30	8
SN2	100	100	47	39	14
SN3	50	150	40	28	32

properties of Si-rich Si nitride films (SRN), such as their PL. In this paper, we seek to address some of these open questions by combining several experimental techniques yielding both bulk-averaged and local atomic-scale information for studying at different length scales the impact of variations in composition and chemical bonding on the SRN film structure. The aim is to improve our understanding of the effect of oxygen incorporation into Si–N networks upon their luminescence properties. The information about atomic bonding and the identification of precise atom locations in our study may assist in validating different chemical bond distribution and PL models for the Si nitride system.

II. EXPERIMENTAL

Thin films composed of a nominally stoichiometric Si nitride (Si_3N_4) buffer layer (~20 nm) followed by an SRN layer (~40 nm) were deposited on (100)-oriented single-crystal Si substrates by radio frequency (RF) magnetron sputtering in an Ar atmosphere. The Si substrates were cleaned using a standard RCA (Radio Corporation of America) cleaning process followed by a dip in a 10% HF solution to remove the native oxide, then dried in N_2 gas, and put into the deposition chamber. Prior to sputtering, the chamber was evacuated to 5×10^{-7} mbar. *In situ* Ar pre-sputtering of the targets was performed in order to remove any Si oxide on the target surface. The flow rate of Ar was maintained at a constant rate of 40 standard cubic centimeter per minute, and the pressure in the chamber was kept at 6×10^{-3} mbar during the film deposition. The excess Si content in the SRN layers was achieved by co-sputtering and deposition from Si and Si_3N_4 targets without any intentional substrate heating. Three different sets of samples, namely SN1, SN2, and SN3, having different Si excess were achieved by adjusting the sputtering rates for the Si and Si_3N_4 targets individually. The composition of these samples ranges from high excess Si content (SN1) to low excess Si content (SN3): see Table I. All the as-deposited samples were confirmed to be amorphous by transmission electron microscopy (TEM) imaging and electron diffraction. Furthermore, the Si nitride buffer layers exhibited a very high porosity compared to the SRN layers. With the purpose of forming Si NCs and induce phase separation in the nitride matrix, the samples were subsequently annealed at 1100 °C for 2 h in a sealed SiO_2 glass tube evacuated to a vacuum of better than 1×10^{-2} mbar.

TEM specimens were prepared for cross-sectional observations by mechanical grinding and finished with low-angle Ar-ion milling (at 5 keV) in a Gatan PIPS 691 Precision Ion Polishing System. High-resolution transmission electron microscopy (HRTEM) and energy-filtered transmission electron microscopy (EFTEM) observations were performed at 200 keV primary beam energy with a JEOL 2010 F microscope equipped with a Gatan Imaging Filter. EFTEM images were acquired using the Si bulk plasmon peak at 17 eV with an energy slit width of 2 eV. The scanning transmission electron microscopy coupled with electron energy-loss spectroscopy (STEM-EELS) experiments were performed at 100 keV in a C_s-corrected Nion UltraSTEM equipped with a Gatan Enfina spectrometer. The cold field electron emitter of this instrument has a native energy spread of 0.35 eV, as determined from the full width at half maximum (FWHM) of the zero-loss peak in typical operating conditions. For the core-loss EELS acquisition, the collection semi-angle was 32 mrad with a probe convergence semi-angle of 30 mrad.

X-ray photoelectron spectroscopy (XPS) measurements were carried out using a Kratos AxisUltra^{DLD} instrument with a monochromatic Al Kα radiation. The employed settings allowed for a resolution of 0.57 eV as determined by the FWHM of the Ag $3d_{5/2}$ peak. Depth profiling was performed using Ar ion sputtering (at 4 keV) combined with sample rotation. The binding energies of photoemission spectra were calibrated by referring the position of the C 1*s* peak from adventitious C on the un-etched surface to 285 eV binding energy. PL measurements were performed by excitation with the 325 nm line of a He–Cd laser at room temperature. The XPS core-level photoemission spectra and PL spectra were fitted by a standard nonlinear least-squares fitting procedure using Voigt functions.

III. RESULTS AND DISCUSSION

A. Chemical and structural characterization

Figure 1 shows cross-sectional HRTEM images of the SRN layers of the three annealed samples. After annealing at

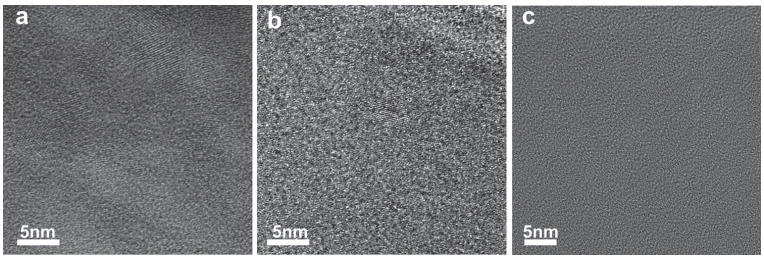

FIG. 1. (a)–(c) Cross-sectional HRTEM of SN1, SN2, and SN3, respectively. (a),(b) Distribution of Si NCs in which lattice planes can be seen clearly. By contrast, no NC was observed in SN3.

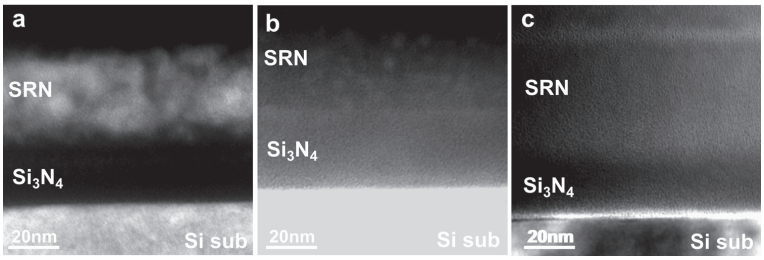

FIG. 2. Cross-sectional EFTEM at 17 eV (using a 2 eV slit) images of (a) SN1, (b) SN2, and (c) SN3. Bright contrast corresponds to a higher elemental concentration of Si.

1100 °C for 2 h, sample SN1 and SN2 exhibited an extensive phase separation evidenced by the formation of NCs embedded in the amorphous matrix. The width of the observed lattice fringes in HRTEM and electron diffraction patterns confirmed that the NCs in these samples are indeed Si. Sample SN1 has a high density of NCs with a rather large crystal size distribution (~3–10 nm) while sample SN2 has much lower density and smaller crystal size and size distribution (~3–5 nm). In contrast, sample SN3 shows no visible NCs, amorphous phases dominating the entire film structure. Figures 2(a)–2(c) show EFTEM images acquired at the bulk Si plasmon energy (17 eV) from the three samples after annealing. For samples SN1 and SN2, the brighter areas in the SRN layers correspond to the Si clusters, while the image from sample SN3 has a homogeneous grey contrast confirming the absence of cluster formation. This observation further confirms the difference in structure between the three annealed samples, which thus depends strongly on their chemical composition, from low to high Si excess content.

Information about bonding structure and chemical composition of the three annealed samples was obtained by XPS. Measurements show the presence of Si, N, as well as O in the samples as witnessed from the Si 2*p*, N 1*s*, and O 1*s* peaks (Figure 3(a)). Figures 3(b)–3(d) show the film

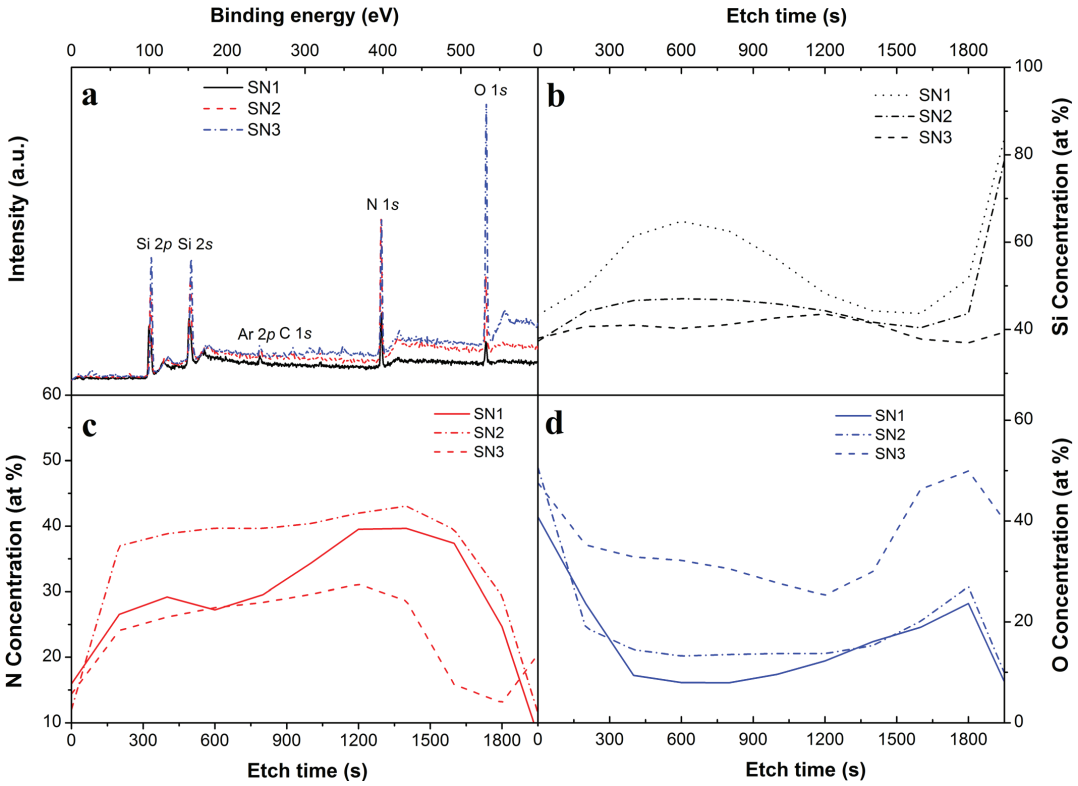

FIG. 3. (a) The experimental XPS survey spectra for all elements. (b)–(d) concentration of Si, N, and O, respectively, in the three annealed samples plotted as a function of etching time.

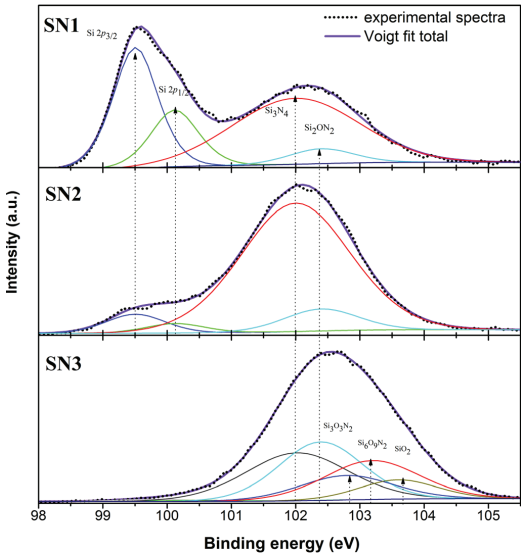

FIG. 4. The experimental Si 2*p* spectra (dotted lines) and component peaks (solid lines) obtained from the spectral deconvolution for the three annealed samples.

concentrations, determined by integrating the areas under the XPS peaks and plotted as a function of sputtering time (which corresponds to film depths). In all three investigated films the concentration of O is higher at the film surface (from 0 to 200 s sputtering time) and in the Si nitride buffer layer (from 1600 s sputtering time). Out of the three samples, sample SN1 exhibits the highest Si and lowest O concentration, while sample SN3 has the lowest Si concentration but the highest O concentration. We will focus in the following on XPS data acquired at a depth corresponding to the middle part of the SRN layer, i.e., from 400 to 800 s sputtering time. The elemental concentration for samples SN1, SN2, and SN3 at that depth is given in Table I.

Figure 4 shows the measured XPS Si 2*p* spectra of the three annealed samples, and their component peaks are obtained by the deconvolution of the spectra. The Voigt functional form-fitting method was used for fitting the spectra after standard Shirley background subtractions. $Si–Si_4$ and five other possible Si-centered tetrahedral configurations, SiO_xN_{4-x} (where x = 0, 1, 2, 3, and 4), were used to carry out the fitting procedure. The calculation of the binding energies of these tetrahedral units is based on the assumption that the displacement of the binding energy is linear with the increase of the coordination number of oxygen or nitrogen.[15] From the resolved component peaks, the corresponding tetrahedra together with their binding energies and relative atomic percentages are listed in Table II. For samples SN1 and SN2, the experimental spectra consist of two distinct peaks. The low energy peak at 99.5 eV, which is resolved into a $2p_{3/2}$-$2p_{1/2}$ doublet (as seen in Figure 4), can be readily assigned to bulk crystalline Si ($Si–Si_4$ tetrahedral unit). This information combined with the initial EFTEM observation

TABLE II. Structural phase components and their relative atomic percentages of the three annealed samples.

	Tetrahedron[a,b,c]	Bonding unit	Binding energy (eV)[a]	SN1	SN2	SN3
Relative atomic percentages (at. %)	$Si–Si_4$	Si	99.6	47.38	9.67	1.47
	$Si–N_4$	Si_3N_4	102	47.06	80.91	28.05
	$Si–ON_3$	Si_2ON_2	102.4	5.56	9.42	27.94
	$Si–O_2N_2$	$Si_3O_3N_2$	102.8			12.93
	$Si–O_3N$	$Si_6O_9N_2$	103.2			21.05
	$Si–O_4$	SiO_2	103.6			8.55

[a]Reference 14.
[b]Reference 15.
[c]Reference 16.

from these two samples further confirms the precipitation of Si from the SRN film. The Si crystalline content was determined to be ~47% and 9% in samples SN1 and SN2, respectively, by comparing the integrated intensity of the 99.5 eV peak with the total peak intensity. This is again consistent with TEM observations. In both samples, the higher energy peak at around 102.2 eV can only be fitted by a combination of $Si–N_4$ (Si_3N_4) and $Si–ON_3$ (Si_2ON_2). For sample SN3, the measured Si 2*p* spectrum shows only one symmetric peak at 102.8 eV, implying the absence of any pure Si phase in this sample.

There exist two extreme models, namely, random-bonding model (RBM) and random-mixture model (RMM) that have frequently been used to describe the chemical bond distribution in amorphous silicon oxy-nitride (a-SiO_xN_y).[13,15–17] According to the RBM, a-SiO_xN_y is composed of five types of tetrahedra described by SiO_xN_{4-x} (where x = 0, 1, 2, 3, and 4). This in turn implies that in this model the Si 2*p* spectrum must consist of a single broad peak. As seen in Figure 4, the experimental Si 2*p* spectra of sample SN1 and SN2, both considered to be Si rich, clearly do not agree with the RBM. This model appears to underrate the available fraction of $Si–Si_4$ tetrahedra, which are responsible for the observed bulk Si peak at 99.5 eV. Furthermore, the peak at around 102.2 eV corresponding to the residual matrices of sample SN1 and SN2 can only be fitted with two components: $Si–N_4$ and $Si–ON_3$. This again is in contradiction with an RBM description of these samples. The RMM on the other hand predicts that a-SiO_xN_y is a mixture of stable SiO_2 and Si_3N_4 phases, together with a pure Si phase, if Si is in excess. Hence the Si 2*p* spectrum should show the corresponding component peaks. However, the deconvolution of our experimental spectra (Figure 4, Table II) clearly shows the presence of $Si–ON_3$ tetrahedra that are not expected in the RMM. Moreover, the RMM model predicts a very strong proportion of $Si–O_4$ tetrahedra that correspond to a SiO_2 phase, which is not observed in samples SN1 and SN2. It is thus clear that neither the RBM nor the RMM can be used to describe our experimental data for SN1 and SN2. The experimental Si 2*p* spectrum of sample SN3, however, can be fitted almost perfectly with the RBM, suggesting that the film comprises five types of tetrahedra, as shown in Figure 4 and Table II.

Previously, Gritsenko *et al*. and Novikov *et al*. reported that neither RBM nor RMM could adequately describe the structure of SiN_x and SiO_x films.[16,18] Instead, they proposed an intermediate model, according to which the SiN_x and SiO_x structures comprise five types of tetrahedral units, as in the RBM, but for which the probability of finding a given tetrahedron type is not described by the RBM. The intermediate model is based on the assumption that there is a phase separation in the nitride or oxide matrices including Si clusters, sub-oxide and SiO_2, or sub-nitride and Si_3N_4 matrices. The local variation of the chemical composition between these phases will lead to large scale potential fluctuations for electrons and holes, thus increasing the probability of localized electrons and holes in potential wells. Nevertheless, direct evidence of the existence of Si clusters with small sizes as well as their spatial distribution in the oxide or nitride matrices are not provided in their works.[16,18]

In order to quantitatively confirm the validity of this "intermediate" model for our film structures, we carried out EELS measurements in an aberration-corrected STEM. The advantage of this experimental setup is that the scanned electron probe is sub-angstrom in size, and therefore the chemical and electronic structure information is obtained on an atomic scale. This allows us to determine whether the distribution of O is uniform within the sample and to confirm the type of bonding suggested by the intermediate model. The distributed-dose EELS SMART[19] scan technique was employed in order to minimize radiation damage in the notoriously beam sensitive Si nitride layers.

EELS SMART line scans across the whole film structure from the Si substrate to the surface of sample SN1 and SN2 are shown in Figures 5(a) and 5(c), respectively. The detector dispersion setting was chosen to cover an energy range from 70 to 700 eV allowing the Si $L_{2,3}$, N K, and O K edges to be simultaneously recorded. It is worth mentioning that the dark contrast in STEM high-angle annular dark-field (HAADF) imaging can be interpreted as pores in the bright contrast solid structure. As seen in Figures 5(a) and 5(c), the Si nitride buffer layers have a higher density of pores than the SRN layers. Figure 5(b) shows background-subtracted (using a power law model) Si $L_{2,3}$ edge EEL spectra extracted from the SMART line scan at different positions along the direction normal to the film structure and averaged over 20 adjacent data points to improve the signal-to-noise ratio. Position A corresponds to the Si substrate and the spectrum shows a sharp onset at 99 eV, reaching a maximum at

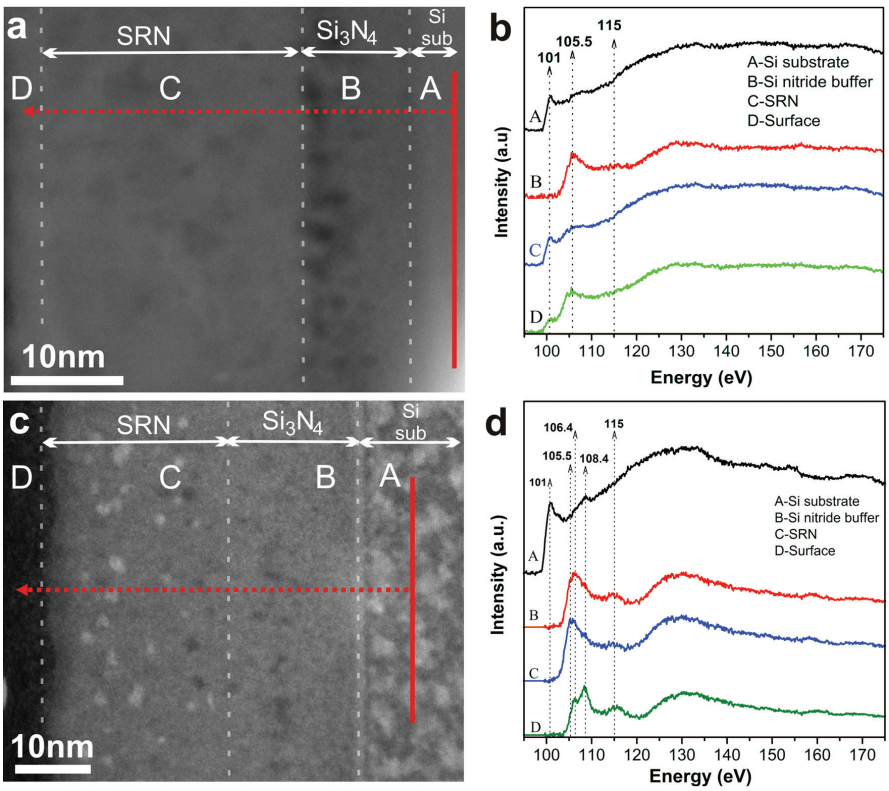

FIG. 5. (a) and (c) HAADF STEM survey image of sample SN1 and SN2, respectively, showing the position of the EELS SMART line scan acquisition across the film structure. The white spots in (c) are probably due to surface contaminations that do not alter the results. (b),(d) Averaged (and background subtracted) Si $L_{2,3}$ edge spectra, taken at different areas through the whole film depth of sample SN1 and SN2, respectively.

about 101 eV, characteristic of pure Si. Spectrum B was acquired in the Si nitride buffer layer next to the substrate and exhibits a sharp peak at 105.5 eV, which is the "fingerprint" of the Si_3N_4 phase, along with a broad secondary maximum at 115 eV. Moving further into the SRN layer where spectrum C was acquired, these two peaks decrease in intensity, and the energy loss near-edge fine structure (ELNES) becomes very similar to that of spectrum A, taken inside the Si substrate where the signal from Si crystalline bulk is dominant. Finally, spectrum D corresponds to the film surface: in addition to a weak sharp edge onset at 99 eV, its main peak is again centered around 105.5 eV. From the fine structure of these EELS edges it is possible to conclude that the SRN layer in sample SN1 comprises mostly of crystalline Si in a residual Si_3N_4 matrix.

Figure 5(d) shows background-subtracted Si $L_{2,3}$ edge EEL spectra extracted from a similar SMART line scan in sample SN2. As can be seen, spectrum C acquired in the SRN layer is very different from that of sample SN1. The edge onset at 99 eV and the sharp peak at 101 eV is not observed. Instead, a double peak (105.5 eV and 106.4 eV) is found. The first peak at 105.5 eV can be assigned to the presence of Si–N bonds, whereas the second peak at 106.4 eV can be associated with the presence of Si–O bonds: these peak energies closely coincide with reference spectra taken in pure Si_3N_4 and Si_2ON_2 phases.[20] Besides, a more intense broad secondary maximum at 115 eV is observed, which can be traced to O nearest neighbors in Si_2ON_2.[20] This indicates that the atomic environment around Si atoms consists of N and O atoms. It also reflects the significantly lower crystalline content of sample SN2: in the broad averaged lines scans the signature of crystalline Si is not detected. In contrast, the atomic environment of Si atoms in the SRN layer of sample SN1 is found to consist mostly of Si atoms, in agreement also with the very high crystalline content in the sample. In addition, spectrum D corresponding to the surface of sample SN2 exhibits a strong peak at 108.4 eV, which is the "fingerprint" of the SiO_2 phase. These observations are in good agreement with the high O content found in the XPS quantification results.

Figures 6(a) and 6(b) show the corresponding background-subtracted N *K* and O *K* edges EEL spectra, respectively, extracted from the SMART line scan at the same positions as the spectra from Figure 5(b). Peaks at 401 eV and 533 eV are observed for the N *K* and O *K* edges respectively. Comparing the experimental N *K* and O *K* ELNES to first-principles supercell calculations of the N *K* and O *K* edge ELNES from the literature[20] allows us to confirm the phase identification. The features of the N *K* edges in spectra A and C, corresponding to the sample surface and the Si nitride buffer layer, respectively, are in good agreement with the ELNES of either the Si_3N_4 phase or the Si_2ON_2 phase calculated by Ching *et al.*[20] On the other hand, the ELNES observed for the N *K* edge at position B within the SRN film resembles more the reported calculations of Si_3N_4 phase.[20] Regarding the O *K* edges, the observed ELNES in all spectra are compatible with the calculated ELNES of Si_2ON_2 phase. A similar result is obtained for sample SN2, except that the intensity of the N *K* edge at position B within the SRN layer is much higher than that of

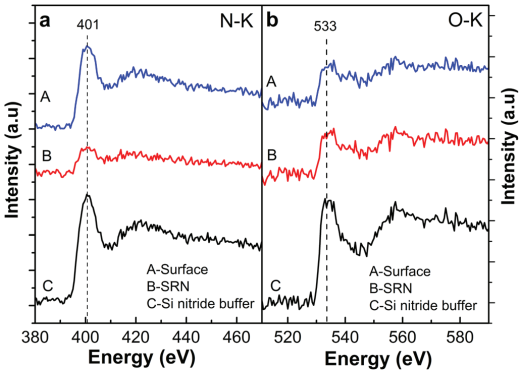

FIG. 6. (a) Averaged (and background subtracted) N *K* and (b) O *K* edge spectra, taken in different areas through the whole film depth of SN1.

sample SN1. This can be explained by the higher N content in sample SN2 also seen in the XPS quantification results.

In short, the agreement between averaged information obtained from core-loss EELS line scans and the XPS results is satisfactory. As shown by EELS lincescans, we suggest that the SRN layer in sample SN1 is dominated by Si precipitates and the residual matrix consists of mainly Si_3N_4 phase, whereas in sample SN2 the matrix involves Si_3N_4 phase and a minority of Si_2ON_2 phase with fewer Si precipitates.

In order to determine more precisely the distribution of the various species within the active SRN layers, very localized core-loss EELS scans were recorded in areas of the film containing only the nitride matrix and at the interfaces between Si NCs and the matrix of sample SN1 and SN2. While for sample SN1 the Si NCs were found to be mostly surrounded by a pure Si_3N_4 matrix, for sample SN2, in some cases (about 30% of observed NCs), the signature of the Si_2ON_2 phase was detected at the interface between a Si NC and its surrounding matrix. An example of this is shown in Figure 7. Figure 7(a) shows a STEM survey image of a 2 nm Si particle in sample SN2, where the trace of the core-loss EELS line scan taken across the particle is marked. Figure 7(c) shows background-subtracted, averaged Si $L_{2,3}$ EEL spectra from the line spectrum image in Figure 7(b). The spectra correspond to the areas marked A–C in Figures 7(a) and 7(b), respectively. Spectrum B in Figure 7(c) taken from the particle core shows a broad shoulder onset at 99 eV (the pure Si NC) and a pronounced peak at 105.5 eV corresponding to Si_3N_4 (the surrounding matrix, above and below the NC through the film thickness). In the spectra from areas A and C that correspond to the matrix/NC interface, a similar peak is present at 105.5 eV, but in addition a weak peak in the fine structure appears at 115 eV. As explained above, this can be traced to O nearest neighbors in Si_2ON_2 and could indicate the presence of a small amount of Si_2ON_2. Our observation of pure Si NCs embedded in the Si_3N_4 matrix, plus some occasional, very localized "pockets" of Si_2ON_2, is in good agreement with the intermediate model. Importantly, it confirms the existence of variations in the local chemical composition.

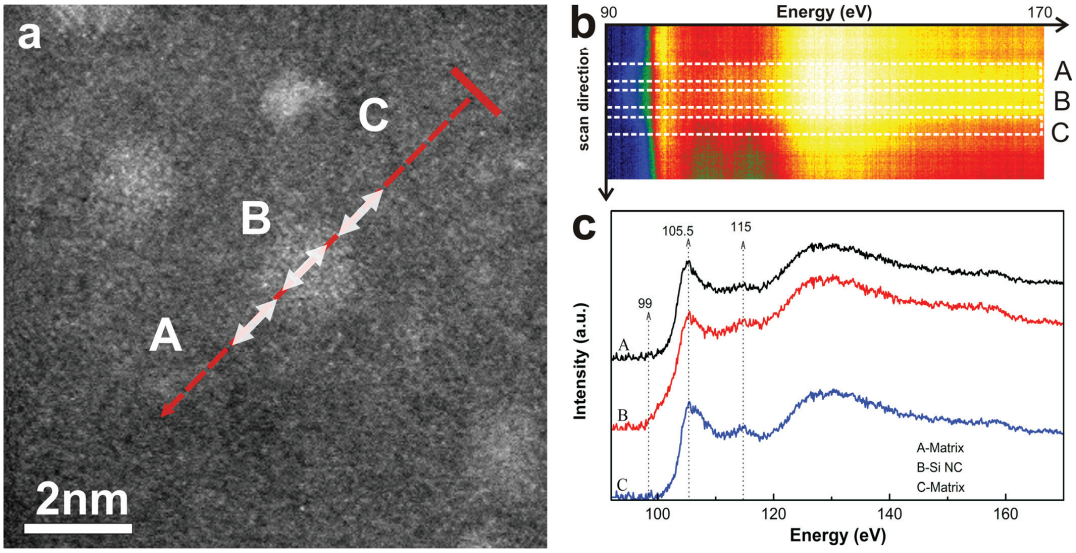

FIG. 7. (a) HAADF STEM survey image of a Si NC in sample SN2, showing the trace of the Si $L_{2,3}$ edge EELS line scan. The parts of the line scan that are marked from A to C correspond to the parts of the raw spectrum image in (b) (the color scale corresponds to normalized intensity). (c) Averaged (and background subtracted) Si $L_{2,3}$ edge spectra from regions A to C.

B. Photoluminescence properties

None of the as-deposited samples showed any appreciable light emission, in contrast to the improved luminescence properties of the annealed samples. Broad luminescence bands were observed between 1.2 and 3.6 eV for the three annealed samples, among which sample SN3 exhibits the strongest PL peaks overall. The PL spectra were decomposed into several components in order to identify individual constituents of the emission spectra. The Voigt functional form-fitting method was found to be satisfactory for fitting the data: the results of this analysis are shown in Figure 8. The individual peak energies and their respective contributions are presented in Table III. The resolved bands are centered at around 1.8 eV (named quantum levels QL1 and QL2 at 1.76 eV and 1.79 eV, respectively), 2.0 eV (named defect level DL1), and 2.6 eV (DL2) for samples SN1 and SN2. By contrast, 2.1 eV (DL3) and 2.7 eV (DL4) bands are found for sample SN3.

With regard to the red light emission, Kim *et al.*[21] reported for a series of Si NCs embedded in Si nitride matrix films that when the Si crystal size was decreased from 6.1 to 2.6 nm, the PL peak energy blueshifted from 1.46 eV to 3.02 eV due to quantum confinement effects. The energy gap (E) of Si nanocrystals can in the effective mass approximation be expressed as $E = E_{bulk} + C/d^2$, where d is the diameter of the Si quantum dot.[1,21,22] According to Kim *et al.*,[21] $E\,(eV) = 1.16 + 11.8/d^2$. From this, the energy gap of Si NCs with a mean size of 4–5 nm is estimated to be 1.76–1.79 eV, which is in agreement with our TEM and PL observation in sample SN1 and SN2, indicating that the red emission (QL1 and QL2 in Figure 8 and Table III) arises from band-to-band recombination in the Si NCs. The slight blueshift of these bands from 1.76 eV (QL1) to 1.79 eV (QL2) is expected due to the reduction of NC size in sample SN2 compared to SN1. The relative contribution of these bands in the PL spectra is 37 and 21% for sample SN1 and SN2, respectively. These different contributions can be explained by the much lower Si NC content in sample SN2 compared to sample SN1

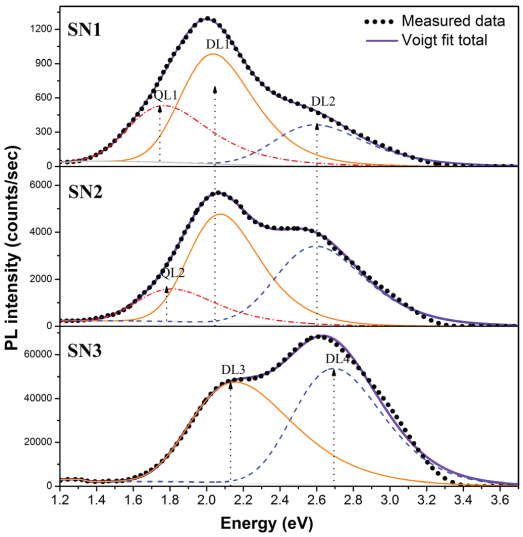

FIG. 8. PL spectra acquired from the three annealed samples at room temperature. Different peak components are resolved by fitting using the Voigt functional form. Arrows indicate emission bands corresponding to defect levels (DL) and quantum level (QL) in Table III.

TABLE III. Component peaks of the PL spectra of the three annealed samples and their respective energies and contributions.

Sample	Peak name	Peak energy (eV)	Peak contribution (%)
SN1	QL1	1.76	37
	DL1	2.03	49
	DL2	2.54	14
SN2	QL2	1.79	21
	DL1	2.04	50
	DL2	2.59	29
SN3	DL3	2.16	60
	DL4	2.69	40

(47% compared to 9%). On the other hand, a more intense luminescence of QL2 band was observed in sample SN2. The difference in PL intensities of QL1 and QL2 can be explained by: (i) the NC size dependence of recombination probabilities, (ii) different quenching probability by defects at/or near the NC interfaces, caused by different lifetime in the NCs, and (iii) different concentration of defects. These mechanisms can contribute to the observed different intensities of QL1 and QL2. Naturally, the absence of any red emission band in sample SN3 is consistent with the lack of Si NCs in this sample.

Concerning the yellow to orange emission, the 2 eV bands dominate the PL spectra of sample SN1 and SN2 with relative contributions of about 50% in both cases (DL1 in Figure 8 and Table III), whereas another band at 2.16 eV governs the PL spectra of sample SN3 with a relative contribution of 60% (DL3 in Figure 8 and Table III). We tentatively assign DL1 and DL3 bands to the same type of defect level transitions, but in different matrices due to the different O content in the samples. The energy gaps of states of the systems are schematically drawn in Figure 9. According to the theoretical calculations of Robertson and Powell,[23] emission bands observed at 2.1 eV are caused by the electronic transitions from the conduction band minimum of Si_3N_4 to Si dangling bond states denoted $\equiv Si^0$. Hence, our observed orange emission bands at 2 eV (DL1) and 2.16 eV (DL3) could have a similar origin. The slightly higher energy of DL3 band in sample SN3 may be associated with the higher O content and be explained as follows: Ance *et al.*[24] reported that for the SiO_xN_y films, which are assumed to have a random mixture of Si–N and Si–O, the bottom of the conduction band shifts to higher energy while the valence band maximum does not change. Thus, the optical gap opens with increasing oxygen content, as compared to the original band gap of Si_3N_4. According to these observations, sample SN3, which has a relative oxygen ratio $O/(O+N) = 0.5$, is thus expected to have a larger band gap than samples SN1 and SN2. Therefore, the electronic transitions from the conduction band minimum to $\equiv Si^0$ in sample SN3 should give a higher energy of the emission band compared to that of samples SN1 and SN2. The band gap of Si_3N_4 in sample SN1 and SN2, which have a similar ratio of $O/(O+N) = 0.2$, will remain constant. In addition, rationalizing from the theoretical analysis of Robertson and Powell,[23] the optical bangap is essentially made of σ^* antibonding Si orbitals and σ bonding Si orbitals near the conduction and valence band, respectively. The Si atoms are tetrahedrally bonded and use their four sp^3 hybrids for bonding both in Si_3N_4 and in crystalline Si. The mid-gap dangling bond state $\equiv Si^0$ is tied to these Si orbitals, so when the bandgap of sample SN3 increases the mid-gap position will also rise. Therefore, the position of the $\equiv Si^0$ gap state in sample SN3 will be shifted upward, as shown in Figure 9.

For the three annealed samples, the spectral position of the blue emission band (DL2 and DL4 in Figures 8 and 9) remains centered at around 2.6 eV, even though for sample SN3 the DL4 band exhibits a slight blue shift and an increase in its FWHM (Figure 8). This is likely due to the large increase of the total O content in sample SN3 evidenced by the XPS results. Figure 10 summarizes the observed trends for the blue band position and its contribution to the PL

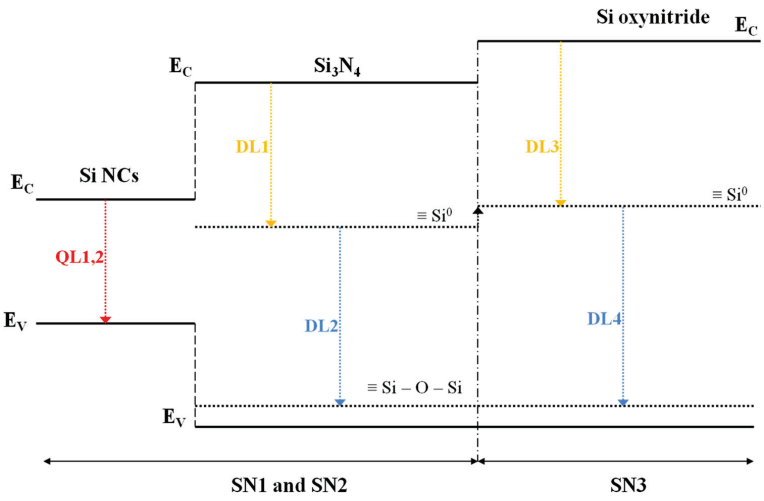

FIG. 9. Gap states including DL and QL and corresponding electronic transitions observed in the three annealed samples.

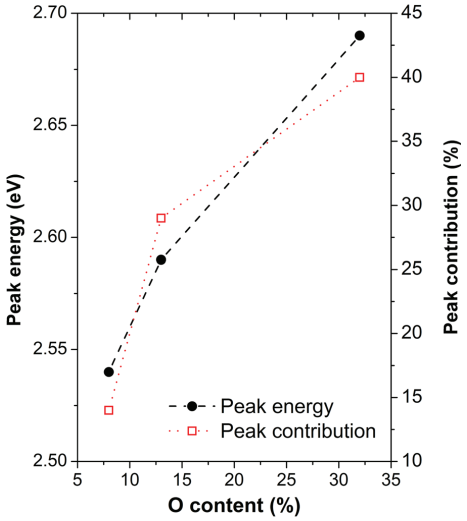

FIG. 10. Energy shifts and peak contributions of blue emission bands (DL2 and DL4) as a function of O content in the three annealed samples.

spectra as a function of the O content in the three annealed samples. Huang *et al.*[11] reported that the blue emission peak at around 2.5 eV in amorphous Si nitride films that have been oxidized originates from localized states related to Si–O bonds. Its intensity was shown to be strongly dependent on the Si–O bonds concentration. Furthermore, Liu *et al.*[25] reported that the presence of O in SRN films will create a gap state of Si–O above the valence band maximum of Si_3N_4 and will lead to the $\equiv Si^0 \rightarrow \equiv Si–O–Si$ transition, giving rise to the 2.55 eV emission.[25] In our experiment, the emission band at 2.54–2.59 eV (DL2 in Figures 8 and 9 and in Table III) observed in sample SN1 and SN2 is compatible with this model. Meanwhile, we suggest that the 2.69 eV emission band (DL4 in Figures 8 and 9 and in Table III) in sample SN3 originates from the same source, with a slightly higher energy compared to DL2 band due to the higher energy position of the $\equiv Si^0$ gap state in this sample compared to the others as previously discussed. With increasing O concentration from 8 to 40%, the contribution of these emission bands increases gradually from 14 to 40% (see Figure 10). The emission intensity is directly proportional to the state density. Therefore, the increase of the height of the blue emission band with increasing O content can be attributed to the rise of localized state density related to Si–O bonds in the matrix.

In summary, the dominant orange to yellow emission in the PL of the three annealed samples stems from the electronic transitions from the conduction band minimum of silicon nitride to $\equiv Si^0$ (50%–60%), whereas the contribution from the blue emission related to the gap state of Si–O bonds increases with O content in the corresponding sample. In addition, for sample SN1 and SN2 where Si NCs were found, the association of the red band to the light emission arises from band-to-band radiative recombination in the Si NCs, while this is absent in sample SN3 where no NCs were found.

C. Summarizing discussion of the sample structures and mechanisms

Complementary TEM, XPS, EELS, and PL results have allowed us to draw a consistent picture of bonding structures and resulting optical properties in our Si nitride films. By XPS quantification profiles and EELS line scans through the film depth, we observed that, overall, the O concentration follows the nitride content. Upon closer inspection, however, oxygen is detected mostly at the top film surface and the Si nitride buffer layers. The oxide surface is thought to be due to sample surface oxidation, while the Si nitride buffer layer has a strong tendency to create oxy-nitride owing to its porous structure, which has been observed by HRTEM and HAADF STEM. Concerning the SRN layers, sample SN3 takes up a large amount of O in its bulk due to its high nitride concentration and therefore high density of pores. As a result, more Si–O bonds are formed. The annealed film structure is then described adequately by the RBM and consists in bonded networks of randomly distributed tetrahedral SiO_xN_{4-x} (where $x = 0, 1, 2, 3,$ and 4). The oxy-nitride film will not induce large scale potential fluctuations as no spatial local variation of dielectric constant exists in the randomly distributed oxy-nitride tetrahedra. Consequently, no excited carriers' confinement and recombination is expected in the PL. This is in good agreement with the observed PL of sample SN3 where the dominant emission band is thought to arise from defect levels in the amorphous matrix. An additional effect of the high O content in this structure is to shift the conduction band minimum to higher energy, giving rise to a defect-related emission band at a higher energy than in the pure nitride.

Samples SN1 and SN2 have a low O concentration, and these film bonding structures cannot be explained by either the RBM or the RMM. Except for the difference in crystalline Si content, the matrices of these annealed film structures are quite similar, dominated by a Si_3N_4 phase with occasional localized nanoregions of the Si_2ON_2 phase (the latter are very rare in SN1 and more numerous is SN2 due to its higher O content overall). Consequently, the optical gap of the matrix remains similar to that of the Si_3N_4 phase. The PL observed in these films thus originates from the same mechanism, including the band-to-band radiative recombination in the Si NCs, the radiative recombination via luminescent Si dangling bonds and Si–O bonds existing in the matrix. The intermediate model is found to be satisfactory to describe these film structures, where Si clusters, Si_3N_4, and Si_2ON_2 phase coexistence can cause variations in local chemical composition and as such can lead to the potential fluctuation in Si_3N_4. Therefore, this material is capable of localizing electrons and holes in potential wells, giving rise to the quantum confinement effect of Si NCs, as experimentally observed in the PL of sample SN1 and SN2.

IV. CONCLUSIONS

We combined different techniques including XPS, HRTEM, STEM-EELS and PL spectroscopy to study the

structure, chemical bonding, and optical properties of sputtered silicon nitride thin films of variable compositions. It is found that after annealing at 1100 °C for 2 h, Si NCs were formed in highly Si-rich silicon nitride (~50 at. %–60 at. % Si), and the crystal size and density strongly depend on the amount of excess Si. For films with a smaller Si concentration (less than ~40 at. % of Si) no Si NCs were formed in the nitride matrix while the film structure remained amorphous. We were able to correlate the nitride content in different samples and the degree of O incorporation into the nitride network due to its porous structure. Different chemical bond distribution models were used to describe the film structures.

The SRN films with low O content can be best described by the intermediate model, according to which the SiO_xN_y films comprise five types of tetrahedral units, as in the RBM, but for which the probability of finding a given tetrahedron type is not described by the RBM. On the other hand, a high level of O incorporation into the silicon nitride network results in a structure that is well described by the RBM. These theoretical models were justified experimentally by our XPS and EELS results. This information about the specific atomic structure and bonding characteristics in these SiO_xN_y nitride films provides us with key knowledge to clarify the roles of Si NCs and defects in the PL.

A model of gap states and electronic transitions for the SiO_xN_y films is proposed, according to which the dominant emission in the PL arises from the radiative Si dangling bond centers in the silicon nitride matrix, whereas the contribution from the emission band related to the gap state of Si–O bonds increases with O content. In addition, for samples where Si NCs have been found, the association of the emission band arising from band-to-band recombination in the Si NCs is proportional to the concentration of crystals in these samples. Our study also shows that in order to obtain desirable physical properties of silicon nitride thin films produced by sputtering, a precise adjustment of the deposition parameters is needed, making the produced films more reliable for practical applications.

ACKNOWLEDGMENTS

The authors would like to thank the University of Oslo for financial support. The SuperSTEM Laboratory is funded by the U.K. Engineering and Physical Sciences Research Council (EPSRC). P. D. Nguyen wishes to thank O. B. Karlsen for useful discussions and for assistance with sample preparation.

[1]L. Pavesi and R. Turan, *Silicon Nanocrystals* (Wiley-VCH Verlag GmbH & Co. KGaA, 2010), p. 1.
[2]L. D. Dal Negro, S. Hamel, N. Zaitseva, J. H. Yi, A. Williamson, M. Stolfi, J. Michel, G. Galli, and L. C. Kimerling, Sel. Top. Quantum Electron. IEEE J. **12**, 1151 (2006).
[3]S. Minissale, S. Yerci, and L. D. Negro, Appl. Phys. Lett. **100**, 021109 (2012).
[4]G. Conibeer, I. Perez-Wurfl, X. Hao, D. Di, and D. Lin, Nanoscale Res. Lett. **7**, 193 (2012).
[5]B.-H. Kim, C.-H. Cho, T.-W. Kim, N.-M. Park, G. Y. Sung, and S.-J. Park, Appl. Phys. Lett. **86**, 091908 (2005).
[6]M. Wang, D. Li, Z. Yuan, D. Yang, and D. Que, Appl. Phys. Lett. **90**, 131903 (2007).
[7]R. Guerra, M. Ippolito, S. Meloni, and S. Ossicini, Appl. Phys. Lett. **100**, 181905 (2012).
[8]J. Kistner, X. Chen, Y. Weng, H. P. Strunk, M. B. Schubert, and J. H. Werner, J. Appl. Phys. **110**, 023520 (2011).
[9]M. Martyniuk, J. Antoszewski, C. A. Musca, J. M. Dell, and L. Faraone, J. Appl. Phys. **99**, 053519 (2006).
[10]W.-S. Liao, C.-H. Lin, and S.-C. Lee, Appl. Phys. Lett. **65**, 2229 (1994).
[11]R. Huang, K. Chen, B. Qian, S. Chen, W. Li, J. Xu, Z. Ma, and X. Huang, Appl. Phys. Lett. **89**, 221120 (2006).
[12]V. A. Gritsenko, J. B. Xu, R. W. M. Kwok, Y. H. Ng, and I. H. Wilson, Phys. Rev. Lett. **81**, 1054 (1998).
[13]V. Gritsenko and H. Wong, Crit. Rev. Solid State Mater. Sci. **36**, 129 (2011).
[14]P. D. Nguyen, D. M. Kepaptsoglou, Q. M. Ramasse, and A. Olsen, Phys. Rev. B **85**, 085315 (2012).
[15]P. Cova, S. Poulin, O. Grenier, and R. A. Masut, J. Appl. Phys. **97**, 073518 (2005).
[16]V. Gritsenko, D. Gritsenko, Y. Novikov, R. Kwok, and I. Bello, J. Exp. Theor. Phys. **98**, 760 (2004).
[17]V. A. Gritsenko, R. W. M. Kwok, H. Wong, and J. B. Xu, J. Non-Cryst. Solids **297**, 96 (2002).
[18]Y. N. Novikov and V. A. Gritsenko, J. Appl. Phys. **110**, 014107 (2011).
[19]K. Sader, B. Schaffer, G. Vaughan, R. Brydson, A. Brown, and A. Bleloch, Ultramicroscopy **110**, 998 (2010).
[20]W.-Y. Ching, S.-D. Mo, and Y. Chen, J. Am. Ceram. Soc. **85**, 11 (2002).
[21]T.-Y. Kim, N.-M. Park, K.-H. Kim, G. Y. Sung, Y.-W. Ok, T.-Y. Seong, and C.-J. Choi, Appl. Phys. Lett. **85**, 5355 (2004).
[22]T.-W. Kim, C.-H. Cho, B.-H. Kim, and S.-J. Park, Appl. Phys. Lett. **88**, 123102 (2006).
[23]J. Robertson and M. J. Powell, Appl. Phys. Lett. **44**, 415 (1984).
[24]C. Ance, F. D. Chelle, J. P. Ferraton, G. Leveque, P. Ordejon, and F. Yndurain, Appl. Phys. Lett. **60**, 1399 (1992).
[25]Y. Liu, Y. Zhou, W. Shi, L. Zhao, B. Sun, and T. Ye, Mater. Lett. **58**, 2397 (2004).

Paper III

P. D. Nguyen, D. M. Kepaptsoglou, R. Erni, Q. M. Ramasse, and A. Olsen

Quantum confinement of volume plasmons and interband transitions in germanium nanocrystals

Physical Review B 86, 245316 (2012)

Quantum confinement of volume plasmons and interband transitions in germanium nanocrystals

P. D. Nguyen,[1,*] D. M. Kepaptsoglou,[2] R. Erni,[3] Q. M. Ramasse,[2] and A. Olsen[1]
[1]*Department of Physics, University of Oslo, P.O. Box 1048, Blindern, NO-0316 Oslo, Norway*
[2]*SuperSTEM Laboratory, STFC Daresbury Campus, WA4 4AD Warrington, Cheshire, United Kingdom*
[3]*Electron Microscopy Center, Empa, Swiss Federal Laboratories for Materials Science and Technology, CH-8600 Dübendorf, Switzerland*
(Received 2 October 2012; published 17 December 2012)

The plasmonic properties of individual quantum-sized Ge nanocrystals (NCs) were observed and systematically analyzed by aberration-corrected scanning transmission electron microscopy (STEM) and electron energy loss spectroscopy (EELS). For this purpose, Ge NCs embedded in an SiO_2 matrix with controllable size, density, and structure were fabricated using magnetron sputtering. The size dependence of the Ge plasmon energies in the size range of 5–9 nm is shown to be well depicted by the so-called medium quantum confinement (QC) model, with an effective mass of $0.57m_0$ (contrary to expectations of a stronger quantum effect). In the very low-loss region of the EEL spectra, an apparent blue shift of the E_2 interband transition peak up to 2 eV and a strong reduction in the oscillator strength were measured for the NCs in the size range of 4–6 nm. It indicates for this smaller size range a transition to a QC regime where the band structure and the density of states are modified dramatically. These trends are explained by a combination of low-loss and core-loss EELS results, which show that the Ge NCs are surrounded uniformly by nearly stoichiometric SiO_2. This local chemistry is shown to provide an infinite potential barrier and to confine electrons and holes in the spherically shaped Ge NCs. In addition to pure QC effects in the Ge NCs, the SiO_2 matrix thus plays an important role in the strength of the observed QC and interband transitions.

DOI: 10.1103/PhysRevB.86.245316 PACS number(s): 73.22.−f, 73.21.La, 73.63.Bd

I. INTRODUCTION

Ge and Si nanocrystals (NCs) embedded in dielectric matrices such as SiO_2 have attracted a great deal of attention due to their tailorable electronic and optical properties for a wide range of optoelectronic and solar cell applications.[1] It is well demonstrated that the electronic structure of the valence band and the conduction band are strongly modified in these NCs.[2,3] For example, by engineering the sizes and morphologies of Si and Ge nanostructures, a widening of effective band gaps and an efficient interband absorption over a certain spectrum range can be obtained.[4] Therefore, in order to tailor these systems for optoelectronic applications, it is extremely important to understand how their properties evolve as a function of NC size and structure.

If the "particle in a box" model is applied to the aforementioned systems, one would expect the band gap to increase and the characteristic transition energies, such as excitons, to move to higher energies due to the quantum confinement (QC) effects in the confined directions.[5] The consequences of these effects have been studied extensively by a variety of techniques, including theoretical calculations,[3,5,6] a combination of low-loss and core-loss STEM-EELS,[7–9] and x-ray absorption spectroscopy (XAS).[10] More complicated quantum behaviors of different interband transitions away from the Brillouin zone center of Ge atomic-like discrete structures, which cannot be described completely by the "particle in a box" model, have also been studied through optical absorption, Raman scattering, and ellipsometry.[11,12] Although these optical methods are commonly used to characterize the optoelectronic properties of such systems, the quantitative information they collectively yield is difficult to interpret due to several factors contributing to the uncertainty of experimental results: size dispersion of NCs, different shapes, density, and interface structures of NCs as well as electron, photon, and phonon transfer between NCs. Consequently, there have been many apparently conflicting reports on these systems. For instance, Tognini *et al.*[11] reported absorption spectra from Ge NCs showing a blue shift of the E_2 transition, which occurs near the X point of the Brillouin zone, and a weakening of the E_1 transition, which is along the Λ direction, with decreasing Ge NC size. By contrast, Heath *et al.*[12] studied extinction spectra from Ge NCs and suggested that E_1 and E_2 remain unaffected by QC. Finally, Melnikov and Chelikowsky[13] calculated absorption spectra of Ge NCs using *ab initio* calculations and showed that both E_1 and E_2 energies are expected to blue shift owing to QC. The discrepancies between the reported experimental results and theoretical calculations demand further investigation in order to predict more accurately the quantum behaviors of these transitions.

One of the most important factors for consideration, when studying QC effects experimentally, is the spread in NC sizes in the samples, which can lead to uncertainties in exciton line positions and widths.[10] Among the variety of available experimental techniques, aberration corrected STEM-EELS is particularly suited to probing the local electronic structure and elemental distribution inside the individual NCs and their surrounding matrices thanks to its key advantage of very high combined spatial and energy resolutions.[14] The low-loss part of the EELS spectrum provides inherent information about plasmon densities and band structures of semiconducting and insulating materials.[15] In addition, the energy-loss near edge structure (ELNES) in core-loss EELS reflects the local density of empty states above the Fermi level, which provides information about the chemistry and bonding of the material under investigation.[16] In the present paper we combine experimental low-loss and core-loss STEM-EELS to study a number of phenomena related to QC in individual Ge NCs embedded in an SiO_2 matrix. The observed phenomena include an apparent blue shift in plasmon energies and an enhancement

of Ge interband transitions with decreasing NC size. In order to facilitate the interpretation of the experimental results, theoretical simulations have also been carried out for similar confined nanostructures to predict possible behaviors of the excitations in the low-loss EELS and thus provide a clearer physical understanding. In addition to the quantum size effects, chemical states and electronic properties of the SiO_2 matrix as well as effects due to changes in the Ge crystal structure are also investigated and discussed.

II. EXPERIMENT

A four-layer structure thin film composed of an SiO_2 buffer layer followed by two SiGeO middle layers with different Ge contents and a capping SiO_2 layer was deposited on a (100)-oriented single-crystal Si substrate by radio frequency (rf) magnetron sputtering in Ar atmosphere. These layers will be hereafter named as layers 1, 2, 3, and 4 for simplicity. Prior to sputtering, the chamber was evacuated to 5×10^{-7} mbar. During the film deposition the Ar pressure in the chamber was kept at 1×10^{-3} mbar. Layers 2 and 3 of SiGeO were obtained by co-sputtering and deposition from SiO_2 and Ge targets without any intentional substrate heating. The different Ge content between these layers was achieved by adjusting the sputtering rate for the Ge target, while the sputtering rate for the SiO_2 target was kept constant. With the purpose of forming Ge NCs in the oxide matrix, the sample was subsequently annealed at 800 °C for 1 h in a sealed SiO_2 glass tube evacuated to a vacuum of better than 1×10^{-2} mbar. High-resolution transmission electron microscopy (HRTEM) observations were performed at 200 keV primary beam energy with a JEOL 2010F microscope. The STEM-EELS experiments were performed at 60 keV in a C_s-corrected Nion UltraSTEM[17] equipped with a Gatan Enfina spectrometer. The cold field electron emitter of this instrument has a native energy spread of 0.35 eV, as determined from the full width at half maximum of the zero-loss peak in typical operating conditions. The EELS experiments were carried out with a probe size of 1.1 Å, the collection semiangle was 4 mrad for the low-loss data sets and 32 mrad for the core-loss data sets. The probe convergence semiangle was 30 mrad. Both 2D-EELS spectrum imaging and distributed-dose "SMART EELS"[18] line-scan techniques were employed. The latter was used in order to mitigate the effects of radiation damage and contamination by distributing the electron dose received by individual NCs. Postmortem images were systematically acquired in order to check for possible specimen drift during the data collection and to assess specimen beam damage.

III. RESULTS AND DISCUSSION

A. Structural and chemical characterization

HRTEM imaging and electron diffraction confirmed the formation of Ge NCs in both layers 2 and 3. As shown in Fig. 1, layer 2 has a higher density and bigger grain size of Ge NCs (5–10 nm) than layer 3 (2–5 nm). For both layers, the NCs are nearly spherical in shape and uniformly distributed in the bulk of these layers. The results of quantitative energy dispersive x-ray spectroscopy analysis showed that the concentration of elemental Ge in layers 2 and 3 are 40% and 12%, respectively.

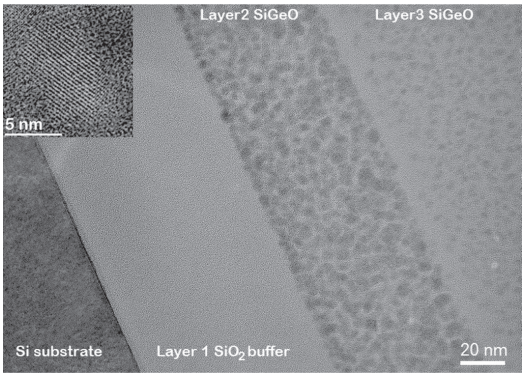

FIG. 1. HRTEM image of the three layers: layer 2 has a higher density and bigger grain size of Ge NCs (5–10 nm) than layer 3 (3–5 nm). The inset shows clear lattice fringes of a Ge NC in layer 2.

Some of the NCs, which precipitated densely in layer 2, are interconnected and/or formed twinning defects, while all of the NCs in layer 3 are well separated and defect-free. In addition, for layer 3 the lattice fringes inside the NCs and the interfaces between them and the matrix were not resolved in the HRTEM images as clearly as those in layer 2. Especially the particles with sizes ∼2 nm in layer 3 were found to be amorphous, which is in good agreement with XAS results reported by Araujo *et al.*[19] on Ge NCs implanted in an SiO_2 matrix, and molecular-dynamics results for Ge NCs embedded in an amorphous matrix reported by Bording and Taftø.[20]

It is well known that the optical properties of Si and Ge NCs are strongly affected by the structural and chemical properties of their surfaces since NCs have a high surface to volume ratio.[21] The interface between a NC and its surrounding matrix can play a crucial role in the optoelectronic properties of the NCs.[22,23] By analyzing the Si $L_{2,3}$ edge from the core-loss EELS line scans across the surrounding matrix to the NC core, useful information about the local bonding, defect, and chemical state at the site where the atom is being excited can be obtained. Figure 2(a) shows the HAADF STEM survey image of a Ge particle in layer 2 where the trace of a core-loss EELS line scan taken across the particle is marked from A to D. Figure 2(b) shows background-subtracted, averaged EELS spectra of the Si $L_{2,3}$ edge (each spectrum in this figure is an average of 20 adjacent spectra) from the four probe positions indicated in Fig. 2(a). The spectra correspond to the areas marked A to D in Fig. 2(a). Compared to the Si $L_{2,3}$ edge of stoichiometric SiO_2 reported by Erni *et al.*,[16] the four spectra show similar peak energies and ELNES. It is expected that the suboxides (Si^{1+}, Si^{2+}, and Si^{3+}) should show a broad intensity band in front of the Si $L_{2,3}$ edge.[16,24–26] As seen in Fig. 2(b), no extra intensity in the pre-edge region is observed. The only difference is found in the intensities of the edges, which are as expected higher in the matrix than in the NC core. Therefore the Ge NCs appear to be surrounded uniformly by nearly stoichiometric SiO_2, and if there is any chemical modification in the matrix [e.g., O deficiency, coexistence of $(SiO_2)_x(GeO_2)_y\ldots$], the concentration of any secondary phases must be too low to be detected at the Si $L_{2,3}$ edges.

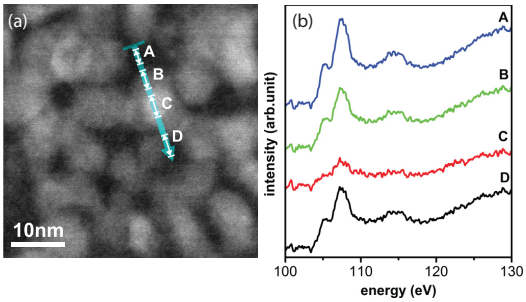

FIG. 2. (Color online) (a) HAADF STEM survey image of a Ge particle in layer 2 where the trace of core-loss EELS line scans taken across the particle is marked from A to D. (b) Background-subtracted, averaged EELS spectra of the Si $L_{2,3}$ edge from the four probe positions indicated in (a). The spectra correspond to the areas marked A to D in (a), respectively.

A similar behavior was observed for the averaged core-loss EELS line scans across the film structure from layer 1 to 3, at both Si $L_{2,3}$ and O K edges. The intensities of these edges are highest in layer 1 of pure SiO_2 and lowest in layer 2 where Ge NCs precipitated densely. The fact that the similar shape and sharp features of the Si $L_{2,3}$ edge can be observed in the three layers indicates that the suboxide content is negligible and the chemical structure of the matrix, which is stoichiometric SiO_2, is independent of the Ge content in layers 2 and 3. This information is essential for deconvoluting the contribution of the matrix in the low-loss EELS data that will be discussed in the following section of this paper.

B. Experimental and calculated low-loss EELS

The controllable sizes, spatial distributions, and structures of Ge NCs in layers 2 and 3 allow us to study the size-dependent volume plasmon and interband transition energies of individual NCs in a large range of sizes with different crystal densities and structures under the same experimental conditions. Due to the radiation damage sensitivity of the Ge-SiO_2 system and in order to improve the signal to noise ratio, the distributed-dose SMART EELS acquisition technique was employed for low-loss EELS. The typical setting of SMART acquisitions is shown in Fig. 3(a), where the HAADF image is marked with the trace of the line scan taken across a Ge NC in layer 2, while the dose is distributed by displacing the probe along the other direction at each point in the line scan, as indicated. Figure 3(b) shows zero-loss peak subtracted (using a power-law function), averaged plasmon EELS spectra from the line scan in Fig. 3(a). Each spectrum in Fig. 3(b) is an average of 20 adjacent spectra (of a line scan containing a total of 150 spectra). The spectra correspond to the areas marked A to C in Fig. 3(a), respectively. Moving from the matrix to the NC core, the plasmon peak shifts to lower energy. The plasmon response of this heterostructure is expected to contain contributions from both the Ge NCs and the surrounding SiO_2 matrix. Therefore, a deconvolution of these broad plasmon peaks is needed in order to identify the individual constituents.[9] By using the Voigt functional-form fitting method, different component peaks are resolved for spectrum B taken at the NC core as shown in Fig. 3(c). The two main components under the plasmon peak were assigned to the volume plasmons of the Ge NC and SiO_2, matrix respectively. The position of the SiO_2 matrix plasmon was verified independently by acquisition of low-loss EEL spectra from the matrix immediately surrounding each studied NC. The plasmon energy of the matrix was found to be in the range of 23–24 eV. This is in agreement with the core-loss EELS results, which showed that the matrix composition is uniform and is nearly stoichiometric SiO_2. The remaining components correspond to the broad $M_{4,5}$ ionization edge of Ge NCs at around 29 eV[27] and a broad peak with maximum around 6 eV. This peak, seen only in spectra acquired in layer 2 (Fig. 3) and layer 3 (not shown), could have several origins, including interband transitions from Ge NCs, retardation effects, such as Čerenkov radiation and guided light modes, or interface plasmon excitation between Ge NCs and the SiO_2 matrix.

In order to determine the origin of the low-loss peak at 6 eV we performed low-loss EELS calculations for a simplified sandwich structure of SiO_2/Ge/SiO_2 as well as for amorphous SiO_2 and Ge of varying thickness, for conditions that reflect

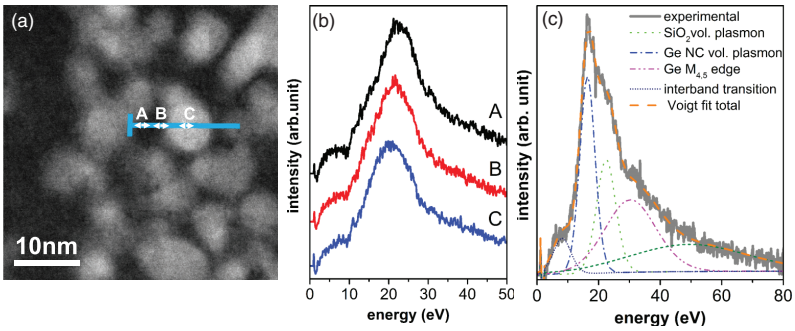

FIG. 3. (Color online) (a) Typical setting of EELS SMART acquisitions for the low-loss line scan, where the HAADF image is marked with the trace of the line scan taken across the Ge NC. (b) Zero-loss peak subtracted, averaged plasmon EELS spectra from the line scan in (a). The spectra correspond to the areas marked A to C in (a), respectively. (c) Different component peaks are resolved for spectrum C taken at the NC core by using the Voigt functional-form fitting method.

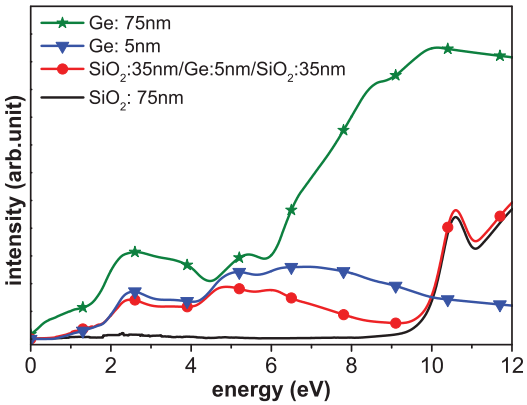

FIG. 4. (Color online) Calculated low-loss EELS spectra at 60 kV for four systems: 75 nm of SiO_2, 75 nm of Ge, 5 nm of Ge, and (35 nm SiO_2 / 5 nm Ge / 35 nm SiO_2). For the last three systems, the interband transition ∼2.5 and 5 eV is well described.

the experimental setup. In these simulations, we use the Ge and SiO_2 bulk dielectric functions,[28] and apply the dispersion bracket formalism of Bolton and Chen[29,30] which allows for calculating surface/interface and bulk plasmons as well as (relativistic) radiation losses. QC effects are not included as they would require corresponding dielectric data.[31,32] The calculations show that the very low-loss regions (0–10 eV) of the EELS spectra from the Ge and SiO_2/Ge/SiO_2 systems are dominated by interband transitions at ∼2.5 and 4.8 eV originating from the thin Ge layers (Fig. 4). These features, which are present in the calculated spectra of a pure Ge slab of thickness 75 and 5 nm, respectively (green and dark blue curves), as well as in the spectrum of the sandwich structure of a 5 nm thick Ge slab embedded in 70 nm amorphous SiO_2 (red curve), closely resemble the E_1 (2.3 eV) and E_2 (4.4 eV) transitions reported in bulk Ge.[33,34] No interface plasmons between SiO_2 and Ge thin layers were predicted by the simulation, implying that there is no strong coupling of the dielectric functions. The fact that the features and intensities of the peak around 6 eV observed experimentally in our spectra do not vary as the beam moves from the particle core to the matrix/particle interface further confirms that these features are not likely related to the interface plasmons. Hence, the experimental data can be interpreted in terms of a superposition of a spectrum that is due to the SiO_2 matrix and another part that is due to the Ge NCs. Moreover, there are no significant peaks present in the calculated spectra that are due to retardation effects such as Čerenkov losses or losses due to the excitation of guided light modes. Indeed, the absence of significant radiation losses can be expected at a primary electron energy of 60 keV. Yet, what cannot be completely ruled out is that residual radiation damage leads to the creation of electronically active defects in SiO_2 that could contribute to the absorption in the sub-10 eV energy range.[35–37] However, as the spectrum recorded from amorphous SiO_2 does not show significant intensity in the sub-10 eV range, the overall effect of residual radiation damage must be small. Therefore, the experimental spectra reflect the actual dielectric characteristics of the material (the interband transitions from Ge NCs) rather than the interaction with the matrix or electron beam. It is therefore concluded that the peak observed at 6 eV peak more likely corresponds to the E_2 interband transition, blue shifted with respect to its bulk value.

C. Quantum confinement of E_2 interband transition

The E_1 transitions (∼2.3 eV) were not observed in our experimental low-loss EELS spectra, possibly due to the weakening of these transitions with the NC size reduction due to a transfer of oscillator strength from E_1 to E_2 transition[11] and the potential overlap with the tail of the zero-loss peaks. Furthermore, Guerra *et al.*[38] reported density functional theory (DFT) calculations on the absorption spectra of Si NCs embedded in SiO_2 matrix and suggested that the absorption at low energy (<4 eV) is strongly damped due to the screening induced by polarization effects at the NC interfaces. Therefore, it can be expected that the E_1 transition features tend to vanish in the presence of local field effects at the NC interfaces.

As discussed above, the 6 eV peak can be assigned to the E_2 interband transition, which is one of the most dominant absorption peaks in the visible region reported in the literature.[11,33,34,39] Figure 5(b) shows the evolution of the E_2 peak position with NC size, as determined by the zero crossing of the first derivative of the low-loss spectrum[11,33,39] [Fig. 5(a)]. The E_2 peaks show a very strong size dependence in the size range of ∼4–6 nm. Radiation damage in the very small NCs does not permit a more detailed study of the behavior of this transition in the size range lower than ∼4 nm. When the NC size decreases from 6 to 4 nm, a dramatic blue shift of the E_2 peak by ∼2 eV is observed, in addition to a depression of its features. A similar behavior of this transition in optical extinction spectra was reported by Hayashi *et al.*[34] for sputtered Ge NCs embedded in SiO_2 thin films, who suggested that for small Ge NCs (∼2.7 to 4.2 nm) the whole band structure and the density of states are altered dramatically.

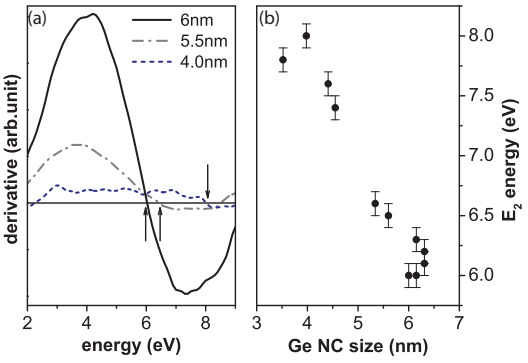

FIG. 5. (Color online) (a) First derivative of E_2 transition peaks of Ge NCs with different sizes. The zero crossing of the curves determines the shift of E_2 peaks. (b) The blue shift of E_2 transitions with decreased NC size.

Compared to the shift of the E_2 transition obtained by *ab initio* calculations of the absorption spectra for hydrogenated Ge NCs reported by Melnikov *et al.*,[13] our data show a higher shift. This might be attributable to the propensity of local density approximation calculations to underestimate the energy of the E_2 transition.[13] A smaller shift is also found for the optical absorption data measured from Ge NCs confined in Al_2O_3/Ge multilayer structures by Bottani *et al.*,[39] or from Ge NCs embedded in SiO_2 by Hayashi *et al.*,[34] albeit with the same trend of size dependence. This can be expected since optical absorption data are acquired with a broader beam over an average of NC size distributions, while our EELS data are obtained directly from individual NCs by using a very small probe size (~1.1 Å). The impact of using different dielectric matrices and growth methods on the observed quantum size effects is also very important in the interactions between NCs and matrices, interface structures, induced stress, and local field effects.[6,38,40,41] As shown by DFT calculations on the absorption spectra of Si NCs embedded in SiO_2 matrix by Guerra *et al.*[38] local field effects cause a blue shift of the main absorption peak (~5.5 eV), in particular for small NCs, which show a sensitivity to their surrounding environment related to perturbations of the absorption resonance conditions. Therefore, we suggest that the higher blue shift of the E_2 transition observed in our experiments as compared to other reported data[13,39] can be attributed to the contribution of local field effects at the interfaces between Ge NCs and the SiO_2 matrix. Crucially, this enhancement of interband absorption with the reduction of Ge NC sizes and the variations of this absorption with the crystal quality suggest a practical way of tuning the efficiency of interband absorptions over certain spectral ranges.

D. Quantum confinement of volume plasmon energy

Depending on the Bohr radius (a_B) and the NC diameter (d), three regimes of QC can be defined by the effective-mass approximation (EMA):[5,6] weak, medium, and strong confinement (for more details, refer to Refs. 5 and 6). For Ge, a_B is ~24 nm, which means that for the size range of Ge NCs in this work (~2–10 nm) the strong confinement regime would be expected. Moreover, the blue shift of the plasmon energies E_P with decreasing particle diameter is attributed to the quantum size effect of the band gap that affects the plasmon energy through the oscillator strength as described by Mitome *et al.*[42] Experimental EELS data of Si NCs and Ge nanowires have revealed trends of $E_P \propto 1/d^2$ and $E_P \propto 1/d^{1.2}$, respectively.[8,9,42] Under the same experimental conditions, Si and Ge NCs with similar structure and geometry embedded in a dielectric matrix can be expected to follow the same trend of $E_P \propto 1/d^2$. The size dependence of plasmon energies for Ge NCs (Fig. 6) is plotted against theoretically predicted trends in three different regimes: strong, medium, and weak confinement. The theoretical QC curves follow the $E_P \propto 1/\mu.d^2$ relation, where μ is the effective mass of the electron-hole pair in each of these three QC regimes.[5,42] Overlaying our experimental data points with the theoretical curves, it appears that the strong regime predicted for the NC sizes considered here overestimates the QC effects observed experimentally. The experimental data show instead

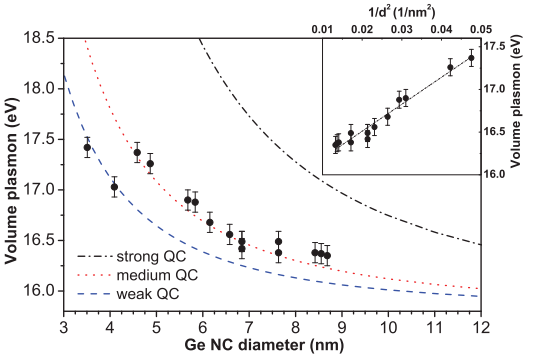

FIG. 6. (Color online) NC size dependence of the Ge volume plasmon energy. The dotted-dashed, dotted, and dashed curves show the theoretically predicted $E_P \propto 1/d^2$ relationship in three different regimes: strong, medium, and weak, respectively. The inset shows the data fitting for NCs > 4 nm.

that most of the NCs in layer 2 (>4 nm) follow closely the medium confinement curve and are best fitted by the equation $E_P = 31.58/d^2 + 15.87$ (see the inset in Fig. 6), which gives an estimated effective mass $\mu = 0.57m_0$, where m_0 is the electron rest mass, consistent indeed with a medium confinement model. By contrast, the NCs in layer 3 (<4 nm) appear to follow the weak confinement curve, although fewer data points are available. The error bars indicate the accuracy in determining the plasmon shift, which was verified statistically from experiments and the instrument resolution.

While neither case appears to follow the initial theoretical expectation of strong confinement behavior, the observed medium confinement trend for the Ge NCs > 4 nm is in fact in good agreement with the experimental EELS results reported by Mitome *et al.*[42] for freestanding Si NCs. They also agree with the effective mass theoretical models calculated by Barbagiovanni *et al.*[6] for Si and Ge NCs embedded in an SiO_2 matrix. The latter were further confirmed by photoluminescence[43] and XAS[10] data.

It is of interest to compare the strength of QC effects in the valence band of Ge NCs and of a similar system consisting of Si NCs, as observed through the blue shift of plasmon energies. We recently reported a strong QC in Si NCs embedded in a silicon nitride matrix,[9] far stronger than the present Ge NCs embedded in an SiO_2 matrix. While this may appear to contradict earlier theoretical calculations[44] and experimental XAS results[10] (which showed stronger QC effects in Ge than in Si), we believe it illustrates the pivotal role of the matrix used when fabricating these devices.[45] As suggested by Barbagiovanni *et al.*,[6] the SiN_x matrix acts as a finite potential barrier, allowing for tunneling of carriers; hence, quantum dots in SiN_x can be described quite accurately by a strong confinement model. By contrast, SiO_2 acts as an infinite potential barrier[6] and the confinement strength in this system can be expected to be lower. More importantly, recent DFT calculations have shown that in addition to QC effects in small NCs, the matrix must be taken into account when evaluating the resultant energy levels.[46] With

increasing polarity of the bonds between the NCs and the matrix, there is an increasing dominance of the interface strain over the QC effects. Therefore, we suggest that in the system of NCs embedded in a polar SiO_2 matrix, the QC can be drastically reduced as it competes against interface effects.

A combination of factors is likely to contribute to the observed downward shift in volume plasmon energies for the NCs < 4 nm, from medium to weak confinement. First, it has been reported both experimentally and theoretically that interface states could play an important role in NCs smaller than a critical size ($\sim$3 nm), whereas the larger crystals simply follow the usual QC model.[46–48] Second, there are reports of lattice instability, which could cause a structural transition from a diamond-type structure to an amorphous phase in very small crystallites ($<$3 nm).[49] As mentioned earlier, the particles with sizes $\sim$2 nm observed in layer 3 were found to be amorphous. Bording and Taftø have used molecular-dynamics simulations to predict a critical size of 2 nm for Ge NCs, below which the entire crystal will to some degree be deformed or eventually be assimilated in the amorphous phase.[20] This transition would very likely change the physical properties related to the electronic band structure. Calculation of Ge band structure modifications caused by phase transitions (using plasmon energy shifts as an indicator) could further confirm this hypothesis. Finally, the higher density and smaller distance between the NCs > 4 nm in layer 2 could cause stronger coupling effects than in the more sparsely populated layer 3. This could in turn enhance the optical absorption cross sections and the stronger plasmon coupling between NCs could give rise to the stronger confinement trend in layer 2. This suggestion still remains explorative: further experimental and theoretical studies would be required to reach a more certain conclusion.

E. Comment on the band gap of the SiO_2 matrix

Besides pure NC size effects, the chemistry of the matrix can play an important role in the observed quantum size effects in term of potential barrier height. In order to ascertain the presence of any change in the SiO_2 matrix band gap (compared to pure SiO_2) we compared low-loss EEL spectra from layers 1 and 2 [Fig. 7(a)]. Figure 7(b) shows the corresponding zero-loss peak subtracted plasmon peaks, extracted from the SMART line scan at positions A and B [Fig. 7(a)] and averaged over 20 adjacent data points to improve the signal-to-noise ratio. Spectrum A from layer 1 shows a sharp peak at 24 eV corresponding to the plasmon energy of pure SiO_2, while spectrum B from layer 2 shows an asymmetric plasmon peak which is skewed toward the lower energy side, implying a contribution from both Ge and SiO_2 signals. The deconvolution of spectrum B revealed component peaks at 23 and 17 eV corresponding to the plasmon energies of SiO_2 and Ge NCs, respectively. In addition to the distinct plasmon peaks, the very low-loss energy regions from 4 to 11 eV in spectra A and B exhibit significant differences in features and intensities. The visible band gap signal of the stoichiometric SiO_2 in spectrum A is estimated to be at 9.5 eV (from the intersection of a straight line originating from the background level with a linear fit to the onset of the low-loss signal spectrum), while

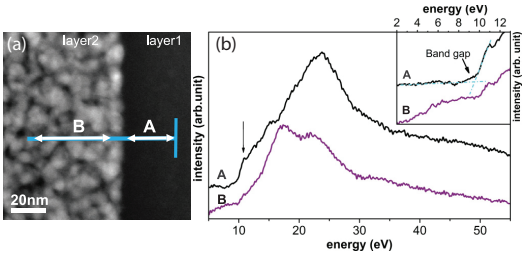

FIG. 7. (Color online) (a) HAADF-STEM image of layers 1 and 2 with different probe positions labeled from which corresponding averaged low-loss EELS SMART line scans were acquired. (b) Plasmon peaks extracted from the SMART line scan at different positions indicated in (a). The inset shows visible band gap signal of the stoichiometric SiO_2 in spectrum A which is estimated to be at 9.5 eV, while it becomes hardly to recognized in spectrum B. The arrow points out position of the exciton peak observed in both spectra A and B.

it is no longer visible in spectrum B. This can be attributed to the overlap with the E_2 interband transition at $\sim$6 eV in front of the band gap onset in spectrum B. Therefore, it is impossible to conclude directly if there is a real change in the SiO_2 band gap energy from layer 1 to layers 2 and 3 or whether this is caused by the contribution of Ge NCs to the low-loss spectra. On the other hand, any change of the characteristic exciton peak around 11 eV[16] just at the band gap signal observed in all of our low-loss EELS spectra might be used as an indirect evidence of a band gap change of SiO_2. The exciton peaks measured in layers 1, 2, and 3 are 11.0, 10.8, and 10.9 $\pm$ 0.3 eV respectively. These values compare well with literature data for crystalline SiO_2, which indicate an exciton peak at 10.8 eV.[50] Thus, if there is a band gap variation of the SiO_2 matrix, it is too small to be detected within our experimental error. This is consistent with the core-loss EELS results, which show that the features and peak energies of the Si $L_{2,3}$ absorption edges of layers 2 and 3 do not change compared to that of the stoichiometric SiO_2 in layer 1.

IV. CONCLUSION

Our studies have shown clear evidence of QC effects on the volume plasmons and interband transitions of individual Ge NCs embedded in an SiO_2 matrix. We have explained some of the discrepancies between earlier theoretical and experimental works on the behavior of the E_2 transition, by demonstrating a blue shift of $\sim$2 eV when the NC size decreases from 6 to 4 nm. The theoretical medium confinement curve reproduces well the overall size dependence of plasmon energies, although it appears to overestimate the QC for NCs smaller than 4 nm, which are better described by a weak confinement model. This double regime, as well as the overall weaker confinement effects (a stronger confinement was expected from initial theoretical considerations) can be interpreted as the result of structure reconstruction and enhanced interface effects in the very small NCs. The influence of the SiO_2 matrix on the optical response of the NCs was also investigated. The nearly stoichiometric SiO_2 matrix is found to provide not only an

infinite potential barrier to confine electrons and holes in the spherical shape Ge NCs but also an increasing polarity of the bonds at the interfaces between the NCs and the matrix compared to the SiN_x matrix. These factors are very important to determine the strength of the observed QC and the enhanced interband transitions.

ACKNOWLEDGMENTS

The authors would like to thank the University of Oslo for financial support. The SuperSTEM Laboratory is funded by the UK Engineering and Physical Sciences Research Council (EPSRC).

*Corresponding author: danpn@fys.uio.no

[1] L. Pavesi and R. Turan, *Silicon Nanocrystals* (Wiley-VCH, Berlin, 2010), p. 1.
[2] G. Conibeer, *Silicon Nanocrystals* (Wiley-VCH, Berlin, 2010), p. 555.
[3] Y. Kayanuma, Phys. Rev. B **38**, 9797 (1988).
[4] C. Bulutay and S. Ossicini, *Silicon Nanocrystals* (Wiley-VCH, Berlin, 2010), p. 5.
[5] A. D. Yoffe, Adv. Phys. **42**, 173 (1993).
[6] E. G. Barbagiovanni, D. J. Lockwood, P. J. Simpson, and L. V. Goncharova, J. Appl. Phys. **111**, 034307 (2012).
[7] R. Erni and N. D. Browning, Ultramicroscopy **107**, 267 (2007).
[8] T. Hanrath and B. A. Korgel, Nano Lett. **4**, 1455 (2004).
[9] P. D. Nguyen, D. M. Kepaptsoglou, Q. M. Ramasse, and A. Olsen, Phys. Rev. B **85**, 085315 (2012).
[10] C. Bostedt, T. v. Buuren, T. M. Willey, N. Franco, L. J. Terminello, C. Heske, and T. Moller, Appl. Phys. Lett. **84**, 4056 (2004).
[11] P. Tognini, L. C. Andreani, M. Geddo, A. Stella, P. Cheyssac, R. Kofman, and A. Migliori, Phys. Rev. B **53**, 6992 (1996).
[12] J. R. Heath, J. J. Shiang, and A. P. Alivisatos, J. Chem. Phys. **101**, 1607 (1994).
[13] D. V. Melnikov and J. R. Chelikowsky, Solid State Commun. **127**, 361 (2003).
[14] S. Schamm, C. Bonafos, H. Coffin, N. Cherkashin, M. Carrada, G. Ben Assayag, A. Claverie, M. Tencé, and C. Colliex, Ultramicroscopy **108**, 346 (2008).
[15] R. F. Egerton, *Electron Energy-Loss Spectroscopy in the Electron Microscope* (Springer, New York, 2011).
[16] R. Erni, N. D. Browning, Z. R. Dai, and J. P. Bradley, Micron **36**, 369 (2005).
[17] O. L. Krivanek, G. J. Corbin, N. Dellby, B. F. Elston, R. J. Keyse, M. F. Murfitt, C. S. Own, Z. S. Szilagyi, and J. W. Woodruff, Ultramicroscopy **108**, 179 (2008).
[18] K. Sader, B. Schaffer, G. Vaughan, R. Brydson, A. Brown, and A. Bleloch, Ultramicroscopy **110**, 998 (2010).
[19] L. L. Araujo, R. Giulian, D. J. Sprouster, C. S. Schnohr, D. J. Llewellyn, P. Kluth, D. J. Cookson, G. J. Foran, and M. C. Ridgway, Phys. Rev. B **78**, 094112 (2008).
[20] J. K. Bording and J. Taftø, Phys. Rev. B **62**, 8098 (2000).
[21] N. Luca Dal, H. Sebastien, Z. Natalia, Y. Jae Hyung, W. Andrew, S. Michael, M. Jurgen, G. Giulia, and C. K. Lionel, IEEE J. Sel. Top. Quantum Electron. **12**, 1151 (2006).
[22] S. Cosentino, S. Mirabella, M. Miritello, G. Nicotra, R. Lo Savio, F. Simone, C. Spinella, and A. Terrasi, Nanoscale Res. Lett. **6**, 135 (2011).
[23] P. D. Nguyen, D. M. Kepaptsoglou, Q. M. Ramasse, M. F. Sunding, L. O. Vestland, T. G. Finstad, and A. Olsen, J. Appl. Phys. **112**, 073514 (2012).
[24] A. Bianconi and R. S. Bauer, Surf. Sci. **99**, 76 (1980).
[25] G. R. Harp, Z.-L. Han, and B. P. Tonner, Phys. Scr. **1990**, 23 (1990).
[26] G. E. v. Dorssen, M. D. Roper, H. A. Padmore, A. D. Smith, and G. N. Greaves, Rev. Sci. Instrum. **66**, 1480 (1995).
[27] R. Pantel, M. C. Cheynet, and F. D. Tichelaar, Micron **37**, 657 (2006).
[28] E. D. Palik, *Handbook of Optical Constants of Solids* (Academic Press, MA, USA, 1991).
[29] J. P. R. Bolton and M. Chen, J. Phys.: Condens. Matter **7**, 3373 (1995).
[30] J. P. R. Bolton and M. Chen, Ultramicroscopy **60**, 247 (1995).
[31] R. Erni and N. D. Browning, Ultramicroscopy **108**, 84 (2008).
[32] R. Erni, S. Lazar, and N. D. Browning, Ultramicroscopy **108**, 270 (2008).
[33] C. W. Teng, J. F. Muth, R. M. Kolbas, K. M. Hassan, A. K. Sharma, A. Kvit, and J. Narayan, Appl. Phys. Lett. **76**, 43 (2000).
[34] S. Hayashi, M. Fujii, and K. Yamamoto, Jpn. J. Appl. Phys. **28**, L1464 (1989).
[35] E. J. Friebele, D. L. Griscom, M. Stapelbroek, and R. A. Weeks, Phys. Rev. Lett. **42**, 1346 (1979).
[36] D. L. Griscom and E. J. Friebele, Phys. Rev. B **34**, 7524 (1986).
[37] A. Kameyama, A. Yokotani, and K. Kurosawa, J. Appl. Phys. **95**, 4000 (2004).
[38] R. Guerra, M. Marsili, O. Pulci, and S. Ossicini, Phys. Rev. B **84**, 075342 (2011).
[39] C. E. Bottani, C. Mantini, P. Milani, M. Manfredini, A. Stella, P. Tognini, P. Cheyssac, and R. Kofman, Appl. Phys. Lett. **69**, 2409 (1996).
[40] H. C. Weissker, J. Furthmüller, and F. Bechstedt, Phys. Rev. B **65**, 155328 (2002).
[41] C. Bulutay, Phys. Rev. B **76**, 205321 (2007).
[42] M. Mitome, Y. Yamazaki, H. Takagi, and T. Nakagiri, J. Appl. Phys. **72**, 812 (1992).
[43] S. Takeoka, M. Fujii, S. Hayashi, and K. Yamamoto, Phys. Rev. B **58**, 7921 (1998).
[44] Y. M. Niquet, G. Allan, C. Delerue, and M. Lannoo, Appl. Phys. Lett. **77**, 1182 (2000).
[45] J. E. Chang *et al.*, J. Phys. D: Appl. Phys. **45**, 105303 (2012).
[46] D. König, J. Rudd, M. A. Green, and G. Conibeer, Phys. Rev. B **78**, 035339 (2008).
[47] M. V. Wolkin, J. Jorne, P. M. Fauchet, G. Allan, and C. Delerue, Phys. Rev. Lett. **82**, 197 (1999).
[48] Z. Zhou, L. Brus, and R. Friesner, Nano Lett. **3**, 163 (2003).
[49] Y. Maeda, Phys. Rev. B **51**, 1658 (1995).
[50] L. A. J. Garvie, P. Rez, J. R. Alvarez, P. R. Buseck, A. J. Craven, and R. Brydson, Am. Mineral. **85**, 732 (2000).

Paper IV

P. D. Nguyen, A. E. Gunnæs, M. F. Sunding, and A. Olsen

Heterogen nucleation and growth of $CrSi_2$ in sputtered thin films of silicon and silicon nitride

Submitted to Journal of Materials Research (November 2012)